

**COMPUTATIONAL ANALYSIS OF PULSED-
LASER PLASMON-ENHANCED
PHOTOTHERMAL ENERGY CONVERSION
AND NANOBUDDLE GENERATION IN THE
NANOSCALE**

by

Ioannis Karampelas

July 28, 2016

A dissertation submitted to the Faculty of the Graduate School of
the University at Buffalo, State University of New York in partial
fulfillment for the degree of Doctor of Philosophy

Department of Chemical and Biological Engineering

Acknowledgements

First and foremost, I would like to begin by expressing my honest gratitude and appreciation to my academic advisor: Prof. Edward P. Furlani. His guidance, leadership and patience were paramount to the completion of the current work. Under his supervision, an initial idea was able to grow and mature, taking the form that it has today. Prof. Furlani offered me the great opportunity to work in his group not only on the project that became my dissertation but also on plethora of other exciting projects that added to my experience and qualified me for future endeavors. His assistance, suggestions and constructive critique proved invaluable throughout the pursuit of my doctoral degree and contributed to the successful completion of this work. Indeed, it has been an honor to be his student and serve under the wing of such a multi-talented scientist and engineer who was also my friend and mentor.

I would also like to extend my sincere thanks to my committee members Profs. Mark T. Swihart and Gang Wu for their assistance and valuable suggestions in improving this work. Along with the entire faculty of the Department of Chemical Engineering at University at Buffalo, they guided me in lifetime decisions towards the completion of my degree.

I can't express anything else other than profound appreciation to present and past group members and lifetime friends: Xiaozheng Xue, Kai Liu, Jenifer Gómez Pastora, Viktor

Sukhotskiy, Fatema Alali, Vikram Reddy Ardham, Young Hwa Kim, Shailesh Konda, Koushik Ponnuru, Chenxu Liu, Moon Kattula, Jianchao Wang, Aditi Verma and Gourav Garg for their active participation, lively discussions, encouragement and valuable feedback in the course of my research.

Last but certainly not least, my deepest gratitude to my beloved parents, Haralabos and Maria, my loving sisters Natalia and Demi for their everlasting love and motivation. Without their help, none of my achievements would have been possible.

Table of Contents

Acknowledgements	ii
Table of Contents	iv
List of Tables	vi
List of Figures and Graphs	vi
Abstract	ix
Chapter 1: Introduction	1
1.1 The Basics of Plasmonic Heating	2
1.1.1 Nanoparticle Illumination	2
1.1.2 Photothermal Energy Conversion	6
1.2 Biological Applications of Plasmonic Nanotransducers	10
1.2.1 Photothermal Therapy	10
1.2.2 Nanobubble Treatment	16
Chapter 2: Theory and Methods	22
2.1 Photonic Analysis	24
2.1.1 Spherical Nanoparticles	24
2.1.2 Numerical Field Analysis	25
2.2 Fluidic Analysis	28
2.2.1 Temperature and Flow Fields	28
2.2.2 Phase Change and Bubble Dynamics	30
Chapter 3: Combined Computational Modeling	34
3.1 Nanospheres	35
3.1.1 Synthesis	35
3.1.2 Photonic Simulations	37
3.1.3 Thermofluidic Simulations	40
3.2 Nanorods	44
3.2.1 Synthesis	44
3.2.2 Photonic Simulations	47
3.2.3 Thermofluidic Simulations	49

3.3	Nanorings and nanotori	52
3.3.1	Synthesis.....	52
3.3.2	Photonic Simulations.....	54
3.3.3	Thermofluidic Simulations	56
3.4	Nanocages and Nanoframes	60
3.4.1	Synthesis.....	60
3.4.2	Photonic Simulations.....	63
3.4.3	Thermofluidic Simulations	67
3.5	Summary of Combined Modeling Effort	73
Chapter 4: Colloidal Photothermal Modeling		75
4.1	Photonic Models for Nanoparticles at Varying Orientations	76
4.1.1	Absorption Spectra of Gold Nanorods and Nanotori at Discrete Rotations ..	76
4.1.2	Absorption Comparison of Gold Nanorods, Nanotori and Nanorings.....	79
4.1.3	Absorption Cross-Section of Nanoframes under Different Orientations	82
4.2	Colloidal Heating of Identical Nanoparticles	84
4.2.1	Gold Nanorods.....	84
4.2.2	Gold Nanotori	85
4.3	Cooperative Nanobubble Nucleation	87
4.3.1	System of Two Nanotori.....	87
4.4	Summary of Colloidal Modeling Effort	90
Chapter 5: Future Work Recommendations and Conclusions		91
5.1	Future Work Recommendations	92
5.1.1	Two-Temperature Model for Femto- and Pico-Second Pulsing.....	92
5.1.2	Temperature Dependent Material Properties.....	93
5.1.3	Illumination during Nanobubble Formation	95
5.2	Conclusions	97
References		100

List of Tables

Table 3.1. Summary of modeled nanoparticle geometries with heating and nanobubble parameters.

List of Figures and Graphs

Figure 1.1. Light wave passing through a plasmonic material. The induced electric field creates a charge separation in the atoms and thus an oscillating electron cloud (source: www.nanocomposix.com).

Figure 1.2. Photothermal energy conversion a) Numerical calculation of heat power as a function of incident wavelength for the case of a single nanorod (50 x 12 nm), b) Heat power density within the nanoparticle for various wavelengths (Baffou and Quidant 2013).

Figure 1.3. Illustration of the process of photothermal therapy. a) Preparation of nanoparticles b) Intravenous injection c) Laser illumination d) Successful treatment

Figure 1.4. In-situ photothermolysis of living EMT-6 tumor cells by thermal explosions triggered by laser-illuminated gold nanorods. Laser Irradiance (a-d) 113 mJ/cm², (e-h) 93mJ/cm² (C.L. Chen et al. 2010a).

Figure 3.1. Scanning electron microscopy (SEM) image illustrating gold nanospheres with an average diameter of 60 nm (source: www.nanocomposix.com).

Figure 3.2. Photonic analysis of a gold nanosphere (a) Computational domain and field analysis, (b) Absorbed power vs. wavelength.

Figure 3.3. Photothermal heat cycle of a nanosphere (R = 30 nm) (cross-sectional view): plot of nanosphere temperature vs. time, pulse duration indicated by red arrow and dashed line and inset plots showing various phases of the thermal cycle; (a) initial heating, (b) primary nanobubble formation, (c) primary nanobubble collapse, (d) secondary nanobubble formation, (e) secondary nanobubble collapse with cooling.

Figure 3.4. Scanning electron microscopy (SEM) image illustrating gold nanorods with an average length and diameter of 60 and 17 nm, respectively (source: www.nanocomposix.com).

Figure 3.5. Photonic analysis of a gold nanorod (a) Computational domain and field analysis, (b) Absorbed power vs. wavelength.

Figure 3.6. Photothermal heat cycle of a nanorod (L = 60 nm, R = 8.5 nm) (cross-sectional view): plot of nanorod temperature vs. time, pulse duration indicated by red arrow and

dashed line and inset plots showing various phases of the thermal cycle; (a) initial heating, (b) nanobubble formation, (c) nanobubble (maximum size), (d) nanobubble collapse, (e) cooling.

Figure 3.7. Nanostructure geometries: (a) nanoring, (b) nanotorus.

Figure 3.8. SEM image (tilted by 80°) of gold nanotori fabricated with colloidal lithography (Aizpurua et al. 2003)

Figure 3.9. Photonic analysis of a gold nanotorus ($R= 30$ nm and $r= 10$ nm) with parallel alignment to the incident polarization: (a) Computational domain and plot of E_x through a cross section of the domain, (b) Absorbed power vs. wavelength at parallel orientation.

Figure 3.10. Absorption spectra for a nanoring ($R = 40$ nm, $r = 20$ nm, $h = 20$ nm) and a nanotorus ($R = 30$ nm, $r = 10$ nm), both aligned parallel to the incident field.

Figure 3.11. Photothermal heat cycle of a gold nanotorus ($R= 30$ nm and $r = 10$ nm) (cross-sectional view): plot of nanorod temperature vs. time, pulse duration indicated by red arrow and dashed line and inset plots showing various phases of the thermal cycle; (a) initial heating, (b) nanobubble formation, (c) nanobubble (maximum size), (d) nanobubble collapse, (e) cooling.

Figure 3.12. Nanoframe structure and characteristic dimensions (Edge length L and edge thickness W).

Figure 3.13. Transmission electron microscopy (TEM) image of gold nanoframes with an average edge length $L = 50$ nm and thickness $W = 10$ nm (Au et al. 2008)

Figure 3.14. Photonic analysis of a gold nanoframe ($L=28$ nm and $R=4$) with parallel alignment to the incident polarization: (a) computational domain, (b) in plane spatial plot of electric field intensity enhancement ($|\mathbf{E}|^2/|\mathbf{E}_0|^2$) (plane shown in inset).

Figure 3.15. Nanoframe absorption spectra as a function of geometric parameters: (a) absorption spectra vs. L ($W = 7$ nm) (b) absorption spectra vs. $R= L/W$ ($L = 28$ nm).

Figure 3.16. Photothermal heat cycle of a nanoframe ($L = 50$ nm, $W = 5$ nm) (cutaway perspective of heated nanocage): plot of nanoframe temperature vs. time, pulse duration indicated by red arrow and dashed line and inset plots showing various phases of the thermal cycle; (a) nanobubble formation, (b) nanobubble (maximum size), (c) nanobubble collapse, (d) cooling.

Figure 3.17. Photothermal heat cycle of a nanoframe ($L = 50$ nm, $W = 10$ nm) (cutaway perspective of heated nanocage): plot of nanoframe temperature vs. time, pulse duration indicated by red arrow and dashed line and inset plots showing various phases of the

thermal cycle; (a) nanobubble formation, (b) nanobubble (maximum size), (c) nanobubble collapse, (d) cooling.

Figure 3.18. Photothermal heat cycle of a nanoframe ($L = 70$ nm, $W = 5$ nm) (cutaway perspective of heated nanocage): plot of nanoframe temperature vs. time, pulse duration indicated by red arrow and dashed line and inset plots showing various phases of the thermal cycle; (a) nanobubble formation, (b) nanobubble (maximum size), (c) nanobubble collapse, (d) cooling.

Figure 3.19. 3D perspective of CFD simulations showing nanobubble at maximum expansion for different nanoframe geometries.

Figure 4.1. Pulsed laser heating of colloidal gold nanorods and nanotori. The nanoparticle orientation is defined by angles θ and φ . The inset plot illustrates a laser pulse profile, irradiance I vs. t .

Figure 4.2. Normalized absorption spectra with nanoparticles at different orientations: (a) nanorod ($L = 60$ nm, $R = 8.5$ nm) and (b) nanotorus ($R = 40$ nm, $r = 10$ nm).

Figure 4.3. Normalized peak absorption at respective fixed LSPR wavelengths as a function of particle orientation (θ, φ): (a) nanorod at $\lambda = 770$ nm ($L = 60$ nm, $R = 8.5$ nm), (b) nanotorus at $\lambda = 986$ nm ($R = 40$ nm, $r = 10$ nm).

Figure 4.4. Normalized peak absorption at respective fixed LSPR wavelengths as a function of particle orientation (θ, φ): (a) nanoring at $\lambda = 793$ nm ($R = 40$ nm, $r = 20$ nm), (b) nanotorus at $\lambda = 825$ nm ($R = 30$ nm, $r = 10$ nm).

Figure 4.5. Pulsed laser heating of colloidal Au nanoparticles. (a) Nanoparticle orientation is defined by angles θ and φ . Inset plot illustrates a laser pulse profile, irradiance I_{laser} vs. t . (b) Optical absorption cross section σ_{abs} vs. orientation.

Figure 4.6. Cooperative heating effects (a) Percentage of single nanorod energy required to achieve multi-rod nucleation vs. nanorod separation, (b) Percentage of single nanotorus energy required to achieve 2 tori nucleation vs. nanotorus separation.

Figure 4.7. Photothermal heat cycle of a 2 identical nanotori system ($R = 30$ nm and $r = 10$ nm) (cross-sectional view): plot of nanorod temperature vs. time, pulse duration indicated by red arrow and dashed line and inset plots showing various phases of the thermal cycle; (a) initial heating, (b) nanobubble formation, (c) nanobubble (maximum size), (d) nanobubble collapse, (e) cooling.

Figure 5.1. Temperature dependent thermal conductivity for water.

Figure 5.2. Normalized absorption spectra for varying nanobubble size (40 to 80 nm).

Abstract

The ability to generate and control thermal energy with nanoscale resolution is finding increasing use in a variety of applications spanning the fields of nanoparticle synthesis, nanofabrication, bio-imaging and medical therapy. One of the most promising approaches to achieving this involves the use of plasmonics, wherein a laser is used to heat metallic nanostructures at their localized surface plasmon resonance (LSPR) wavelength. At plasmon resonance there is a collective and coherent oscillation of electrons within the nanostructures that gives rise to peak absorption of the incident photons and highly localized (sub-wavelength) heating and field enhancement. Laser-based plasmon-enhanced photothermal energy conversion in the nanoscale has drawn increased interest in recent years for applications such as photothermal therapy and nanoscale imaging since it can provide efficient heating with unprecedented (subwavelength) spatial resolution. In the current work, we study pulsed-laser plasmon-assisted nanoscale bubble nucleation around various nanoparticle geometries using combined computational electromagnetic and CFD-based fluidic analysis. This combined modeling approach will aid in the development of a rational guide to experimentalists in this field since it enables fundamental understanding and, hence, rational design of plasmon-based photothermal processes; eventually leading to the development of novel photothermal applications. Our primary goal is to develop computational electromagnetic and CFD-based models for some of the most commonly used nanoparticle geometries. Such modeled geometries include nanospheres, nanorods, nanoframes, nanotori and nanorings. Two types of computational models will be developed: a) Computational Electromagnetics models for

the photonic analysis, used to calculate photothermal energy conversion within the nanoparticles, i.e. the time-averaged power absorbed by a particle as a function of the wavelength, intensity and polarization of the incident light and b) Computational Fluid Dynamic (CFD)-based models that predict thermal, pressure and flow effects including the temperature rise in the particle, heat transfer from the particle to the fluid, phase change within the fluid leading to homogeneous bubble nucleation, the dynamic behavior of the bubble as it expands and collapses, and the temperature, pressure and flow throughout the fluid during the entire process. In order to achieve that goal, we use state-of-the-art software packages including but not limited to: FLOW 3D versions 10.1 and 11.1 from Flow Science Corp. (www.flow3d.com) and COMSOL Multiphysics Software versions 4.4 and 5.2 with full CFD-FSI, nanofluidics and RF analysis capability, respectively. The initial modeling effort is mainly focused on modeling nanoparticles exhibiting some kind of axial symmetry, such as nanospheres and nanorods, with constant fluid and particle properties. It will be used to determine heretofore unknown properties such as the plasmon resonance wavelength, the amount of power required to generate and sustain nanobubbles without melting the nanoparticles and the size and duration of occurring nanobubbles for each nanoparticle geometry. In the next phase of the study, we proceed with the development of enhanced computational models to account for colloidal effects. Although initial models are able to predict the details of the generation of a nanobubble around a single nanoparticle illuminated in parallel orientation relative to the polarization of the incident field, most in-vivo applications involve a colloidal solution of particles: a collection of particles at random orientations. Therefore, a series of models to account for colloidal effects for certain nanoparticle geometries will be

developed. Such models include a) cooperative colloidal nanoparticle heating models that predict the average temperature rise of a colloidal solution of identical nanoparticles under fixed illumination as a function of nanoparticle concentration, b) cooperative nanobubble nucleation models that are able to calculate the effects of cooperative nucleation including the generation of nanobubbles around multiple identical nanoparticles and merging of nanobubbles and c) photonic models for colloidal nanoparticles at varying orientations that can determine the fall off in the peak absorption under fixed illumination as the nanoparticles take on different orientations. This study directly addresses the knowledge gap concerning the colloidal behavior of plasmonic nanoparticles. Finally, we will be suggesting new potential paths of research such as a non-continuum, high accuracy approach. Although, the models developed in this study represent the most accurate nanobubble modeling attempt thus far, the assumptions of continuum theory and of constant nanoparticle properties might lead to potential discrepancies between modeling and experimental results. Hence, in the interest of increased accuracy, we will suggest the use of the Two-temperature Model (TTM) to describe non-equilibrium femto-second electron relaxation in the nanoparticles. Such models may enable the proposed theory to be extended to femto- and pico-second pulsing. A further refinement of the models developed initially can be potentially realized with the inclusion of temperature dependent properties for the fluid and the nanoparticle. The combination of non-equilibrium effects and temperature pertinent properties will provide most sophistication to an already complex modeling effort. In addition to the enhanced models, initial computational models could also be extended to include the fall off on the peak absorption when a nanobubble is being formed around a nanoparticle while it is still being illuminated. Overall, the

modeling approach described herein will a) directly address the knowledge gap of photothermal therapy nanobubble specifics for each geometry such as required wavelength for plasmon resonance, required energy and pulse duration to achieve nucleation without melting or even evaporating the nanoparticles, b) explain the temperature related behavior of colloidal plasmonic nanoparticles for photothermal drug delivery and c) provide experimentalists in the field with a most accurate rational guide for the development of novel photothermal applications.

Chapter 1: Introduction

1.0 Over the last several years there has been a proliferation of research into the synthesis, characterization and photonic applications of metallic (e.g. Au, Ag) nanoparticles (Frens 1973; Goodman et al. 1980; P. K. Jain et al. 2008; Kreibig and Vollmer 1995; Lewinski et al. 2008; Schultz et al. 2000). This is due, in large part, to the unique optical properties of such particles, especially manifestations of localized surface plasmon resonance (LSPR). At plasmon resonance, there is a collective and coherent oscillation of free electrons in subwavelength particles that results in an intense absorption and scattering of incident light, as well as highly localized field enhancement. Metallic nanoparticles exhibit this resonance at shape and size-dependent wavelengths that span the ultraviolet (UV) to near-infrared (NIR) spectrum. A desired resonant wavelength can in principle be obtained by controlling the geometry and dimensions of the particles during synthesis. The ability to tune LSPR in this fashion has proven useful for a broad range of applications such as biosensing (Carrara 2010), optical coherence tomography (Oldenburg et al. 2006), photoacoustic imaging (Agarwal et al. 2007), two-photon luminescence imaging (H. Wang et al. 2005), photothermal therapy (X. Huang et al. 2006), photovoltaic and nanoparticle synthesis (Hashimoto et al. 2012). In many applications, a femto- or nano-second pulsed laser is used to excite a desired LSPR response of a nanoparticle (Ekici et al. 2008). The ability to probe and exploit plasmon-enhanced light-matter interactions occurring in ultra-fast time frames and nanoscale spatial resolution has spawned fundamental and translational research with broad impact in fields that include analytical and material chemistry, condensed matter physics, nanophotonics and biomedicine.

1.1 The Basics of Plasmonic Heating

1.1.1 Nanoparticle Illumination

1.1.1.1 As a first step in our investigation of the use of plasmonic nanoparticles as nano-sources of heat and subsequent nanobubble nucleation, we discuss the basic mechanisms that lead to the generation of heat in metal nanoparticles from the absorption of incident light.

1.1.1.2 Most metal nanoparticles support electronic resonances known as localized surface plasmons (LSPs) that can be excited when such nano-objects are illuminated at a certain wavelength. For the purposes of the current research, plasmons can be understood in a classical sense as an oscillation of a free electron density with respect to the fixed positive ions in a metal, notably noble metals (e.g. Au or Ag) at optical frequencies as seen in **Fig. 1.1**. Under certain circumstances, plasmons can be excited by an incident electromagnetic (EM) field, i.e. when there is a proper momentum match

between the incoming photons and the plasmons. Once plasmons are excited, they give rise to greatly enhanced and highly localized fields and absorption of energy, which are useful for many applications requiring

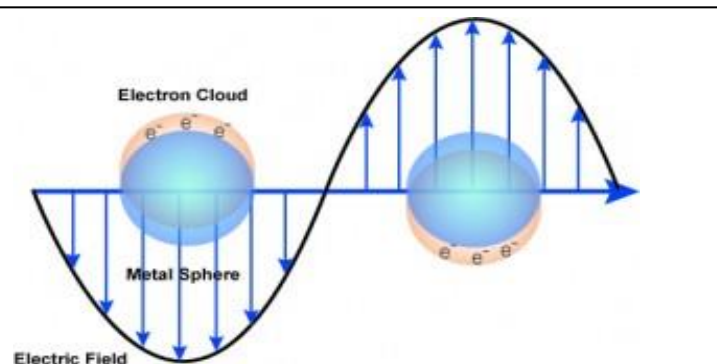


Figure 1.1. Light wave passing through a plasmonic material. The induced electric field creates a charge separation in the atoms and thus an oscillating electron cloud (source: www.nanocomposix.com).

nanoscale heat generation or manipulation, e.g. photothermal therapy. The response of a plasmonic material to an applied field can be predicted using classical electrodynamics if the material can be modeled using an effective bulk dispersive dielectric function. In practice, for noble metal particles, a bulk dielectric function can be used to describe plasmonic behavior for dimensions down to approximately in 10 nm, and a size dependent dielectric function can be employed for objects with dimensions down to roughly 1-2 nm (Coronado and Schatz 2003; Imura et al. 2005; Kottmann et al. 2001).

1.1.1.3 The wavelength at which local surface plasmon resonance occurs depends mostly on the morphology and the type of the metal that nanoparticles are fabricated with. This ability to tune the frequency at which LSP resonances arise, for gold and silver nanoparticles, from the visible to the near infrared (NIR) is a very important quality for bioapplications (Frangioni 2003). Since recent advances in the field of bottom-up fabrication techniques have allowed colloid metal nanoparticles in a variety of different shapes and sizes to be created at low cost, nanoparticles specifically tailored for a plethora of different plasmonic applications are currently available.

1.1.1.4 In order to provide a basic understanding of the physics involved in nanoparticle illumination, we assume that a metal nanoparticle immersed in fluid is being irradiated by polarized monochromatic light at an angular frequency ω . The nanoparticle has a complex relative permittivity $\epsilon(\omega)$ while the surrounding fluid has a real relative permittivity ϵ_s . For the simplest case, a metal sphere with radius R illuminated at a wavelength much larger than the particle itself can be considered as an electromagnetic

dipole. The wavelength at which LSP resonance occurs can then be derived from its polarizability $\alpha(\omega)$ which reads:

$$\alpha(\omega) = 4\pi R^3 \frac{\varepsilon(\omega) - \varepsilon_s}{\varepsilon(\omega) + 2\varepsilon_s} \quad (1.1)$$

Based on this expression, it can be concluded that for the simple case of a sphere, LSP resonance arises when the polarizability gets maximized. This occurs at a frequency ω at which the value of the permittivity of the nanoparticle is $\varepsilon(\omega) \approx -2\varepsilon_s$. For example, for a gold sphere with a radius of approximately 30 nm, submerged in water, the plasmon resonance wavelength is found to be $\lambda \approx 530$ nm. It is useful to note that for larger nanoparticles the previously described dipolar approximation is not valid and more complex models that account for retardation effects are required (e.g. Mie theory) (Bohren and Huffman 2008; Myroshnychenko et al. 2008). Nano-objects of complex geometry, require a full numerical analysis.

1.1.1.5 Nonetheless, for all nanoparticle morphologies the efficiency of the absorption process and thus the effectiveness of the photothermal transduction can be quantified through the absorption and scattering cross-sections (Bohren and Huffman 2008; Myroshnychenko et al. 2008). Independent of nanoparticle geometry, the absorption (σ_{abs}) and scattering (σ_{scat}) cross sections read as follows:

$$\sigma_{abs} = k \operatorname{Im}(\alpha) - \frac{k^4}{6\pi} |\alpha|^2 \quad (1.2)$$

$$\sigma_{scat} = \frac{k^4}{6\pi} |\alpha|^2 \quad (1.3)$$

where k is the angular wavenumber ($2\pi/\lambda$). The photothermal efficiency (μ) can then be determined through the ratio of cross-sections:

$$\mu = \frac{\sigma_{abs}}{\sigma_{scat}} \quad (1.4)$$

The value of μ strongly depends on the morphology of the nanoparticle (H. Chen et al. 2010b; B. Khlebtsov et al. 2006). For the simple case of spherical nanoparticles immersed in water, particles with radii less than 88 nm are found to be more absorption dominant ($\mu \approx 1$) while particles with larger radii were determined to be more scattering dominant ($\mu < 1$). However, this statement is only accurate when comparing the respective maxima of both the absorption and scattering cross-section spectra (Baffou and Quidant 2013).

1.1.1.6 Overall, although gold nanoparticles are generally better absorbers than scatterers of incident light, their actual behavior depends on the illumination frequency. Such frequency has to be precisely determined in order to better understand which the dominant energy conversion pathway actually is. It is worth mentioning that estimating the absorption efficiency of a given plasmonic nanostructure based on experimentally derived extinction spectra, a process commonly employed in literature (Arbouet et al. 2004), does not represent a reliable method of determining the dominant energy conversion pathway. In the current work, we opted for the development of computational models and more specifically full-wave electromagnetic analysis in order to most accurately calculate the absorption cross-section and, hence, the consequent conversion of electromagnetic radiation to heat inside the nanoparticle.

1.1.2 Photothermal Energy Conversion

1.1.2.1 The plasmonic response of metallic nanoparticles to illumination and the resulting thermal effects in a fluid are of particular interest, especially for bioapplications. These effects depend on many factors including the duration of the laser pulse, the wavelength, polarization and intensity of the incident light, the size and shape of the nanoparticles (Hao and Schatz 2004; Hao et al. 2004; Sonnichsen et al. 2002) and the physical properties of the fluid. In order to better understand these effects and the factors affecting them, in this section we describe the basic physics of the process of photothermal energy conversion.

1.1.2.2 The power absorbed by a metallic nanostructure (Q), and subsequently delivered to the surrounding fluid, can be simply expressed using the absorption cross-section σ_{abs} (introduced in paragraph 1.1.1.5) and the irradiance I of the incoming light (power per unit surface). It reads as follows:

$$Q = \sigma_{abs} I \quad (1.5)$$

For the case of a simple sphere of radius r , the heat generation can also be determined through the volume integral of the heat power density $q(r)$ in the nanoparticle which is:

$$Q = \int_V q(r) d^3r \quad (1.6)$$

However, because of the fact that heat generation stems from Joule effects, the heat power density $q(r)$ can also be written as:

$$q(r) = \frac{1}{2} \text{Re} [J(r) \cdot E(r)] \quad (1.7)$$

where $\mathbf{J}(r)$ is the complex amplitude of the electronic current density and $\mathbf{E}(r)$ is the electric field inside the nanostructure. As seen from this analysis, the absorption of energy and the subsequent heat generation is a completely optical problem and directly related to the electric field within the confines of the nanoparticle (Baffou and Quidant 2013).

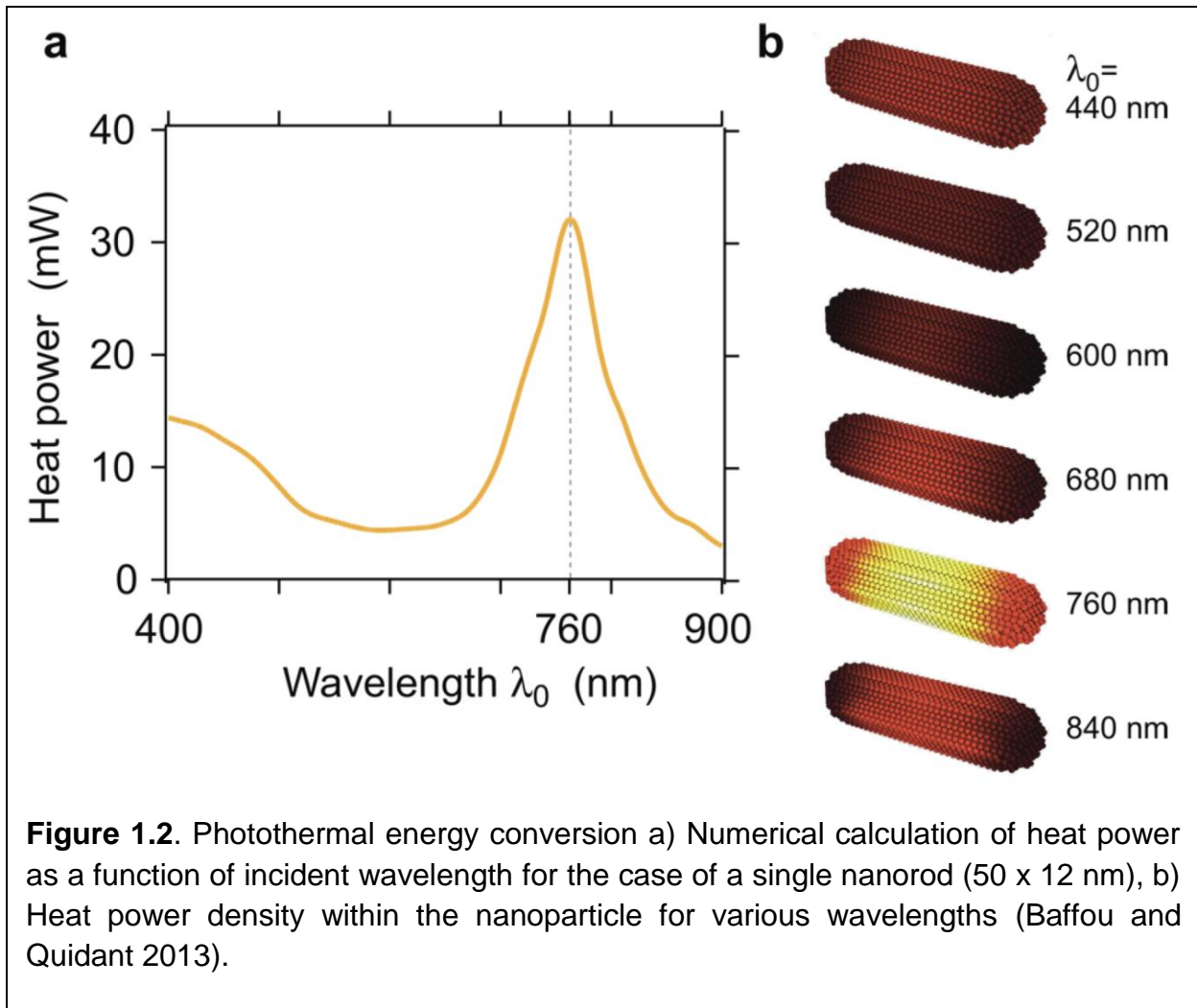
1.1.2.3 Nevertheless, the calculation of the temperature distribution both inside and outside the nanoparticle falls in the field of transport phenomena. For the simplest case of a spherical nanoparticle, the steady state temperature distribution $T(r)$ under continuous illumination can be readily calculated from:

$$\nabla[\kappa(r)\nabla T(r)] = -q(r) \quad \text{Nanoparticle} \quad (1.8)$$

$$\nabla[\kappa(r)\nabla T(r)] = 0 \quad \text{Fluid} \quad (1.9)$$

where $\kappa(r)$ is the radially dependent thermal conductivity. Although, the heat power density $q(r)$ can be non-uniform as it can be seen in **Fig. 1.2**, the temperature of the nanoparticle is generally found to be highly uniform because of the high thermal conductivity of most metals as opposed to their surrounding environment (fluids).

1.1.2.4 Thus far, we described the absorption of light energy under continuous wave illumination. Yet, most applications of metal nanoparticles involve some kind of pulsed illumination ranging from the femtosecond to the nanosecond range. Photothermal energy conversion in pulsed illuminated metallic nanostructures in fluid occurs through a succession of 3 processes (Ekici et al. 2008) involving different time scales. At the onset of illumination, free electrons in the nanoparticles absorb energy from the incident



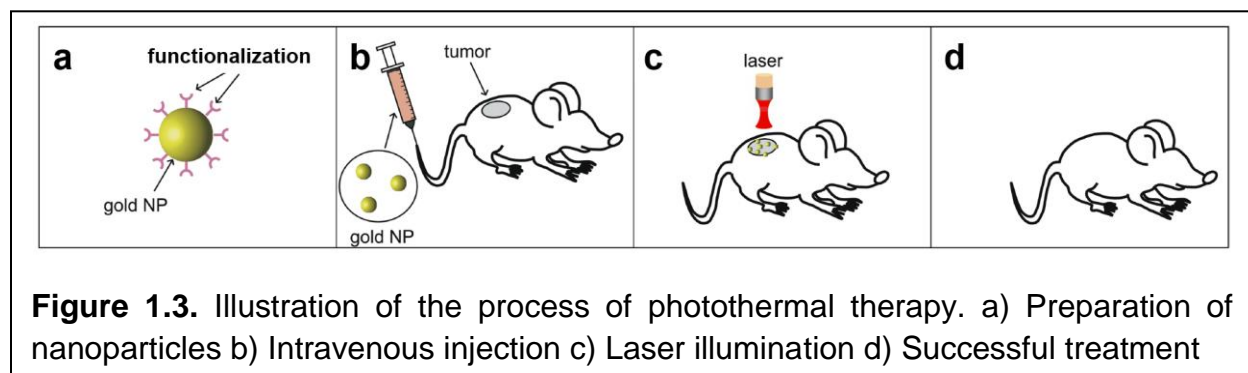
photons. The electrons undergo electron-electron scattering and relax to an equilibrium energy distribution within 10-50 fs. Consequently, these energetic electrons transfer their kinetic energy to the lattice of the nanoparticle through electron-phonon interactions. Thermal equilibrium between the electrons and the lattice occurs on the order of 10 to 50 ps. Finally, as the particle (lattice) temperature increases, energy is transferred to the surrounding fluid through phonon-phonon coupling. Initially, there is a discontinuous jump in temperature at the particle-fluid interface due to the mismatch in material properties, but this subsides within a fraction of a nanosecond (100-400 ps) (Ekici et al. 2008).

1.1.2.5 Pulsed illumination presents researchers with a wealth of advantages such as highly localized temperature increases (Baffou and Rigneault 2011), smaller temperature and pressure variations (Hu and Hartland 2002; V. K. Pustovalov 2005; Volkov et al. 2007) and nanobubble generation which is the focus of the present work (Alali et al. 2013; Furlani et al. 2012; Karampelas et al. 2016; Kotaidis et al. 2006; D. Lapotko 2009a; E. Lukianova-Hleb et al. 2010; Vogel et al. 2008). In the next section we will focus more on the different bioapplications of noble metal nanoparticles as highly isolated sources of heat.

1.2 Biological Applications of Plasmonic Nanotransducers

1.2.1 Photothermal Therapy

1.2.1.1 One of the most prominent applications of plasmonic nanoparticles is photothermal therapy. The basic method of operation of photothermal therapy lies in artificially enhancing the optical absorption of the cancerous tissue compared to healthy tissue. During the last several years, various transducers have been studied for photothermal therapy including organic dyes (e.g. indocyanine green (Zheng et al. 2012)), metal nanoparticles (e.g. Au nanostructures (N. Khlebtsov et al. 2013)) and carbon-based nanomaterials (e.g. carbon nanotubes (Moon et al. 2009)). Among these, there has been an emphasis on applications of gold nanoparticles. Gold nanoparticles are particularly well-suited for bioapplications because they can be synthesized in various sizes and shapes and can be readily coated with a variety of enabling agents using thiolate monolayer chemistry. Such agents include poly(ethylene glycol) (PEG), which enhances biocompatibility and circulation time, cancer specific antibodies (e.g. HER2-antibody (Skrabalak et al. 2007)) to enable selective cancer cell targeting, smart polymers such as poly(N-isopropylacrylamide) (pNIPAAm) (Yavuz et al. 2009) for photothermally controlled drug delivery or combinations thereof. For photothermal applications, gold



nanoparticles can enhance optical absorption of tumor sites through an increase of their concentration in such tissues either via active targeting, as a result of appropriate functionalization, or via agglomeration, due to the nature of the tumorous vascular system. Laser illumination of appropriate wavelength can then locally slowly raise the temperature (usually less than 10 K) of the tissue. This temperature rise (hyperthermia) leads to the disruption of homeostasis of cancer cells causing apoptosis or necrosis. The process in its entirety results in successful patient treatment and is summarized in **Fig. 1.3**. As it can be seen from the following literature review, this method of treatment remains highly popular amongst experimentalists thanks to its relative simplicity and its lack of harmful systemic side-effects usually associated with other methods of cancer therapy, e.g. chemotherapy. However, it has certain disadvantages, namely the lack of high treatment localization which causes the accidental death of healthy cells surrounding the treated tissue (Au et al. 2008; Cherukuri et al. 2010; Gu et al. 2007; X. Huang et al. 2008; Prashant K Jain et al. 2007; Lal et al. 2008; von Maltzahn et al. 2009; Y. Wang et al. 2013; Yakunin et al. 2015).

1.2.1.2 As mentioned previously, in order to achieve the objective of local hyperthermia, appropriate illumination should be employed. It has been demonstrated that maximum penetration of light in human tissues occurs at wavelengths in the near-infrared (NIR) range of the electromagnetic (EM) spectrum. Thus, the collection of wavelengths between 700 and 1000 nm, are commonly referred to as “transparency window”, “therapeutic window” or “optical window”. This high photon propagation is due to the absorption characteristics of particular tissues or organs. In living tissue, the only

major NIR absorbers are water, oxyhemoglobin, deoxyhemoglobin and lipids. On average, for tissues containing 8% blood and 29% lipids, hemoglobin accounts for most of the absorption at NIR wavelengths with a total absorption no more than 65% (Frangioni 2003; Lim et al. 2003). Thus, employing therapeutic options in this region of the spectrum allows for deeper cancerous tissue penetration and nanoparticle targeting while maintaining minimum absorption of light by nearby healthy cells.

1.2.1.3 After light reaches the targeted tissue, maximum light absorption by nanoparticles can be achieved by taking advantage of plasmonic effects. While spherical nanoparticles have maximum absorption peaks in the visible spectrum, a variety of other nanoparticle morphologies with strong NIR absorption peaks have been developed. A few of the most popular choices include gold nanoshells (structures composed of a dielectric core covered by a thin layer of gold) (Day et al. 2011; André M Gobin et al. 2007; L_R Hirsch et al. 2003; Lal et al. 2008; Loo et al. 2005), gold nanorods (elongated ellipsoid structures) (Dickerson et al. 2008; X. Huang et al. 2006; von Maltzahn et al. 2009; Y. Wang et al. 2013) and gold nanocages (hollow nanostructures with porous walls) (Au et al. 2008; Jingyi Chen et al. 2010c; Mackey et al. 2013; Skrabalak et al. 2007).

1.2.1.4 Some of the most pioneering work in the field of photothermal treatment was performed by Hirsch and co-workers in 2003. The authors proposed the novel, at the time, idea of in vitro incubating human breast carcinoma cells with gold nanoshells. After illuminating the cells with a laser at wavelength of 820 nm and an irradiance of 35 W/cm², the authors observed photothermally induced morbidity. No effects were shown on cells

not treated with nanoparticles (L_R Hirsch et al. 2003). Some of the first in vivo experiments were performed by O'Neil et al. in 2004. They demonstrated the feasibility of the method, developed by Hirsch and co, on mice with murine colon cancer by initially functionalizing nanoshells of 130 nm in diameter with polyethylene glycol (PEG) for biocompatibility and then intravenously introducing the solution to the mice to be treated. Nanoparticle illumination was achieved through the use of a diode laser operating at a wavelength of 808 nm with an irradiance of 4 W/cm². All treated mice appeared healthy and tumor free after 90 days (O'Neal et al. 2004).

1.2.1.5 The use of gold nanorods for photothermal therapy was first introduced by the El-Sayed group in 2006. The group managed to appropriately modify the aspect ratio of gold nanorods thus allowing for strong absorption peaks in the NIR. Then, a series of in vitro experiments were performed to demonstrate the capabilities of their nanoparticle design. After functionalizing the nanorods with anti-epidermal growth factor receptor (anti-EGFR) monoclonal antibodies, the authors introduced the nanoparticles into a culture of nonmalignant epithelial cells (HaCat) and two cultures of malignant oral epithelial cell lines (HOC 313 clone8 and HSC 3). The properly functionalized nanoparticles were then shown to bind only to the malignant cells due to the overexpressed EGFR on the cytoplasmic membrane of the malignant cells and after continuous laser illumination at a wavelength of 800 nm the malignant cells were destroyed. Their work represents one of the early examples of theranostics where cancer cell diagnosis and treatment are possible through the use of gold nanoparticles (X. Huang et al. 2006). The same group also introduced some of the first in vivo experiments on mice in 2008. Through the introduction

of PEG-treated nanorods in the cancerous tissue and subsequent illumination in the NIR, the authors were able to demonstrate significant tumor size decreases in the treated mice population (Dickerson et al. 2008).

1.2.1.6 Gold nanocages were introduced to the field of photothermal therapy through an early study performed by L. Au et al. The authors studied the effectiveness of photothermal therapy using gold nanocages by examining breast cancer cell death rate. Initially, through coating nanocages with monoclonal antibodies they were able to attach nanocages to the cell membrane or even achieve endocytosis. After performing a pulsed laser illumination parametric study, they established the illumination power intensity and duration required to achieve irreversible cellular damage. The percentage of cellular damage was measured using flow cytometry coupled with propidium iodide staining (Au et al. 2008). One of the first in vivo investigations of the photothermal application of gold nanocages was performed by J. Chen et al. on mice injected with U87wtEGFR tumor cells. Due to malfunctioning lymphatic system and wide interendothelial junctions, the nanocage concentration was found to be higher in the tumor area because of enhanced permeability and retention. The nanocages were subsequently illuminated by diode laser for 10 min causing a sudden increase in temperature which resulted in irreversible damage to tumor cells. The damage was evaluated by changes to tumor metabolism using F-FDG PET and confirmed through histological examination (Jingyi Chen et al. 2010c). In a recent comparison study by Y Wang et al, nanocages have been shown to be much better photothermal transducers as opposed to nanoshells and nanorods. Based on their analysis, nanocages represent the optimal choice for photothermal energy

conversion per Au atom in vitro followed by nanohexapods and then nanorods. More specifically, in their photothermal efficiency investigation, a solution of gold nanocages was compared to solutions of gold nanohexapods and gold nanorods and despite having the lowest concentration, the overall photothermal performance of the nanocages was the highest (Y. Wang et al. 2013).

1.2.1.7 In spite of its demonstrated therapeutic capabilities, photothermal therapy still remains at its infancy and hasn't quickly translated from the lab to the clinic perhaps because of certain disadvantages that it presents. In most of the studies mentioned above the authors used hyperthermia to induce cancer cell death. However, hyperthermia is a slow process which might result in potential collateral damage to nearby tissues and if combined with photothermal drug delivery for increased effectiveness, specific agents that might have undesired cytotoxicity are also introduced. In addition, there is a wealth of evidence indicating that this method of treatment lacks therapeutic potential in cases of low nanoparticle targeting specificity due to tumor cell heterogeneity, resistance of phenotypes (Cho et al. 2008; Jemal et al. 2009; Peer et al. 2007) as well as cases prone to nanoparticle or energy delivery toxicity (Cherukuri et al. 2010; Choi et al. 2011; Gilstrap et al. 2011; Andre M Gobin et al. 2005; H.-C. Huang et al. 2011; Huff et al. 2007; Li et al. 2009; Pitsillides et al. 2003; Yuan et al. 2012). As a viable alternative to photothermal therapy's shortcomings, we propose the use of plasmonic nanobubbles.

1.2.2 Nanobubble Treatment

1.2.2.1 The principles of nanobubble therapy lie in the synergistic effect of nanoparticle agglomeration and phase-change induced mechanical damage in tumor sites. In this approach, the nanoparticles are introduced into the vasculature and find their way to cancerous tissue where they are up-taken by bio-targeted unwanted cells. Once within the vicinity, the nanoparticles are heated using a pulsed laser with sufficient intensity to selectively generate a thin film of vapor that leads to the destruction of malignant cells by rupturing their membrane. This technique, compared to other nanoparticle medicine solutions, presents an alternative with various advantages: (a) plasmonic nanobubbles can be generated on-demand with high temporal and spatial resolution; (b) the size of the occurring nanobubble size and nucleation energy required depend on the localized concentration of nanoparticles. Higher concentration of nanoparticles in tumor cells results in a lower energy threshold for nanobubble formation due to cooperative heating. Hence, by carefully tuning laser fluence minimal damage is caused to nearby healthy cells (D. O. Lapotko et al. 2006a; E. Y. Lukianova-Hleb et al. 2012a; E. Y. Lukianova-Hleb and Lapotko 2014), (c) plasmonic nanobubbles can be used to inflict direct mechanical damage to a cell's membrane thus nullifying the requirement for specialized drugs. This mechanical process results in immediate lysis of the targeted cancer cells rather than apoptosis or necrosis; (d) the entire process requires only a few nanoseconds to perform rather than approximately 10 min for hyperthermia; (e) apart from mechanical destruction, nanobubbles can also be used for drug delivery for a synergistic effect (E. Y. Lukianova-Hleb and Lapotko 2014).

1.2.2.2 Contrary to continuous wave (CW) illumination used in most hyperthermia studies, nanobubble therapy employs pulsed laser illumination of nanosecond intervals or smaller (refer to paragraph 1.1.2.4). In a very preliminary study, Hartland et al. were the first to experimentally characterize the fundamental energy dissipation mechanisms in femto-second pulsed laser illuminated Au nanospheres (Hartland and Hu 2002; Hartland et al. 2003) but a more recent analysis by Pitsillides et al. in 2003 represents one of the earliest examples of generating nanobubbles through the more efficient method of pulsed illumination. The authors of the latter, performed a series of experiments involving illumination of gold nanoparticles in the visible range of the EM spectrum. Their analysis indicated that when pulsed illumination was employed, the brief but intense temperature increase following a short laser pulse yields fast vaporization of the fluid layer surrounding the nanoparticle causing more efficient cell denaturation as opposed to CW illumination (Pitsillides et al. 2003).

1.2.2.3 A brief survey of literature in this field reveals a wealth of early research work focused on nanobubble treatment by several groups (Huttmann et al. 2002; Huttmann et al. 2005; Letfullin et al. 2006; Pitsillides et al. 2003). One of the first studies focused on the bioapplications of nanobubbles was performed by Lapotko et al. in 2006. The researchers studied the effects of explosive nucleation from cluster of nanoparticles on human leukemia cells taken from bone marrow tissue. The group used spherical nanoparticles coated with cancer-cell specific monoclonal antibodies in order to increase the concentration of nanoparticles in target cells through endocytosis. Since clusters of nanoparticles require less energy to achieve and sustain nanobubble nucleation, by

illuminating the nanoparticles with a 532 nm laser for 10 ns with an irradiance of 0.6 J/cm², the authors managed to achieve a cancer cell death rate of more than 99% with a single laser pulse. Surrounding healthy cells were largely unaffected and had a survival rate of up to 84%. This preliminary work established nanobubble-induced lysis as a reliable and highly specific treatment method that mostly depends on the size of the nanoparticle cluster and the laser radiation properties rather than specific cell characteristics (D. O. Lapotko et al. 2006a). Further research from the same group in the field of nanobubbles for imaging, diagnosis and therapeutic applications at the cellular level verified and expanded the initial results (D. Lapotko et al. 2006b; D. O. Lapotko et al. 2006a; D. Lapotko 2009a, 2009b, 2009c).

1.2.2.4 More recently, Chen et al. revealed that the nanobubble dynamics are dependent on the laser irradiance and directly responsible for the rupture of the cell membrane. It was experimentally determined that the number of nanorods required for the perforation of the plasma membrane directly depends on the energy effluence (C. L. Chen et al. 2010a). An example of their work can be seen in **Fig 1.4**.

1.2.2.5 In numerous published works, Lukianova et al. demonstrated the use of gold nanoparticles and nanobubbles as a method for effective intracellular drug delivery (E. Y. Lukianova-Hleb et al. 2011; E. Y. Lukianova-Hleb et al. 2012b). More specifically, the authors investigated the cooperative effects of plasmonic nanobubbles and drug delivery in an in vivo and in vitro study on head and neck squamous cell carcinoma (HNSCC). A combination of 20 and 60 nm gold nanospheres along with Doxorubicin

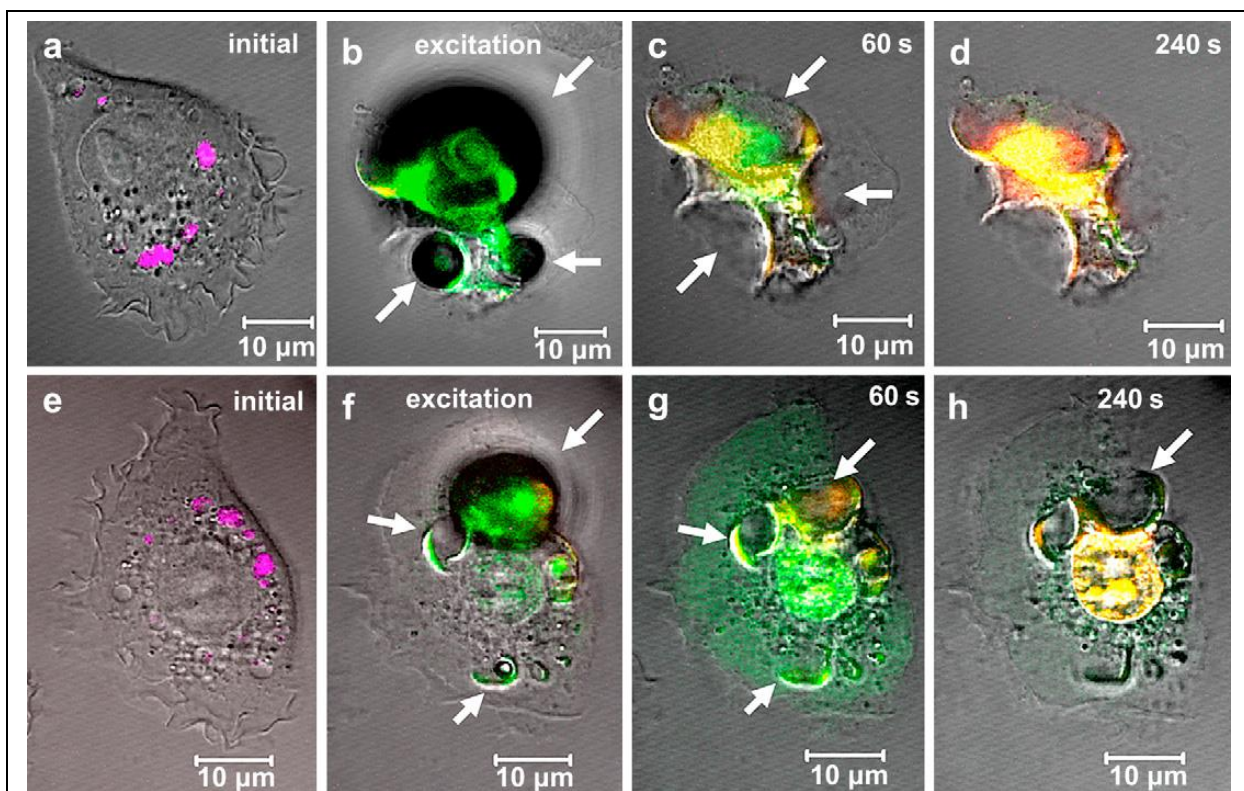


Figure 1.4. In-situ photothermolysis of living EMT-6 tumor cells by thermal explosions triggered by laser-illuminated gold nanorods. Laser Irradiance (a-d) 113 mJ/cm², (e-h) 93 mJ/cm² (C.L. Chen et al. 2010a)

encapsulated into 85 nm liposomes was used to cause an explosive impact that would immediately disrupt the liposome and endosome membranes while the pressure released by the plasmonic nanobubble would trigger a highly localized drug ejection. Ultrasound analysis was used to determine when the nanobubble-enhanced drug delivery was triggered. A level of necrosis of more than 90% was achieved (for low penetration depths) while the method's high selectivity prevented damage to nearby healthy cells (E. Y. Lukianova-Hleb et al. 2012a).

1.2.2.6 Compared to experimental work, relatively few computational models on the behavior of plasmonic nanobubbles have been reported. For instance, Volkov et al.

introduced a one-dimensional (1D) hydrodynamic computational model for predicting femtosecond-pulsed laser heating of spherical nanoparticles. Their work suggests that biological damage can be restricted to within a short distance (relative to the particle diameter) from the illuminated particle (Volkov et al. 2007). Yet, 1D analyses have inherent limitations since they can be applied only in cases of spherical nanoparticles. In a more recent study by Lombard et al. it was computationally demonstrated via a hydrodynamic free energy model that the temporal evolution of the size of nanobubbles is an asymmetrical process consisting of an adiabatic expansion followed by an isothermal collapse (Lombard et al. 2014). Their model provides good insight on the thermodynamic nature of nanobubble expansion and collapse phases but lacks generalization. Thus, it could be possible that even computational models developed so far, most likely lack the rigor required to describe all the details of the nanobubble treatment process.

1.2.2.7 From this brief literature survey it can be concluded that plasmonic nanobubble treatment represents a potentially safer and more effective alternative to photothermal therapy. Despite the recent experimental progress in this field, relatively few theoretical studies have emerged, let alone, focused on the details of plasmon-assisted bubble nucleation and the subsequent bubble and fluid dynamics as described here. In the majority of the aforementioned studies researchers used spherical nanoparticles particularly functionalized to achieve aggregation in cells of interest. The ensuing illumination was then performed, in certain cases, at off-plasmon resonance or non “therapeutic window” wavelengths leading to the potential generation of non-specific nanobubbles and limited penetration in cancerous tissue. This process cannot be directly

regulated, due to the random location of nanoparticles in colloids or in vivo aggregates and might have unwanted side effects such as destruction of healthy cells, without lengthy calibration. For successful treatment, most experimentalists still rely on simplified nanoparticle morphologies, theoretical approximations and trial-error. Therefore, there is a significant knowledge gap concerning the specific details of photothermal energy conversion such as the required wavelength to achieve plasmon resonance and the required energy and pulse duration for various geometries. Since, to the best of our knowledge, very few theoretical studies addressing the aforementioned have been reported, the need arises for a new approach of studying pulsed-laser plasmon-assisted nanoscale bubble nucleation using combined computational electromagnetic and CFD-based fluidic analysis for a number of nanostructure morphologies; thus combining the advantages of employing complex morphologies (e.g. high average absorption in the NIR) with those of nanobubble treatment (e.g. specificity) resulting in a more effective and controlled method of cancer therapy. This approach, proposed herein, enables fundamental understanding and rational design of plasmon-based photothermal processes and should prove useful for the development of novel photothermal applications.

Chapter 2: Theory and Methods

2.0 The plasmon-based photothermal process studied here is highly complex. It involves coupled phenomena that span multiple length and time scales, which depend on the duration and power level of the laser pulse. A rigorous analysis of this process would require concurrent multiscale modelling that encompasses quantum to continuum level theory. To the best of our knowledge, no such models have been reported. Previous theoretical studies in this field are based to some extent on simplifying assumptions. In this work, we make the assumption that the photothermal process can be modelled using continuum theory over the range of variables that we consider. The continuum approach can be justified based on several factors. To begin with, we consider laser pulse durations of multiple nanoseconds, which is longer than the characteristic time constants of the transient non-equilibrium photothermal effects such as electron-electron scattering (10-50 fs), electron-phonon/lattice interactions (10 - 50 ps), and phonon-phonon interactions at the surface of the particle ($\sim 100 - 400$ ps) (Roper et al. 2007). Second, we study the response of metallic nanoparticles with dimensions (~ 60 nm) that are greater than the phonon mean free path (~ 20 nm in gold) (Pattamatta and Madnia 2010). Therefore, the phonon Knudsen number is ~ 0.3 , which implies that continuum thermal analysis can provide a reasonable estimate of thermal behavior. Similarly, as it will be shown in the following chapters below, nucleated bubbles have dimensions (~ 60 nm) that are greater than the mean free path ($\sim 10 - 15$ nm) of the vapor molecules within them. Thus, the Knudsen number for the gas dynamics is ~ 0.25 . The fluidic domain is on the order of 200-300 nm, which is suitable for continuum fluid dynamics. Finally, in order to account

for the complexity and multidimensionality of the problem, we make combined use of computational fluid dynamics (CFD) to predict coupled thermal fluid phase change effects and computational electromagnetics to predict photonic effects. In this chapter we will describe the key theoretical principles and methods used to achieve this objective. The equations used can be found in subsections 2.1 and 2.2, respectively.

2.1 Photonic Analysis

2.1.1 Spherical Nanoparticles

2.1.1.1 Although the basic underlying principles regarding spherical nanoparticles are briefly described in Chapter 1, it would be instructive to explain some of the theory regarding their absorption of light when submerged in fluid. For this case, the irradiance of the incident laser I_{inc} is given by:

$$I_{inc} = \frac{c\epsilon_0 n_f}{2} |E_{inc}|^2 \quad (2.1)$$

where c is the speed of light in vacuum, ϵ_0 is the permittivity of free space, n_f is the refractive index of the fluid and E_{inc} is the incident electric field. Throughout this analysis, we have $E_{inc} = 2 \times 10^6$ V/m and therefore the nominal irradiance for all of our photonic simulations is $I_{inc} = 7$ mW/ μm^2 . We can then compute the absorbed power (Q_{abs}) using an analytical approach, which is based on Rayleigh scattering theory (van de Hulst 1981):

$$Q_{abs} = k \text{Im}(\alpha) I_{inc} \quad (2.2)$$

where $k = 2\pi n_f / \lambda$ and α is the complex-valued polarizability of the sphere:

$$\alpha = \frac{4\pi \alpha_0 \epsilon_0}{\left[1 - \alpha_0 \left(\frac{k^2}{a} - \frac{2}{3} i k^3 \right) \right]} \quad (2.3)$$

where $\alpha_0 = R_p^3(\epsilon_r - 1)/(\epsilon_r + 2)$ and R_p and ϵ_r are the radius and relative permittivity of the sphere, respectively (Furlani and Baev 2009b). This analytical approach can be used to estimate the heat generated by a spherical nanoparticle submerged in fluid but is not applicable for more complex nanoparticle geometries and yields a somewhat lower and narrower absorption profile because it is based on a dipole approximation, whereas the numerical model described in the following section is geometry independent and gives more accurate results since it takes into account absorption and scattering due to higher order multiple terms.

2.1.2 Numerical Field Analysis

2.1.2.1 For more complex geometries, the photonic response of metallic nanoparticles in fluid is predicted using numerical three-dimensional (3D) full-wave time-harmonic field theory which accounts for all the principles discussed above. In this case, Maxwell's equations are solved assuming an E-field time dependence of the form:

$$E = E(x)e^{i\omega t} \quad (2.4)$$

where ω is the angular frequency of incident light. For cases of nanoparticles immersed in fluid, we use transverse electromagnetic (TEM) analysis where the equation for the electric field can be written as:

$$\nabla \times (\mu_r^{-1} \nabla \times \mathbf{E}) - k_0^2 \left(\epsilon_r - j \frac{\sigma}{\omega \epsilon_0} \right) \mathbf{E} = 0 \quad (2.5)$$

where μ_r , ϵ_r and σ are the relative permeability, permittivity and conductivity of the various constituent materials, respectively while k_0 is the free space wavenumber and can be defines as $k_0 = \omega/c$. For gold nanoparticles at optical frequencies, $\mu_r = 1$ and ϵ_r is modeled using a complex valued analytical expression that is based on the Drude-Lorentz model and matches the measured optical response of gold. It can be written as:

$$\epsilon_{r,Au}(\lambda) = \epsilon_\infty - \frac{1}{\lambda_p^2 \left(\frac{1}{\lambda^2} - i \frac{1}{\gamma_p \lambda} \right)} + \sum_{n=1,2} \frac{A_n}{\lambda_n} \left[\frac{e^{i\phi_n}}{\left(\frac{1}{\lambda_n} - \frac{1}{\lambda} + i \frac{1}{\gamma_n} \right)} + \frac{e^{-i\phi_n}}{\left(\frac{1}{\lambda_n} + \frac{1}{\lambda} - i \frac{1}{\gamma_n} \right)} \right] \quad (2.6)$$

A more thorough description of this expression and its various parameters is given in the references (Etchegoin et al. 2006, 2007; Johnson and Christy 1972). It is important to note that **Eq. (2.6)** is valid for a time-harmonic dependence of the form $\exp(-i\omega t)$. However, we use the COMSOL RF program (www.comsol.com) for the photonic analysis, which is based on an $\exp(i\omega t)$ time-harmonic dependence. Therefore, ϵ_r in our analysis is obtained by replacing the imaginary terms in **Eq. (2.3)** with their complex conjugates (i.e. by replacing i by $-i$). The fluid surrounding the nanoparticle is assumed to be non-absorbing water with an index of refraction of $n_f = 1.333$.

2.1.2.2 Throughout our work, the magnitude of the surface current is chosen to provide a plane wave in the fluid with a peak amplitude of $E_x = 2 \times 10^6$ V/m (in the absence of the nanoparticles). This choice of field amplitude is arbitrary as we are ultimately

interested in the power absorbed by the particle Q_{abs} (W) per unit irradiance I_{inc} (W/m²). The absorbed power, which is wavelength dependent, is converted to heat and thus this analysis predicts photothermal energy conversion within the particle. The power level in the nanoparticle and corresponding pulse duration that are needed to nucleate and sustain a bubble without damaging the particle are computed using a CFD analysis as described in the next section. Once a viable power level is known, the laser irradiance required to generate this power within the nanoparticle is computed from the photonic analysis.

2.2 Fluidic Analysis

2.2.1 Temperature and Flow Fields

2.2.1.1 The fluidic analysis is performed using computational fluid dynamics (CFD) and is used to predict thermal, pressure and flow effects including the temperature rise in the particle, heat transfer from the particle to the fluid, phase change within the fluid leading to homogeneous bubble nucleation, the dynamic behavior of the bubble as it expands and collapses, and the temperature, pressure and flow throughout the fluid during the entire process. The fluidic analysis is used to determine the threshold power and pulse duration needed to generate and sustain a bubble with a desired dynamic behavior. Once this is understood, the laser intensity needed to produce the threshold power within the particle is back-calculated from the photonic analysis. The thermofluidic analysis is based on the following assumptions: For simplicity and better result reproducibility, we consider all fluid and solid properties as constant throughout the photothermal cycle. As a result, we also consider the nanoparticle size variations (maximum of ~1.5% increase) caused by density changes due to heating as negligible (V. Pustovalov et al. 2008). The shape of the nanoparticle is assumed to remain unaltered for all simulations and any mechanical damage to the nanoparticle from the pressure generated by the nanobubble is considered trivial because of the inherent structural rigidity of the metal structure and the symmetry of the nucleated nanobubble. Finally, we assume that no heat transfer occurs from the nanoparticle to the surrounding gas post-

nucleation since energy losses to the rarefied gas are significantly lower compared to the effects of laser heating.

2.2.1.2 The volume of fluid (VOF) method as implemented in the Flow3D software (www.flow3d.com) is used for this analysis (Hirt and Nichols 1981). The fluid is assumed to be incompressible and Newtonian with surface tension σ , viscosity μ , density ρ , specific heat at constant pressure c_p and thermal conductivity k . These are assumed to be constant in our initial analysis. The general equations governing momentum and heat transfer are as follows:

Navier-Stokes:

$$\rho \left(\frac{\partial \mathbf{v}}{\partial t} + \mathbf{v} \cdot \nabla \mathbf{v} \right) = -\nabla p + \mu \nabla^2 \mathbf{v} \quad (2.7)$$

Continuity:

$$\nabla \cdot \mathbf{v} = 0 \quad (2.8)$$

Heat transfer:

$$\rho c_p \left(\frac{\partial T}{\partial t} + \mathbf{v} \cdot \nabla T \right) = k \nabla^2 T \quad (\text{fluid}) \quad (2.9)$$

$$\rho_{np} c_{np} \frac{\partial T_{np}}{\partial t} = Q_{abs}(t) + k_{np} \nabla^2 T_{np} \quad (\text{nanoparticle}) \quad (2.10)$$

where \mathbf{v} and p are the velocity and pressure in the fluid and ρ_{np} , c_{np} and k_{np} are the density, specific heat at constant pressure and thermal conductivity of the nanoparticle,

respectively. Q_{abs} is the power generated uniformly within by the nanoparticle due to absorption of incident laser light while T and T_{np} are the corresponding temperatures in the fluid and the nanoparticle, respectively. For our initial approach, we study the behavior of gold nanoparticles using the following material properties: $\rho_{gold} = 19,300 \text{ kg/m}^3$, $c_{gold} = 129 \text{ J/kg}\cdot\text{K}$ and $k_{gold} = 317 \text{ W/m}\cdot\text{K}$. Similarly, in all our simulations, the gold nanoparticles are immersed in an aqueous solution, which has the properties of water at 300 K. The surface tension contact angle for the nanoparticle is assumed to be 30° .

2.2.1.3 In addition to the physical equations, initial and boundary conditions are imposed to obtain a consistent theory. Heat transfer at the particle-fluid interface is determined using an effective transfer coefficient that takes into account local variations in thermal conduction and convection at this surface. This coefficient can vary along the surface, especially when its shape changes, as in the case of a nanorod. The variation in this coefficient can impact the local formation and growth of a bubble.

2.2.2 Phase Change and Bubble Dynamics

2.2.2.1 Phase change that initiates bubble nucleation occurs when the fluid reaches its superheat temperature at the surface of the particle, which is taken to be $T = 580\text{K}$ for H_2O . Before nucleation, the temperature in the particle and surrounding fluid is calculated based on **Eqs. (2.9)** and **(2.10)**. Heat transfer at the particle-fluid interface is predicted using a local effective transfer coefficient that is dynamically determined. Once a bubble is nucleated, its interface is tracked using the VOF method. The pressure in the bubble is

initially set to the saturation pressure at the superheat temperature (approximately 100 atm), which is computed using the Clausius-Clayperon equation:

$$p_{sat}(T) = p_1 \exp \left[\frac{\Delta H_{vap}}{R} \left(\frac{1}{T_1} - \frac{1}{T} \right) \right] \quad (2.11)$$

where p_1 and T_1 are the pressure and temperature at a point on the saturation curve (e.g. $p_1 = 100$ kPa, $T_1 = 273$ K), ΔH_{vap} (40.65×10^3 J/mol) is the molar enthalpy of vaporization and R (8.314 J/mol·K) is the universal gas constant. This pressure exerts an outward force at the liquid-vapor interface that causes the vapor region to expand into a bubble. As the bubble evolves, the pressure p_{vap} , temperature T_{vap} and density ρ_{vap} of the vapor within it are computed using the equation-of-state of an ideal gas:

$$p_{vap} = (\gamma - 1) \rho_{vap} C_{vap,v} T_{vap} \quad (2.12)$$

where C_{vap} is the specific heat of the vapor at constant volume and $\gamma = C_{vap,p}/C_{vap,v}$ is the ratio of specific heats. The pressure, temperature and density are assumed to be spatially uniform (i.e. homogeneous) within the bubble. The mass flux \dot{m} at the fluid-bubble interface is taken to be proportional to the deviation of the fluid from its saturation conditions:

$$\dot{m} = \sqrt{\frac{MW}{2\pi R}} \left(c_{evap} \frac{p_l^{sat}}{\sqrt{T_l}} - c_{cond} \frac{P_{vap}}{\sqrt{T_{vap}}} \right) \quad (2.13)$$

where MW is the molecular weight of the vapor, R the vapor gas constant, T is temperature (K), and the subscripts l and vap refer to liquid and vapor phases, respectively. The term p_l is the saturation pressure corresponding to the liquid temperature T_l , and c_{evap} and c_{cond} are accommodation coefficients for evaporation and condensation.

2.2.2.2 After the bubble has nucleated, the nanoparticle is surrounded by vapor and there is negligible heat transfer at the particle-vapor interface. Thus, if the laser pulse continues beyond nucleation, the temperature of the nanoparticle will rise rapidly as it absorbs incident light while being essentially insulated. Under this condition, the nanoparticle can reach its melting or even vaporization temperature within a nanosecond or less. For bulk gold, these values are $T_m = 1336$ K and $T_{vap} = 2933$ K, respectively. However, experiments have shown that Au nanoparticles have a lower melting point that can differ by as much as 200 K from the bulk value. Specifically, the experimentally observed surface melting temperature of a 38 nm gold nanoparticle, which is smaller than the nanoparticles we consider, was found to be ~ 1067 K (Inasawa et al. 2005). Additional experiments performed on gold nanoparticles show significant surface melting effects can occur even at lower temperatures, given a sufficiently long period of time (timescales ranging from hours to days). As an example, nanorods of various lengths can be converted into spheres at 523 K in 60 min (Petrova et al. 2006). In order to avoid high temperature damage to the particle, the laser power level and pulse duration must be carefully chosen, with special attention given to laser heating immediately after bubble nucleation while the nanoparticle is essentially insulated. We use modelling to carefully

select the laser pulse duration so as to constrain the heating to keep the nanoparticle below a maximum temperature of 1100 K. The modelling approach suggested here enables rapid parametric screening to achieve this goal for a variety of nanoparticle geometries such as nanospheres, nanorods, nanotori, nanorings and nanocages/nanoframes.

Chapter 3: Combined Computational Modeling

In this chapter, we will describe the development of computational electromagnetic and CFD-based models for various nanoparticle geometries. The nanoparticle geometries that represent the focus of our research are nanospheres, nanorods, nanotori, nanorings and nanocages/nanoframes. As described in the previous chapter, two types of computational models will be developed: a) Computational Electromagnetics models for the photonic analysis will be used to calculate the plasmon resonance wavelength and the photothermal energy conversion within the nanoparticles, i.e. the time-averaged power absorbed by a particle as a function of the wavelength, intensity and polarization of the incident light and b) CFD models that predict thermal, pressure and flow effects including the temperature rise in the particle, heat transfer from the particle to the fluid, phase change within the fluid leading to homogeneous bubble nucleation, the dynamic behavior of the bubble as it expands and collapses, and the temperature, pressure and flow throughout the fluid during the entire process. In order to achieve that goal, we will employ state-of-the-art customizable software packages including but not limited to: FLOW 3D versions 10.1 and 11.1 from Flow Science Corp. (www.flow3d.com) and COMSOL Multiphysics Software (www.comsol.com) versions 4.4 and 5.2 with full CFD-FSI, nanofluidics and RF analysis capabilities, respectively. Simulation results will also be compared with analytical methods where applicable. The modeling effort will follow the assumptions stated in Chapter 2 and will be used to determine heretofore unknown properties such as the plasmon resonance wavelength, the amount of power required to generate and sustain nanobubbles without melting the nanoparticles and the size and duration of occurring nanobubbles for each nanoparticle geometry.

3.1 Nanospheres

3.1.1 Synthesis

3.1.1.1 The modeling effort begins with an analysis of the most common nanoparticle geometry: the nanosphere. The synthesis of gold spherical nanoparticles is one of the oldest known fabrication techniques and is traditionally carried out through a citrate reduction bottom-up process. This technique, which still remains popular today, was first reported by Turkevich in 1951 and involves the mixing of gold salt and citrate stirred in a water solution. It can lead to the fabrication of nanoparticles with a diameter ranging between 16 and 147 nm. The size distribution of the yielded nanospheres is controlled by the temperature, the ratio of gold to citrate and the order of addition of the reagents used (Daniel and Astruc 2004; Frens 1973; Turkevich et al. 1951).

3.1.1.2 However, the fabrication technique that has potentially had the most considerable impact in the field is the Brust-Schiffrin method published in 1994. This represents a more accurate fabrication procedure which allows the facile synthesis of air-stable and thermally-stable gold nanoparticles of reduced dispersity and controlled size. Nanospheres generated through this process have diameters from 1.5 to 5.2 nm, they can be repeatedly isolated and re-dissolved in a variety of organic solvents without risk of decomposition and they can be easily handled and appropriately functionalized for any application, behaving similarly to other stable organic compounds. The method itself is based on Faraday's two phase system (Faraday 1857) and makes use of thiol ligands

that bind to gold through thiolate monolayer chemistry (Mathias Brust et al. 1994; M Brust et al. 1995).

3.1.1.3 Another notable synthesis method for larger spherical nanoparticles, as those shown in **Fig 3.1**, is the seeding technique. This method starts with a colloid of small nanospheres at which a reducing agent is added. The mixture is then introduced into a growth solution with more metal ions and surfactant to induce anisotropic growth. Usually sodium borohydride is used as an initial

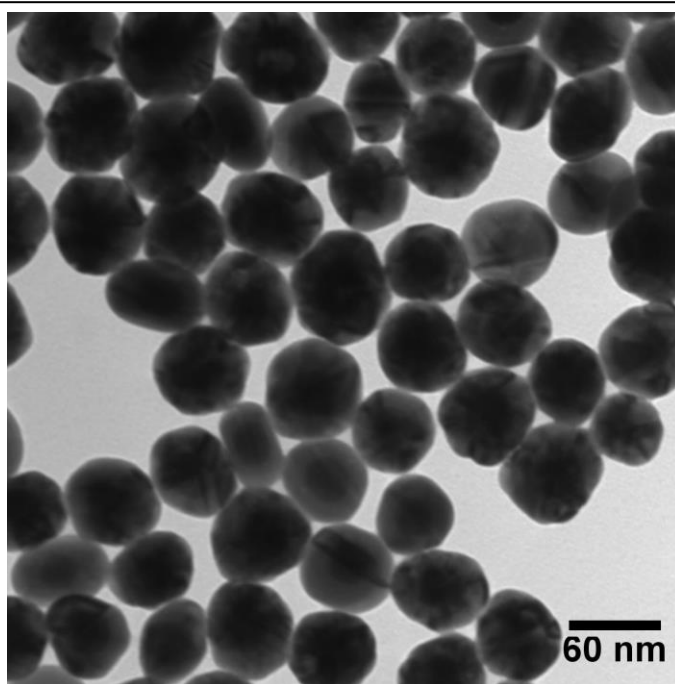


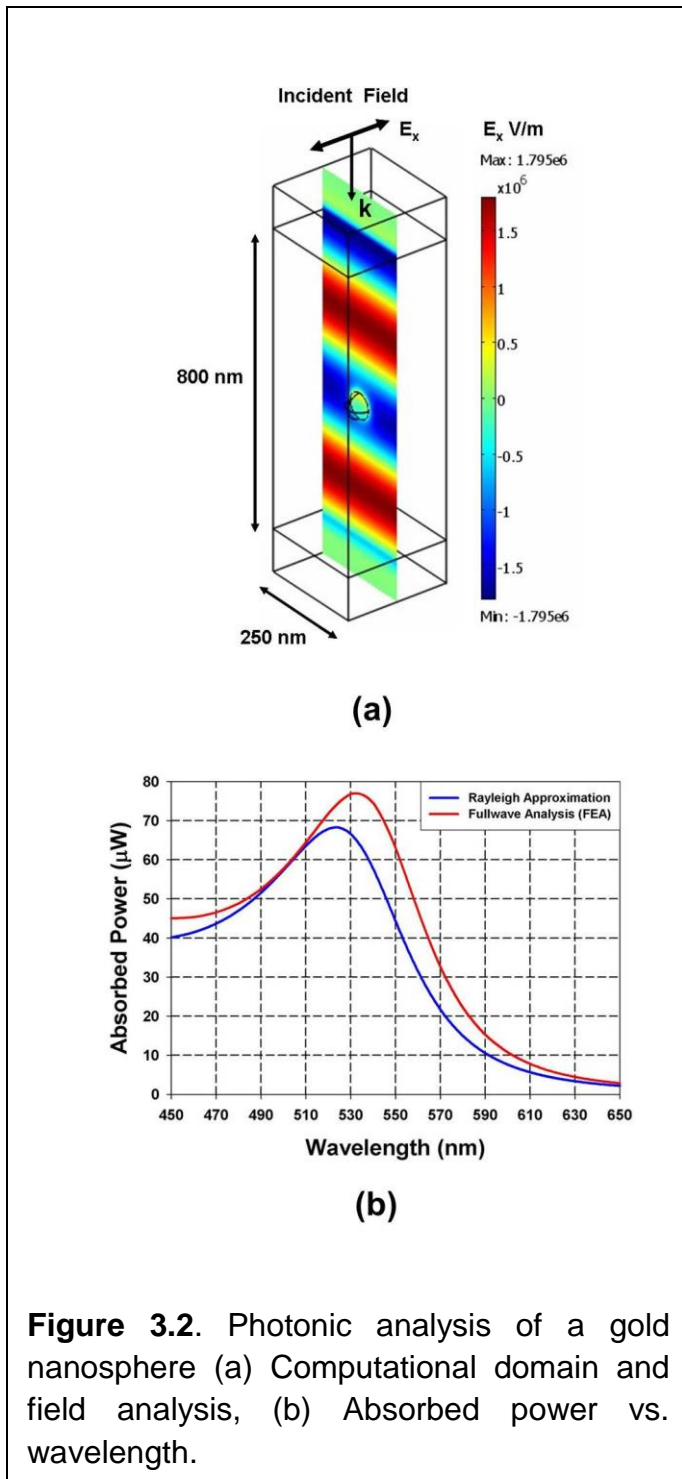
Figure 3.1. Scanning electron microscopy (SEM) image illustrating gold nanospheres with an average diameter of 60 nm (source: www.nanocomposix.com).

reducing agent while a weaker agent such as ascorbic acid is used in the growth solution to reduce the metal salt to an intermediate state so that only catalyzed reduction on the nanoparticle surface is allowed. A variation of this technique can also be applied for the synthesis of nanorods (Murphy et al. 2005). More information on the history and the details of the various fabrication processes of gold nanospheres can be found in an excellent review from M.C. Daniel and D. Astruc (Daniel and Astruc 2004).

3.1.1.4 Now that the basics of fabrication are understood let's turn our attention to the computational modeling of nanospheres for nanobubble treatment. Similarly to all the cases studied here, nanospheres will be initially modeled in isolation, as single particle system. As part of this approach all material properties are considered constant. A photonic analysis is performed to quantify photothermal energy conversion within the sphere. The power absorbed by the sphere $Q_{abs}(\lambda)$ is computed as a function wavelength at a nominal irradiance with TEM field polarization. The wavelength that produces the highest absorption is identified as the plasmon resonant wavelength. Once the photonic analysis is complete, a CFD analysis is performed to determine a power level for heat generation within the nanosphere and a corresponding pulse duration that are sufficient to create bubble nucleation without irreversible damage to the particle, i.e. keeping its peak temperature below its melting or even vaporization temperature. Once the viable power level and pulse duration are known, the laser irradiance needed to generate this power is back-calculated from the results of the photonic analysis.

3.1.2 Photonic Simulations

3.1.2.1 For analysis purposes, we have chosen to model a nanosphere with a diameter of 60 nm using the finite element (FE) method as implemented by COMSOL Multiphysics (www.comsol.com) and analytical techniques. The numerical solution method which remains the same for all geometries can be briefly summarized in the following eight steps: a) Discretization of the solution region (computational domain) into a finite number of sub-regions (elements) and labeling of the nodes that define each



element; b) User choice of an approximating function for each element's field solution; c) Numerical solution at each element as a function of the nodal values and the spatial variables from the element; d) Definition and evaluation of energy functional for the field equation over each element to obtain an expression for the energy in each element in terms of its nodal values; e) Compilation of a global energy expression as a sum of the energy of the individual elements; f) Simplification of the global energy expression with respect to the unknown nodal values, which results to algebraic equations for the nodal values; g) Solution of the system of equations to determine the nodal values and finally; h) Assembly of the

desired solution from a compilation of nodal values. In the case of a nanosphere with a diameter of 60 nm, the computational domain spans 1000 nm in the direction of

propagation (**z**-axis), and 250 nm in both the **x** and **y** directions. The nanosphere is centered at the origin (**Fig. 3.2a**). Perfectly matched layers (PMLs) are applied to the top and bottom of the computational domain with a height of 100 nm. This leaves 800 nm of physical domain along the **z**-axis. Perfect electric conductor (PEC) boundary conditions are applied at the boundaries perpendicular to the **E** field at $\mathbf{x} = \pm 125$ nm, and perfect magnetic conductor (PMC) boundary conditions are applied at the boundaries perpendicular to the magnetic (**H**) field at $\mathbf{y} = \pm 125$ nm. These conditions mimic a 2D array of identical nanospheres with a center-to-center lattice spacing of 250 nm in both the **x** and **y** directions. These, boundary conditions simplify the analysis and the lattice distances are chosen to be large enough so that the resulting predictions will reflect the response of a single particle i.e. negligible coupling with neighboring particles. The sphere is illuminated with a downward directed uniform TEM plane wave with **E** parallel to the **x**-axis. The incident field is generated by a time-harmonic surface current (not shown) positioned in the **x-y** plane 400 nm above the center of the nanosphere, i.e. immediately below the upper PML as described in the references (Furlani and Baev 2009a, 2009b). We use a cubic vector finite element formulation with a total of 29,615 tetrahedral elements in the computational domain. The time-averaged power absorbed by the nanosphere was computed for a range of wavelengths that spanned 450 nm to 650 nm in 2 nm increments.

3.1.2.2 The plasmon resonance wavelength was found to be 532 nm based on the numerical analysis and the corresponding power absorbed by the nanosphere is 76 μW (with $I_{inc} = 7 \text{ mW}/\mu\text{m}^2$) as shown in **Fig. 3.2b**. The analytical approach, indicated by the

blue line in **Fig. 3.2b** as Rayleigh approximation (described in subsection 2.1.1), is also plotted and it yields a somewhat lower and narrower absorption profile because it is based on a dipole approximation, whereas the numerical model takes into account absorption and scattering due to higher order multiple terms. It is useful to note that although an isolated nanosphere of 60 nm has a plasmon resonance wavelength located in the visible spectrum, plasmonic coupling effects in nanosphere aggregates may produce an optimum absorption in the NIR which is more suitable for bioapplications (Baffou and Quidant 2013). Overall, we use the results of the photonic analysis to determine the laser irradiance needed to effect bubble nucleation, which is based on the fluidic analysis described in the following subsection.

3.1.3 Thermofluidic Simulations

3.1.3.1 A CFD analysis was performed to determine viable power levels and pulse durations that produce bubble nucleation with sustained bubble dynamics, without damaging the nanosphere. We chose such values that limit the maximum particle temperature to less than 1100 K. An axisymmetric CFD model was developed to model one quadrant of a gold sphere. The computational domain spanned 7 radii of the sphere (210 nm), with 1 nm cell widths in both the radial (r) and axial (z) direction. Symmetry boundary conditions were imposed along both the r - and z -axes. The former accounted for the lower half of the sphere, while the latter accounted for its axial symmetry. The pressure and temperature throughout the computational domain were initialized to 1 atm (1×10^5 N/m²) and $T_0 = 300$ K, respectively. A stagnation pressure condition (1×10^5

N/m²) was imposed at the outer r and z boundaries along with a Dirichlet condition set to the ambient temperature, $T_{amb} = 300$ K. These initial and boundary conditions were used for all fluidic analyses.

3.1.3.2 A preliminary CFD thermal analysis (without phase change) was performed to determine power levels and pulse durations that increase the temperature of the fluid at the interface with the sphere from its initial value ($T_0 = 300$ K) to the supercritical temperature of 580 K. We computed the temperature of the nanosphere during heating for a range of power levels and pulse durations. The latter was chosen to be from 2 to 5 ns so as to exceed the non-equilibrium time constants of the photothermal process as described in paragraph 2.0. The CFD analysis was guided by analytical formulas for heat transfer as appropriate. This preliminary analysis was performed because it is far less computationally intensive than the full phase change and bubble nucleation analysis, while at the same time providing an intuitive understanding of thermal diffusion from the sphere to the fluid up to nucleation.

3.1.3.3 Once the preliminary thermal calculations were complete, CFD simulations of bubble nucleation were performed using power levels selected from the preliminary analysis, but with slightly longer pulse durations to ensure nucleation and sustained bubble dynamics. For the nanosphere, we concluded that an adequate power for nucleation without melting was 152 μ W, with a pulse duration of 5 ns. Given these values, and the results from the photonic analysis (**Fig. 3.2a**), we determined that a laser operating at $\lambda = 532$ nm with an irradiance of $I_{inc} = 14$ mW/ μ m² is sufficient to generate a

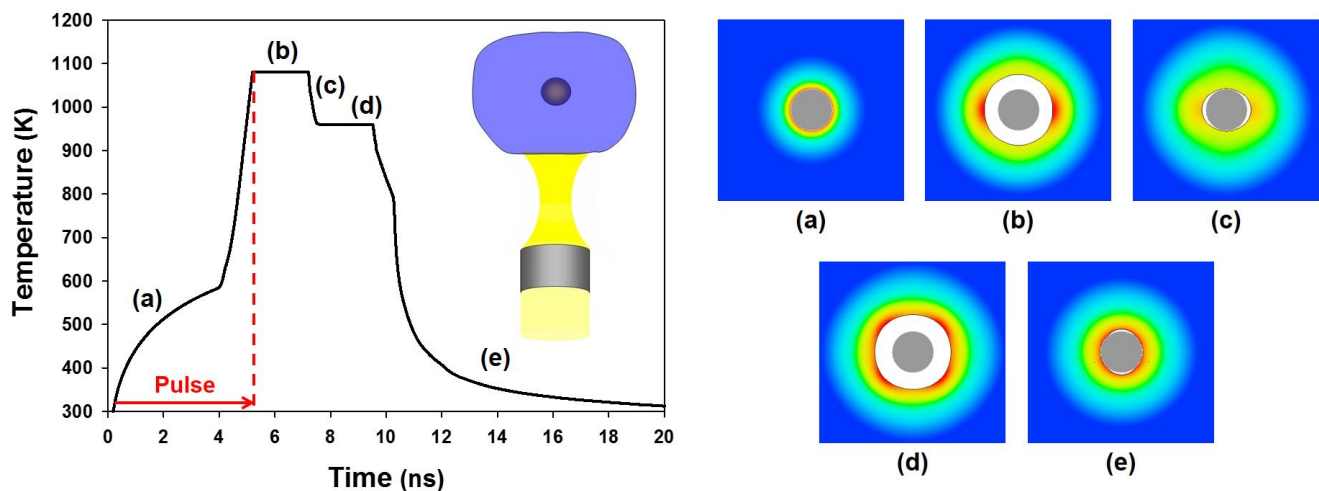


Figure 3.3. Photothermal heat cycle of a nanosphere ($R = 30$ nm) (cross-sectional view): plot of nanosphere temperature vs. time, pulse duration indicated by red arrow and dashed line and inset plots showing various phases of the thermal cycle; (a) initial heating, (b) primary nanobubble formation, (c) primary nanobubble collapse, (d) secondary nanobubble formation, (e) secondary nanobubble collapse with cooling.

bubble under controlled conditions, i.e. without melting the sphere. The fluidic analysis at this power and pulse duration is shown in **Fig. 3.3**. This plot shows the temperature of the nanosphere before, during and after the heat pulse. Various portions of the plot are labelled from (a)-(e) and there are corresponding images of the nanosphere and bubble at these times that show the generation and collapse of a primary and secondary bubble.

3.1.3.4 Initially the nanosphere and the domain are at a temperature of 300 K. After 0.2 ns the particle is illuminated and starts to heat. During the first 3.8 ns of heating, the temperature of the sphere gradually increases (**Fig 3.3a**) from the ambient 300 K to the superheat temperature 580 K at which point a bubble is nucleated around it. Once this occurs, the sphere is surrounded by vapor and the heat transfer from its surface is greatly reduced. Thus, its temperature increases rapidly as it is still absorbing energy from the

incident light. The particle reaches a peak temperature of approximately 1080 K, which occurs at the end of the heat pulse (5 ns), while it is surrounded by vapor (**Fig. 3.3b**). Once the bubble has nucleated, which occurs just after 4 ns, it expands due to its high pressure relative to the surrounding fluid, which is initially at 1 atm. The bubble reaches its maximum volume 5.4 ns after the heating starts. At its largest extent, the bubble is characterized by a slightly elliptical shape and its maximum size is approximately 50 nm and 60 nm in the r and z directions, respectively. Subsequently, 7 ns after the onset of heating, the bubble collapses, bringing fluid back in contact with the particle, which cools it from its peak temperature of 1080 K to approximately 960 K (**Fig. 3.3c**). As the particle cools, the fluid temperature increases until it reaches the superheat temperature once again, at which point a secondary bubble is generated (**Fig. 3.3d**). The secondary bubble reaches its maximum size 8.2 ns after the initial onset of heating. At this point, the bubble is characterized by a spherical shape and its maximum size is approximately 50 nm in radius. Eventually, the second bubble collapses bringing fluid in contact with the sphere once again, and the sphere cools it towards the ambient temperature (**Fig. 3.3e**). It is important to note that the number of bubble cycles generated and the dynamics during each cycle can in principle be controlled by tuning the power and duration of the heat pulse (Furlani et al. 2012).

3.2 Nanorods

3.2.1 Synthesis

3.2.1.1 Let's now examine three bottom up methods of fabricating gold nanorods. The first method is the template method and was first introduced by Martin and co. in 1992. This technique is based on the electrochemical deposition of gold in the pores of nanoporous polycarbonate or alumina template membranes. The group showed that the gold/alumina composites can be optically transparent in the visible and also that by changing the aspect ratio of the prepared nanocylinders they were able to vary the color of the membrane (Foss Jr et al. 1992; Martin 1994, 1996). Following the initial work on nanocomposites, the method was later applied to the synthesis and dispersion of gold nanorods in water or even other organic solvents by the dissolution of the appropriate membrane followed by polymer stabilization (Cepak and Martin 1998; Van der Zande et al. 1997). In brief, this fabrication method can be described as follows: a) A small amount of Ag or Cu is sprayed onto the alumina template membrane to provide a conductive film for electrodeposition; b) Gold is then electrodeposited within the nanopores of alumina c) The alumina membrane and the copper or silver film are selectively dissolved in the presence of a polymeric stabilizer such as poly(vinylpyrrolidone) (PVP) d) The nanorods are then dispersed either in water or in organic solvents by means of sonication or agitation. The diameter of the gold nanoparticles synthesized with this method coincides with the pore diameter of the alumina membrane while their length can be controlled through the amount of gold deposited within the pores of the membrane (Pérez-Juste et al. 2005).

3.2.1.2 Another synthesis technique with considerable less complexity was first demonstrated by the Wang group. Their method, which is based on previous research on the electrochemical synthesis of transition metal clusters within reverse micelles in organic solvent systems, enables the production of gold nanorods with high yield. According to this technique, synthesis of gold nanorods can be made possible within a simple two-electrode-type electrochemical cell. More specifically, a gold metal plate is used as an Au source anode whilst the cathode is a platinum plate. Both electrodes are immersed in an electrolytic solution, containing a cationic surfactant, hexadecyltrimethylammonium bromide (C₁₆TAB), and a small amount of a much more

hydrophobic cationic surfactant,

tetradodecylammonium bromide (TC₁₂AB) acting as a rod-inducing co-surfactant.

The electrolytic cell containing the mixed solution is then placed inside an ultrasonic bath. Throughout the process, a controlled-current electrolysis is used with a typical current of 3 mA and a typical electrolysis time

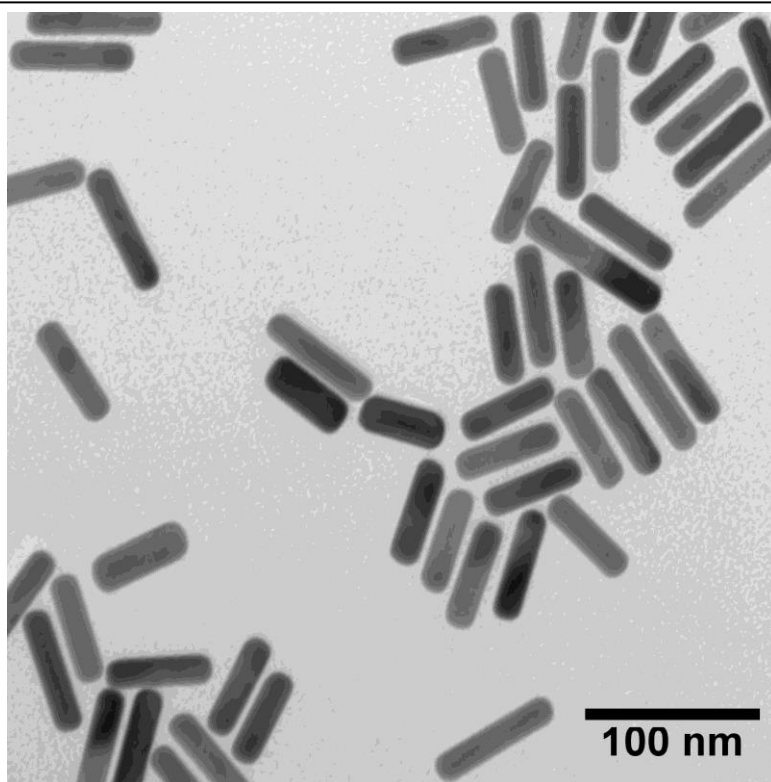


Figure 3.4. Scanning electron microscopy (SEM) image illustrating gold nanorods with an average length and diameter of 60 and 17 nm, respectively (source: www.nanocomposix.com).

of 30 min. Thus, the bulk gold metal anode is consumed, forming AuBr_4^- . These anions combine with the cationic surfactants and migrate to the cathode where reduction occurs. Sonication is required to shear the synthesized nanorods away from the cathode surface. An important factor controlling the aspect ratio of fabricated nanoparticles is the gradual introduction of a silver plate in the electrolytic solution behind the Pt electrode. The redox reaction between gold ions generated from the anode and silver metal leads to the formation of silver ions. It was determined that the concentration of silver ions and their release rate determined the length of the nanorods. The complete mechanism, as well as the role of the silver ions, still remains largely unexplained (Chang et al. 1999; Reetz and Helbig 1994; Yu et al. 1997).

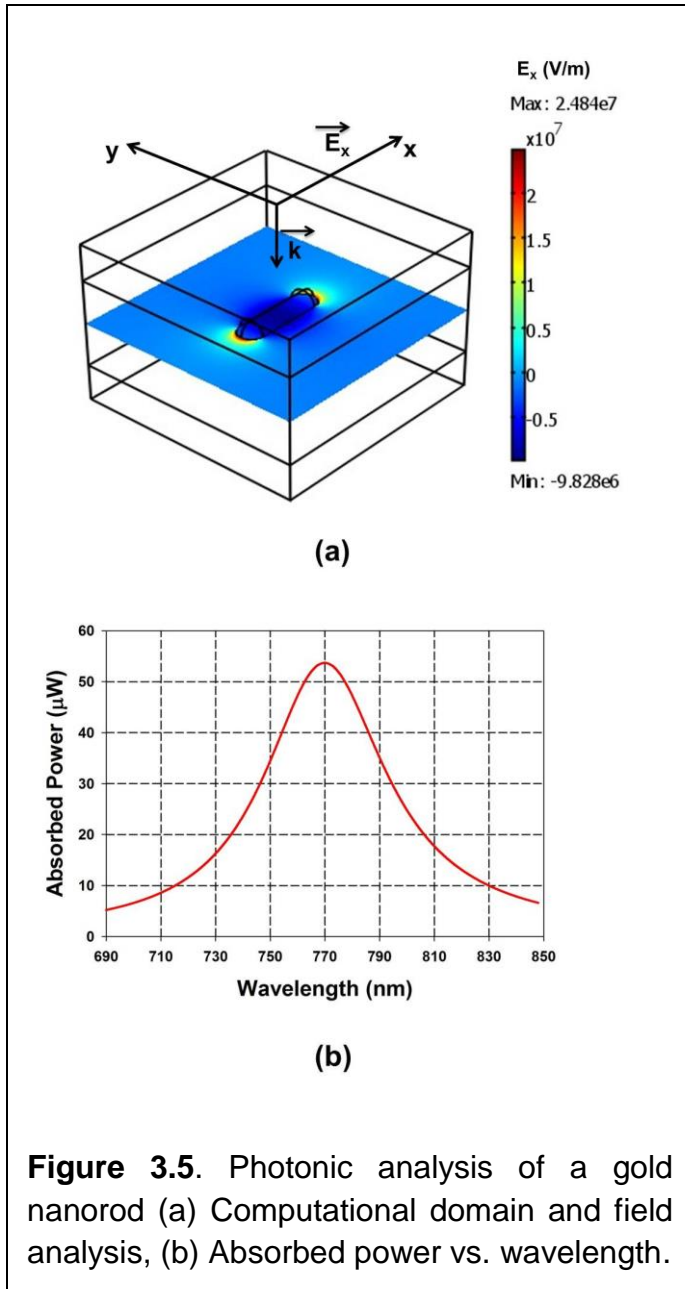
3.2.1.3 More recently, the seeding method, a technique for fabricating nanospheres (refer to 3.1.1.3), was also applied to the synthesis of gold nanorods. Although, the basic steps involved in this fabrication method, described in the previous subsection, remain the same, gold nanorods can be synthesized by carefully controlling the growth conditions, and in particular by using ascorbic acid as a weak reducing agent, that cannot reduce the gold salt in the presence of the micelles if the seed is not present. By controlling the growth conditions in aqueous surfactant media it is possible to synthesize gold nanorods with tunable aspect ratio. It was found that addition of AgNO_3 influences not only the yield and aspect ratio control of the gold nanorods but also the mechanism for gold nanorod formation and correspondingly its crystal structure. Nevertheless, synthesis of gold nanorods is possible even without its addition. A more thorough

description of the details of nanorod synthesis and applications can be found in a very well written review by J. Pérez-Juste et al. (Pérez-Juste et al. 2005).

3.2.1.4 Having provided the basic principles of nanorod fabrication, we shift our attention to the use of gold nanorods for bubble nucleation. It is important to note that these nanoparticles have plasmonic properties that are different than their spherical counterparts. Most notably, they have two distinct plasmon resonant frequencies, one higher and one lower, corresponding to transverse and longitudinal polarization modes, respectively. The higher frequency (shorter wavelength) occurs when the field is polarized transverse to the rod (i.e. perpendicular to the major axis) and is similar to that of a spherical particle. The lower frequency (longer wavelength) depends on the aspect ratio of the nanorod and can be tuned through synthesis for specific applications. The ability to tune the resonance in this fashion has spawned a growing interest in the use of gold nanorods, especially for bioapplications that require plasmon resonance tuned to NIR wavelengths to achieve deeper and more effective penetration of light into a target tissue. Gold nanorods have additional interesting plasmonic features, notably, a narrower plasmon bandwidth (Sonnichsen et al. 2002) and greater field enhancement than spherical particles at comparable resonance frequencies and volumes.

3.2.2 Photonic Simulations

3.2.2.1 The gold nanorod was modelled as a cylinder with hemispherical caps. For this analysis, we chose the length and diameter of the nanorod to be 60 nm and 17 nm,



respectively. The computational domain for the photonic analysis spans 110 nm in the direction of propagation (z -axis), and 150 nm in both the x and y directions as shown in **Fig. 3.5a**. The nanorod is centered at the origin with its length aligned with the x -axis. As before, there are PMLs at the top and bottom of the computational domain, which are 25 nm in height. This leaves 60 nm of physical domain along the z -axis. PEC boundary conditions are applied at boundaries perpendicular to the E field at $x = \pm 75$ nm and PMC boundary conditions are applied at boundaries perpendicular to the H field at $y = \pm 75$ nm. These conditions

mimic a 2D array of identical nanorods with a center-to-center lattice spacing of 150 nm in both the x and y directions. The nanorod is illuminated with a downward directed uniform TEM plane wave with \mathbf{E} aligned along the length of the nanorod, i.e. parallel to the x -axis. As in the previous analysis, the incident field is generated by a time-harmonic surface current positioned in the x - y plane immediately below the upper PML. Cubic

vector finite elements were used and there were a total of 41,932 tetrahedral elements in the computational domain. The time-averaged power absorbed by the nanorod was computed for wavelengths that spanned 600 nm to 900 nm in 2 nm increments. The plasmon resonance wavelength was found to be 770 nm and the corresponding power absorbed is 53.7 μW (with $I_{inc} = 7 \text{ mW}/\mu\text{m}^2$) as shown in **Fig. 3.5b**.

3.2.3 Thermofluidic Simulations

3.2.3.1 A CFD analysis was performed to determine a power level and pulse duration that would produce bubble nucleation and sustained dynamics without melting the nanorod. An axisymmetric CFD model was used for the analysis. The computational domain spanned 150 nm in both the r and z directions. A uniform mesh of 0.5 nm cells in both directions was used. Symmetry boundary conditions were imposed along both the r and z axes. The former accounted for the lower half of the nanorod while the latter accounted for its axial symmetry. The same initial and boundary conditions were used as in the case of the nanosphere. However, it should be noted that unlike a sphere, a nanorod is characterized by different heat transfer coefficients along the surface of its cylindrical portion as compared to its spherical tips. Thus, bubble nucleation and growth can evolve differently over these surfaces.

3.2.3.2 As in the case of the sphere, a preliminary CFD analysis (without phase change) was performed to determine a range of power levels and pulse durations that increase the temperature of the nanorod from ambient to the supercritical temperature.

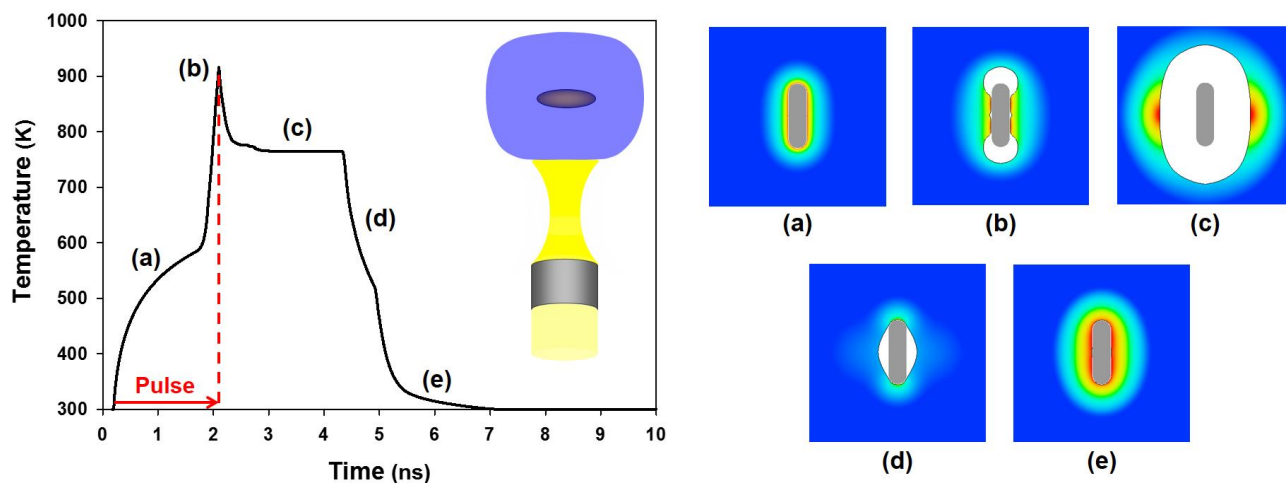


Figure 3.6. Photothermal heat cycle of a nanorod ($L = 60 \text{ nm}$, $R = 8.5 \text{ nm}$) (cross-sectional view): plot of nanorod temperature vs. time, pulse duration indicated by red arrow and dashed line and inset plots showing various phases of the thermal cycle; (a) initial heating, (b) nanobubble formation, (c) nanobubble (maximum size), (d) nanobubble collapse, (e) cooling.

Based on this analysis, we identified viable power levels and pulse durations limited to a range of 1.5 to 3 ns. We then used this data in a parametric CFD analysis that accounted for bubble nucleation, only with slightly extended pulse durations so as to ensure a sustained bubble without damaging the particle. It was found that an adequate power for nucleation without melting the nanorod was $76.8 \text{ } \mu\text{W}$, with a pulse duration of 1.9 ns. Given these values and the results of the photonic analysis (**Fig. 3.5b**), we determined that a laser operating at $\lambda = 770 \text{ nm}$ with an irradiance of $I_{inc} = 10 \text{ mW}/\mu\text{m}^2$ is sufficient to generate and sustain a bubble without melting the nanorod. The photothermal process at this power and pulse duration is shown in **Fig. 3.6**. This figure shows the temperature of the nanorod during and after the heat pulse along with corresponding images that show the generation and collapse of the nanobubble.

3.2.3.3 Initially, the nanorod is at ambient temperature of 300 K. After 0.2 ns the nanorod is illuminated and its temperature starts to increase. During the first 1.7 ns of heating, the temperature of the nanorod gradually increases to the superheat temperature (**Fig. 3.6a**), at which point a bubble is nucleated around its tips. Once this occurs the particle is partly surrounded by vapor and heat transfer from its surface is greatly reduced. Its temperature increases rapidly at this point as it is still absorbing energy from the incident light. The nanorod reaches a maximum instantaneous temperature of 915 K, which occurs at the end of the heat pulse (1.9 ns in duration) when it is still surrounded, in part, by liquid (**Fig. 3.6b**). The remaining liquid completely evaporates by approximately 2.7 ns after the onset of heating, and in doing so, the nanorod cools from its peak temperature to approximately 765 K.

3.2.3.4 As soon as the bubble has nucleated, it expands due to its high pressure relative to the surrounding fluid. It reaches its maximum size 3 ns after the onset of heating (**Fig. 3.6c**) at which point it has an elliptical shape and it has dimensions of approximately 45 nm and 65 nm in the r and z directions, respectively. Eventually, at 4.4 ns the nanobubble collapses, bringing fluid back in contact with the tips of the nanorod (**Fig. 3.6d**) and starts cooling it. The nanorod is then further cooled to ambient temperature when the rest of the fluid comes in contact with it, 5.2 ns after the onset of heating (**Fig. 3.6e**) (Furlani et al. 2012).

3.3 Nanorings and nanotori

3.3.1 Synthesis

3.3.1.1 The next nanostructures we consider are nanorings and nanotori (**Fig. 3.7**). These two geometries are very similar and have comparable optical responses, hence they are studied as a group. Various methods have been demonstrated for producing such nanoparticles (Yan and Goedel 2005; Zinchenko et al. 2005). More specifically, gold nanorings can be produced with a bottom up approach through a template method. Adding chloroauric acid to a solution of silver nanodisks can cause colloidal nanoring formation because the standard reduction potential of the $\text{AuCl}_4^-/\text{Au}$ redox pair is higher than that

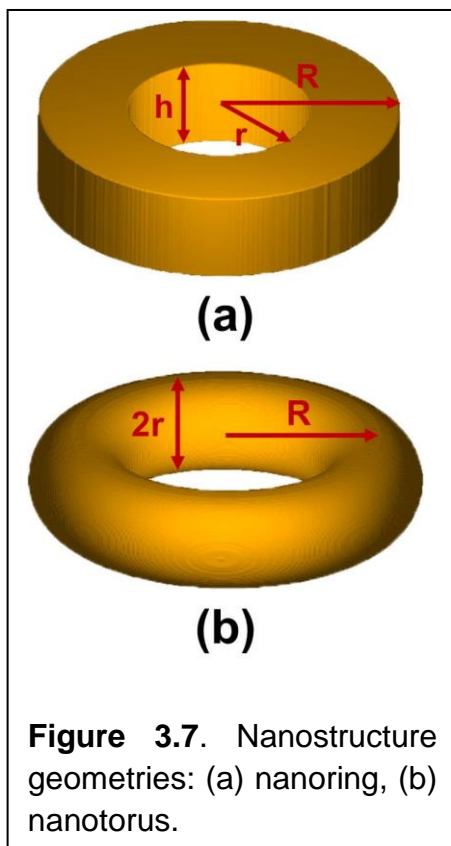


Figure 3.7. Nanostructure geometries: (a) nanoring, (b) nanotorus.

of the Ag^+/Ag redox pair, thus, silver nanoparticles can be oxidized to silver ions immediately. The AgCl precipitate can, then, be removed by an aqueous solution of ammonia. Different molar ratios between gold and silver can lead to different nanoring morphologies (Jiang et al. 2004; Y. Sun and Xia 2003b; Z. Wang 2000).

3.3.1.2 Nanotori, have been recently fabricated on substrates using top-down lithographic techniques and then released into a colloidal dispersion. However, to the best of our knowledge, currently no bottom up fabrication methods exist. Nevertheless, we

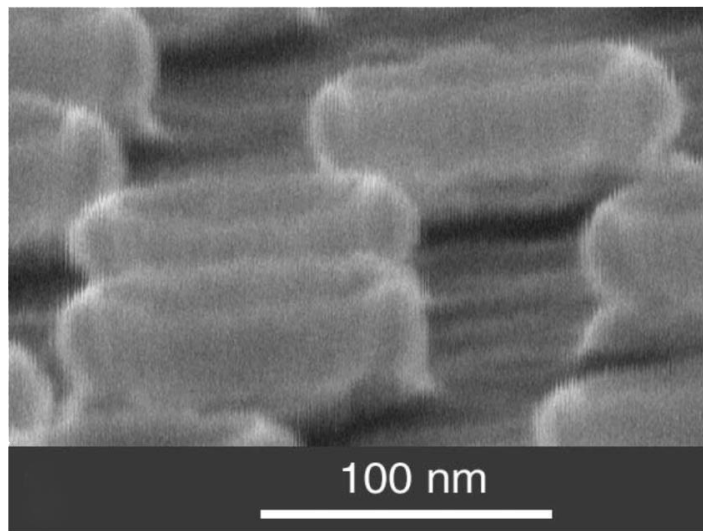


Figure 3.8. SEM image (tilted by 80°) of gold nanotori fabricated with colloidal lithography (Aizpurua et al. 2003)

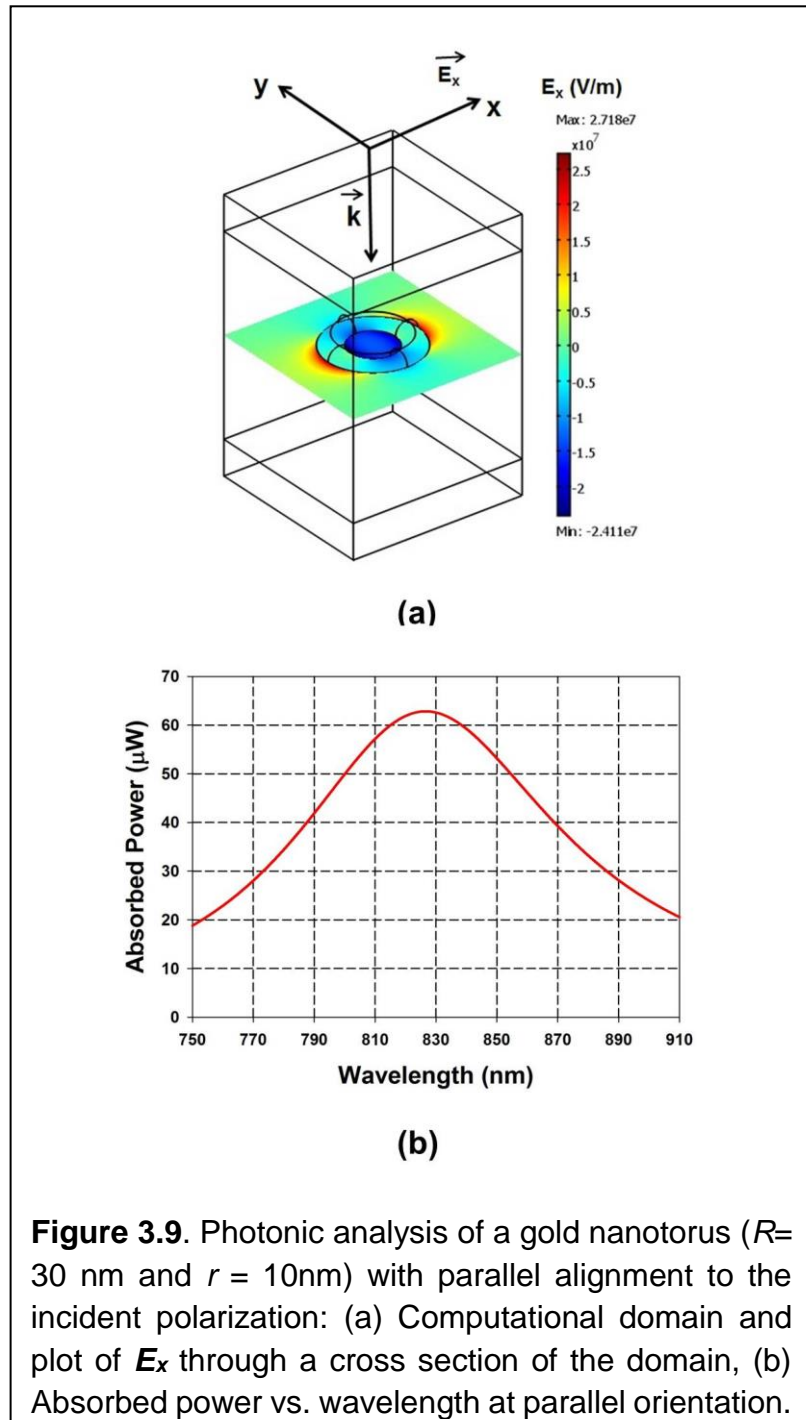
choose to study this nanoparticle geometry because it is commonly confused with nanorings due to its symmetrical round structure, as seen in **Fig. 3.8**. It is believed that rapid advances in nanoparticle synthesis will most likely lead to bottom-up methods for producing these particles in the near future. In addition, these structures can

be tuned to have a high absorption cross-section in the NIR. For instance, for incident light polarized in the plane of the torus, the optical spectrum is characterized by a long wavelength resonance, and a short wavelength resonance that corresponds to excitation of higher order modes. We are most interested in the long wavelength resonance as it can be tuned by varying the major (R) and minor (r) radii of the torus, during synthesis (Aizpurua et al. 2003; Dutta et al. 2008; Lee et al. 2010). Though nanorods also possess this feature, their longer (e.g. NIR) resonant wavelength will only be effective when the field is polarized along the major axis, which can be difficult to achieve in practice. Due to their unique symmetrical shape, the absorption of such nanostructures remains relatively high for a broad range of orientations since resonance can be achieved with the field polarization at any angle as long as it is in the plane of the torus. Therefore, nanorings and nanotori are better-suited for colloidal heating applications than nanorods especially for bioapplications that require NIR illumination for maximum tissue penetration. The

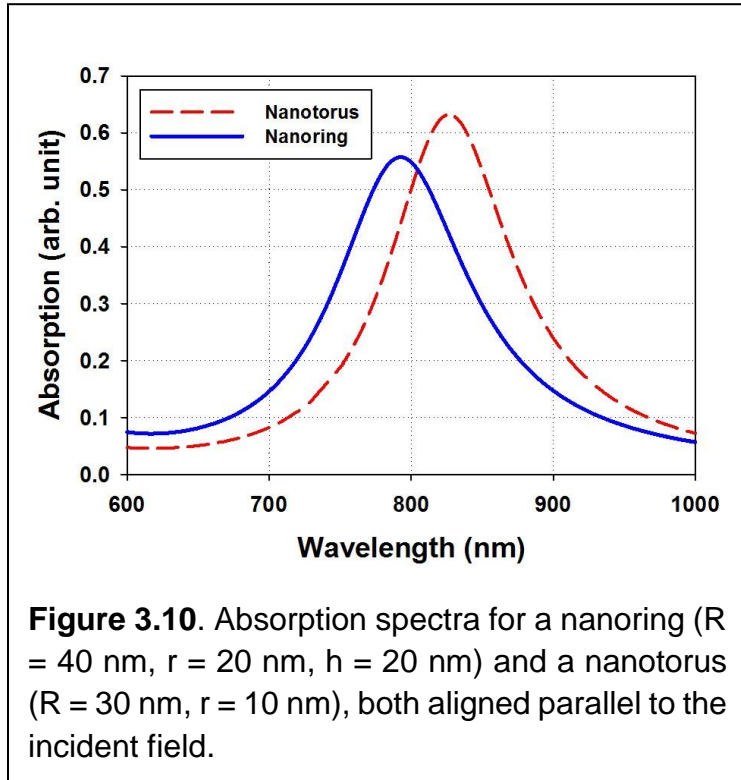
results of the random orientation colloidal modeling will be discussed in more detail in chapter 4.

3.3.2 Photonic Simulations

3.3.2.1 For our initial modeling effort we consider 3 different aspect ratios for each geometry, i.e. r/R in the case of the nanotorus and $(R-r)/R$ in the case of the nanoring. However, in order to more concisely summarize our modeling effort, in the following sections, we will consider a specific nanotorus with major and minor radii of $R= 30$ nm and $r = 10$ nm, respectively. A similar analysis was performed for each geometry and the results are summarized in **Table 1**.



3.3.2.2 The computational domain for the torus spans 230 nm in the direction of propagation (**z**-axis), and 150 nm in both the **x** and **y** directions (**Fig. 3.9a**). The torus is centered at the origin and as above, there are PMLs at the top and bottom of the computational domain, which are 30 nm in height. This leaves 170 nm of physical domain along the



z-axis. Once again, PEC boundary conditions are applied at boundaries perpendicular to the **E** field at $\mathbf{x} = \pm 75$ nm, and PMC boundary conditions are applied at boundaries perpendicular to the **H** field at $\mathbf{y} = \pm 75$ nm. These conditions mimic a 2D array of identical nanotori with a center-to-center lattice spacing of 150 nm in both the **x** and **y** directions. The torus is illuminated with a downward directed uniform TEM plane wave with **E** parallel to the **x**-axis (**Fig. 3.9a**). The incident field is generated by a time-harmonic surface current positioned in the **x-y** plane 85 nm above the center of the torus, i.e. directly below the upper PML. We performed a parametric analysis of the power absorbed by the torus as a function of wavelength for $\lambda = 750$ -950 nm in 2 nm increments. As in the previous cases, cubic vector finite elements were used, in this case there were 28,668 tetrahedral elements in the computational domain. Plasmon resonance was found to occur at 828

nm and the corresponding power absorbed is 62.8 μW (with $I_{inc} = 7 \text{ mW}/\mu\text{m}^2$) as shown in **Fig. 3.9b**.

3.3.2.3 Nanorings are closely related to nanotori in terms of their plasmonic behavior. An example of this can be seen in **Fig. 3.10**, which shows the absorption spectra for the two geometries of comparable sizes when they are aligned parallel to the incident field. It is instructive to note that the resonant wavelength of the nanotorus is redshifted with respect to the nanoring. This is due primarily to the fact that the torus has a smaller aspect ratio ($r/R = 1/3$) than the ring ($(R-r)/R = 1/2$).

3.3.3 Thermofluidic Simulations

3.3.3.1 Similarly, for our fluidic analysis we considered 3 cases for each geometry. However, we present here the thermofluidic nanobubble heat cycle for the case of nanotorus with major and minor radii of $R = 30 \text{ nm}$ and $r = 10 \text{ nm}$, respectively. The analysis steps described here apply to all cases of each geometry and will be summarized in **Table 1**. For the aforementioned case of nanotorus, we performed a CFD analysis to determine the power and pulse duration required to achieve bubble nucleation without melting the nanoparticle. An axisymmetric model was used with a computational domain that spanned 200 nm in both the r and z directions. A uniform mesh of 1 nm cells in both dimensions was used. Symmetry boundary conditions were imposed along both the r - and z -axes. The former accounted for the lower half of the torus while the latter accounted

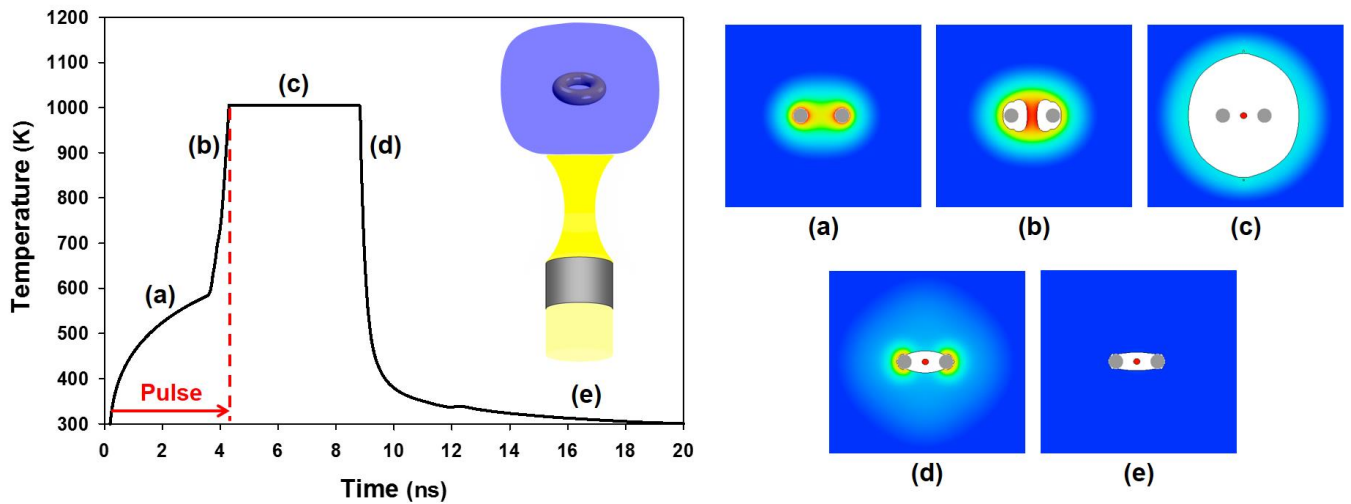


Figure 3.11. Photothermal heat cycle of a gold nanotorus ($R= 30$ nm and $r = 10$ nm) (cross-sectional view): plot of nanorod temperature vs. time, pulse duration indicated by red arrow and dashed line and inset plots showing various phases of the thermal cycle; (a) initial heating, (b) nanobubble formation, (c) nanobubble (maximum size), (d) nanobubble collapse, (e) cooling.

for its axial symmetry. The initial and boundary conditions are the same as for the previous cases of nanospheres and nanorods.

3.3.3.2 As in the other cases, a preliminary thermal analysis (without phase change) was performed to determine power levels and pulse durations that increase the temperature of the torus from ambient to the supercritical temperature. We calculated the temperature of the torus during heating for a range of power levels and pulse durations. The latter was chosen to be from 2 to 5 ns. Once this was complete, the results were used in a second parametric CFD analysis that included bubble nucleation to determine viable power levels and pulse durations that are sufficient to nucleate a sustained bubble without destroying the torus or ring. It was found that an adequate power for nucleation was $172.8 \mu\text{W}$, with a pulse duration of 4.1 ns. Given these values and the results of the

photonic analysis (**Fig. 3.9b**) we determined that a laser operating at the plasmon resonant wavelength of $\lambda = 828$ nm with an irradiance of $I_{inc} = 19.27$ mW/ μm^2 is sufficient to generate and sustain a bubble without melting the torus. The fluidic analysis at this power and pulse duration is shown in **Fig. 3.11**. This plot shows the temperature of the torus throughout the photothermal process along with corresponding images of the bubble dynamics.

3.3.3.3 Initially the torus is at ambient temperature. After 0.2 ns it is illuminated and its temperature begins to rise. During the first 3.4 ns of heating, its temperature gradually increases (**Fig. 3.11a**) to the superheat temperature, at which point a bubble is nucleated around it. Once this occurs the torus is surrounded by vapor and its temperature increases rapidly as it is still absorbing energy. It reaches a peak temperature of approximately 1000K, which occurs at the end of the heat pulse (4.1 ns), at which point it is completely surrounded by vapor (**Fig. 3.11b**). As soon as the bubble has nucleated, it expands and reaches its maximum size at 5.4 ns after the onset of heating. At this time the bubble has a spherical shape, approximately 80 nm in radius.

3.3.3.4 An interesting feature of this process is the residue of an isolated drop of heated fluid that forms in the middle of the torus during the bubble expansion as seen in **Fig. 3.11c**. Eventually, 8.7 ns after the onset of heating, the nanobubble collapses, bringing fluid back in contact with the torus (**Fig. 3.11d**). Consequently, it slowly cools to the ambient temperature as more of the fluid comes in contact with it (**Fig. 3.11e**). It is instructive to note that the capillary force that acts to collapse the bubble is relatively weak

because of the relatively large radius of curvature that defines the fluid-vapor interface as it gets closer to the torus. Thus, the nanobubble requires a substantial amount of time to completely collapse, compared to other geometries. This effect is not present in the case of nanorings

3.4 Nanocages and Nanoframes

3.4.1 Synthesis

3.4.1.1 Hollow cubical nanostructures have gained more attention in recent years owing to their high absorption cross-section that qualifies them as the optimum choice for a variety of bioapplications (Jingyi Chen et al. 2007; Leon R Hirsch et al. 2006; Loo et al. 2004). In this part of

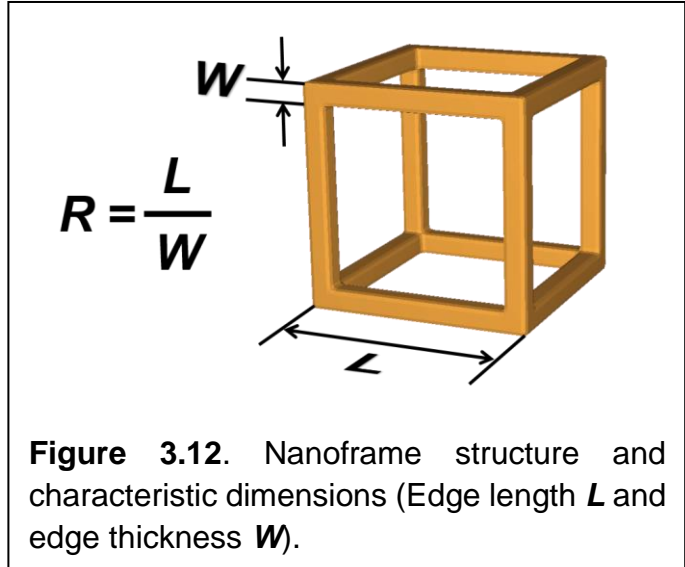


Figure 3.12. Nanoframe structure and characteristic dimensions (Edge length L and edge thickness W).

our work we will specifically focus on cubical nanocages and nanoframes. Nanocages are hollow cubical structures with porous walls while nanoframes are hollow cubical structures that are defined by a metallic frame. An idealized nanoframe can be thought of as consisting of twelve rectangular nanowires with length L and width W as shown in **Fig. 3.12**. Both nanocages and nanoframes can be fabricated through a template method. As far as nanocages are concerned, some of the earliest work in the field was performed by Y. Sun and Y. Xia in 2003. They reported a simplified method of fabricating porous metal nanostructures through the galvanic replacement reaction between silver (Ag) nanoparticles in an aqueous solution of chloroauric acid (HAuCl_4). By carefully choosing the concentration of chloroauric acid in the solution, the authors managed to fabricate porous Au/Ag nanocages through a de-alloying process during which silver atoms were replaced with gold. The resulting nanoparticles were found to have a plasmon resonance

wavelength in the NIR region (800 – 1030 nm) (Y. G. Sun and Xia 2003a). Following this work, J.Chen et al. fabricated and characterized gold nanocages on the scale of 40nm. This group determined that despite their smaller size compared to other nanoparticle geometries (e.g. gold nanoshells), nanocages not only maintain strong optical resonance peaks in the NIR but also, based on optical coherence tomography (OCT) measurements, present a very large absorption cross-section compared to other nanoparticles or organic dyes. In addition, it was shown that bioconjugated gold nanocages coated IgG antibodies could successfully bind to SK-BR 3 breast cancer cells bound with anti-HER2 antibodies. Hence, gold nanocages also showed potential as thermal therapeutic agents for cancer treatment (J. Chen et al. 2005). S.E. Skrabalak et al. managed to prepare porous hollow gold nanostructures in the order of ~15nm with 2 to 5nm voids using silver multiply twinned particles (MTPs). The LSPR wavelength for such nanoparticles could reach a maximum of 740nm despite their smaller size. Such nanoparticles could prove advantageous for biomedical applications through enhanced delivery rates and diffusion. In a related result, coating 45nm nanocages with calcein AM (fluorescent green in living cells) and EthD-1 (fluorescent red when penetrating compromised cell walls) this group could determine the effectiveness of using nanocages for photothermal treatment through fluorescence microscopy (Skrabalak et al. 2007).

3.4.1.2 In the field of nanoframe fabrication a pioneering study was carried out by Y. Xia and his group who introduced a simplified method of fabricating nanoframes through the galvanic replacement reaction between silver (Ag) nanocubes and chloroauric acid (HAuCl₄). This method is very similar to the one employed for fabricating nanocages but the geometrical characteristics of the ensuing nanostructures can be

altered by carefully selecting the concentration of chloroauric acid in the solution. The resulting nanoparticles were found to have absorption peaks ranging from 400nm to 900nm (Au et al. 2008; Wan et al. 2013). The optical properties of

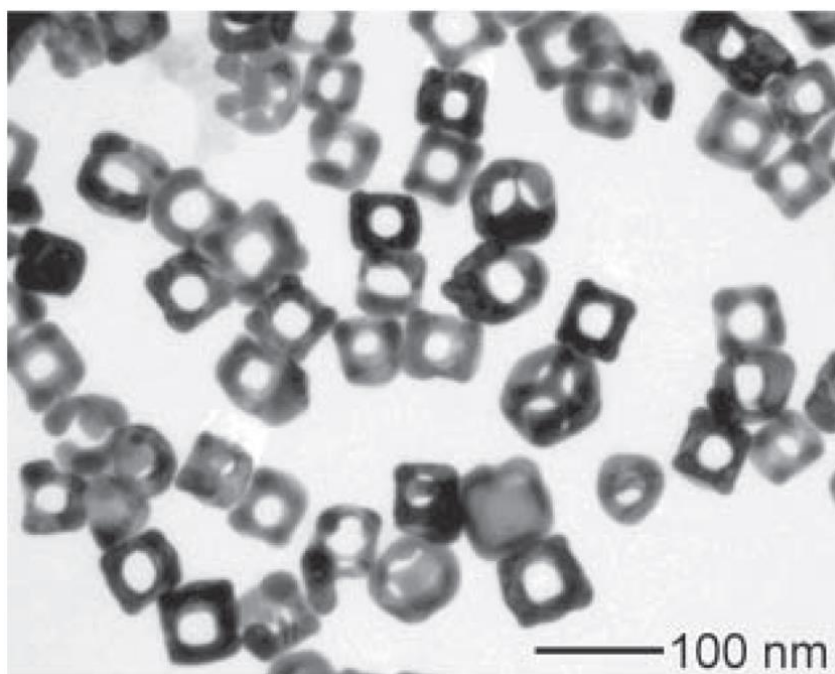


Figure 3.13. Transmission electron microscopy (TEM) image of gold nanoframes with an average edge length $L = 50$ nm and thickness $W = 10$ nm (Au et al. 2008)

nanoframes were further investigated by M.A. Mahmoud and M.A. El-Sayed. In a combination of theoretical and experimental studies, they were able to determine that nanoframes exhibit strong field enhancement at their surface and throughout their hollow interior. Moreover the authors demonstrated that gold nanoframes have significantly higher sensitivity factors (an indication of the strength of a nanoparticle's plasmonic surface field), compared to other similar size solid nanoparticles. As such, gold nanoframes represent promising candidates for nanosensors in the NIR (M. A. Mahmoud and El-Sayed 2010; M. Mahmoud et al. 2010). Despite the plethora of research on their optical characteristics, compared to other metallic nanoparticles, to the best of our knowledge, no theoretical studies have been reported to quantify the photothermal and

thermofluidic behavior of colloidal Au nanoframes under pulsed-laser illumination (Baffou and Quidant 2013).

3.4.1.3 As it can be deduced from this brief literature review, nanocages and nanoframes are very similar in their fabrication and optical characteristics. Since a nanoframe with thicker frame elements can be considered a nanocage while a nanocage with highly porous walls can be considered a nanoframe, in order to make our analysis more concise, from now on the term nanoframe will be used to describe this type of nanoparticles in the following subsections; where, for the first time, their photothermal response and nanobubble behavior will be numerically quantified.

3.4.2 Photonic Simulations

3.4.2.1 In this section we explore the optical properties of nanoframes with different dimensions and orientations. The computational domain for this analysis is shown in **Fig. 3.14a**. A single Au nanoframe is centered at the origin of the domain. The geometry of the nanoframe is defined by its length L that defines the size of the cube (i.e. the length of the rectangular nanowire frame element), and the width W that defines the cross-sectional area of the nanowire as shown in **Fig. 3.12**. The aspect ratio, $R=L/W$ is also used in parts of our analysis. The particle is illuminated with a uniform downward-directed plane wave with the E field parallel to the x -axis. PMLs are applied at the top and bottom of the domain to reduce backscatter from these boundaries. PEC conditions are applied at the boundaries perpendicular to \mathbf{E} , and PMC conditions are applied at the boundaries

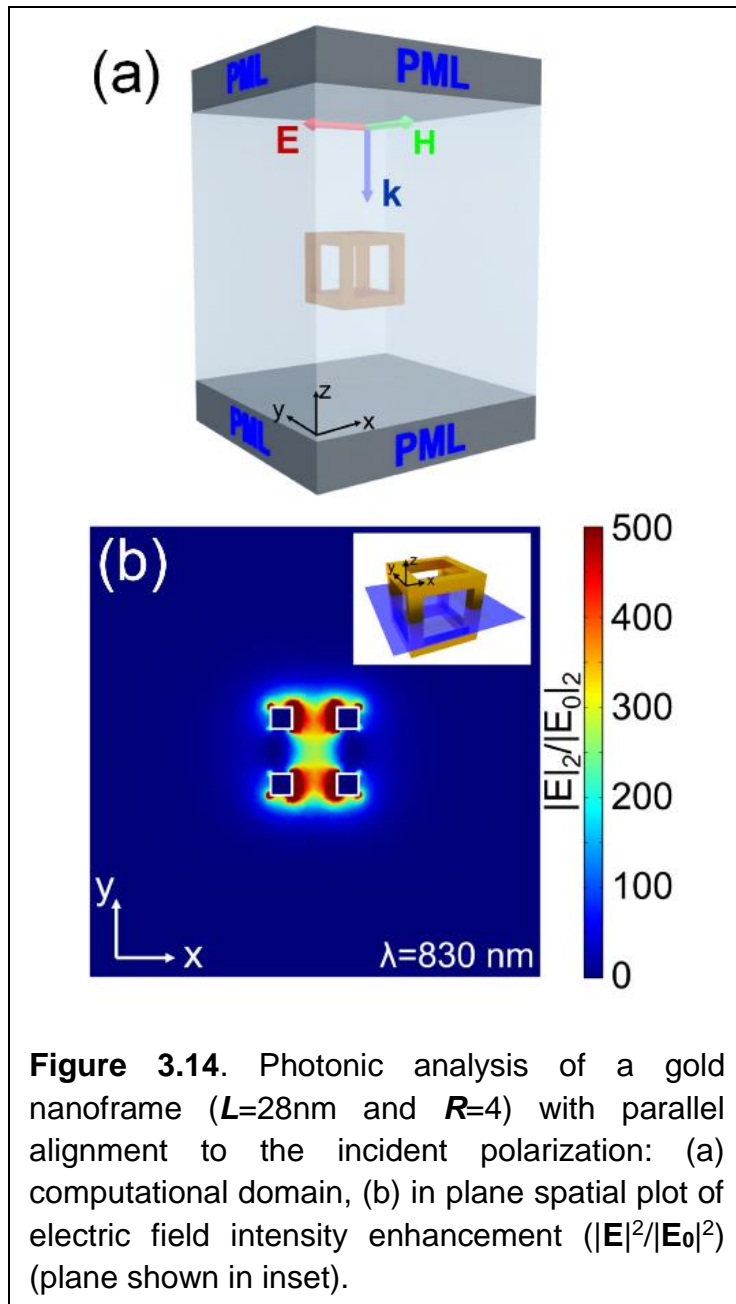
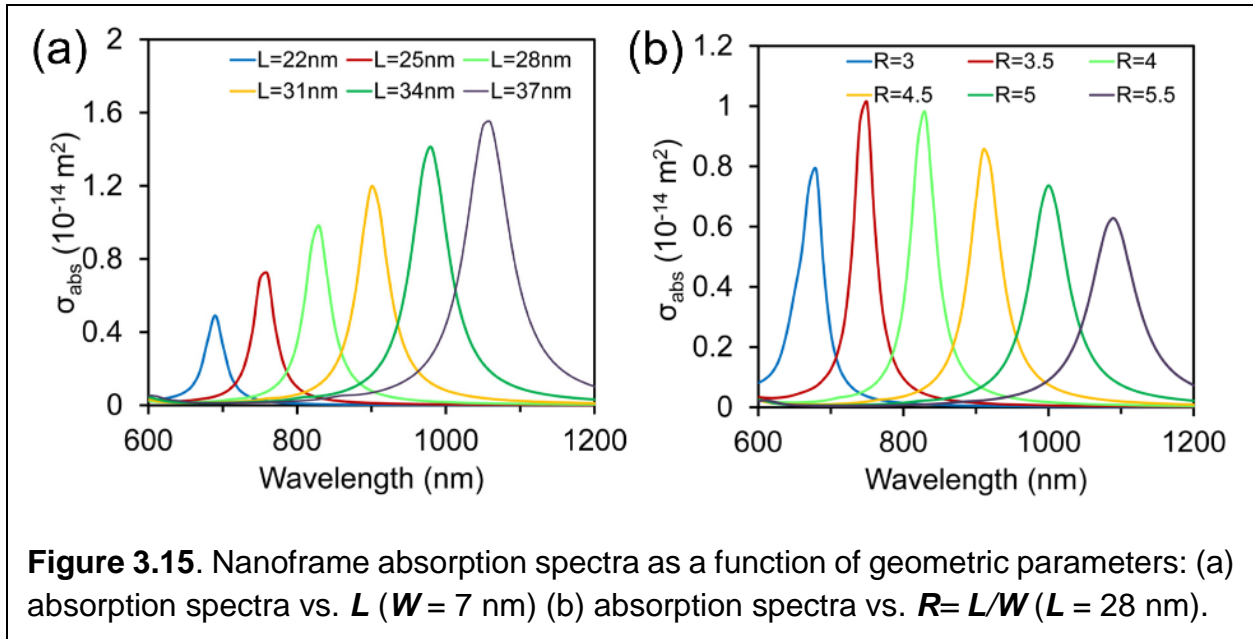


Figure 3.14. Photonic analysis of a gold nanoframe ($L=28\text{nm}$ and $R=4$) with parallel alignment to the incident polarization: (a) computational domain, (b) in plane spatial plot of electric field intensity enhancement ($|E|^2/|E_0|^2$) (plane shown in inset).

perpendicular to \mathbf{H} . These symmetry boundary conditions mimic the response of a 2D array of identical nanoframe structures with center-to-center x and y lattice spacing equal to the width of the computational domain in the x and y directions, respectively. The lattice spacing is chosen to be large enough so that the resulting predictions will reflect the response of a single isolated particle, i.e. with negligible coupling with neighboring particles. The fluid surrounding the nanoparticle is assumed to be non-absorbing water with an index of refraction of $n_f = 1.3$. The

incident field is generated by a time-harmonic surface current positioned in the x - y plane directly below the upper PML. We compute the (wavelength dependent) power absorbed by the particle Q_{abs} (W), which is converted to heat. Thus, this analysis predicts photothermal energy conversion within the particle.

3.4.2.2 In **Fig. 3.14b** we plot the spatial profile of electric field intensity enhancement ($|E|^2/|E_0|^2$) in the **x-y** plane, shown in the inset. The size of the nanoframe is $L=28$ nm with $R=4$ and the localized surface plasmon resonance (LSPR) occurs at $\lambda = 830$ nm. An interesting discovery of this analysis is that the mode profile demonstrates a high degree of field localization and enhancement due to the coupled surface plasmons of the neighboring nanowire frame elements. We believe that this property can be leveraged for theranostic biomedical applications because the surface of gold nanoframes can be functionalized to achieve cancer cell specificity. More specifically, by manipulating thiolate-Au monolayer chemistry, excellent compatibility between gold surfaces and various molecules and ligands can be achieved (J. Chen et al. 2005; Xia et al. 1999). Through the functionalization process, fluorescent labels can be attached to the gold surface to enable spatial tracking and imaging. The LSPR of Au nanoparticles can then be used to enhance fluorescent signal intensity. Such fluorescence increase is directly related to the localized field enhancement at LSPR (Khatua et al. 2014). **Figure 3.14b** shows that strong E field enhancement (~ 500 fold) occurs around the nanowires. This could dramatically increase the signal from surface-bound fluorescent molecules. Highly localized regions that exhibit even higher enhancement (~ 3000) can also be observed. If the frame elements of a nanoframe are sufficiently close to one another, their LSPR modes are coupled, which can produce a significant field enhancement throughout the interior of the nanoframe. We have predicted enhancement factors of ~ 300 for this region. This could prove to be especially useful for biomedical applications wherein photoactivated theranostic agents are transported to target tissue in the porous



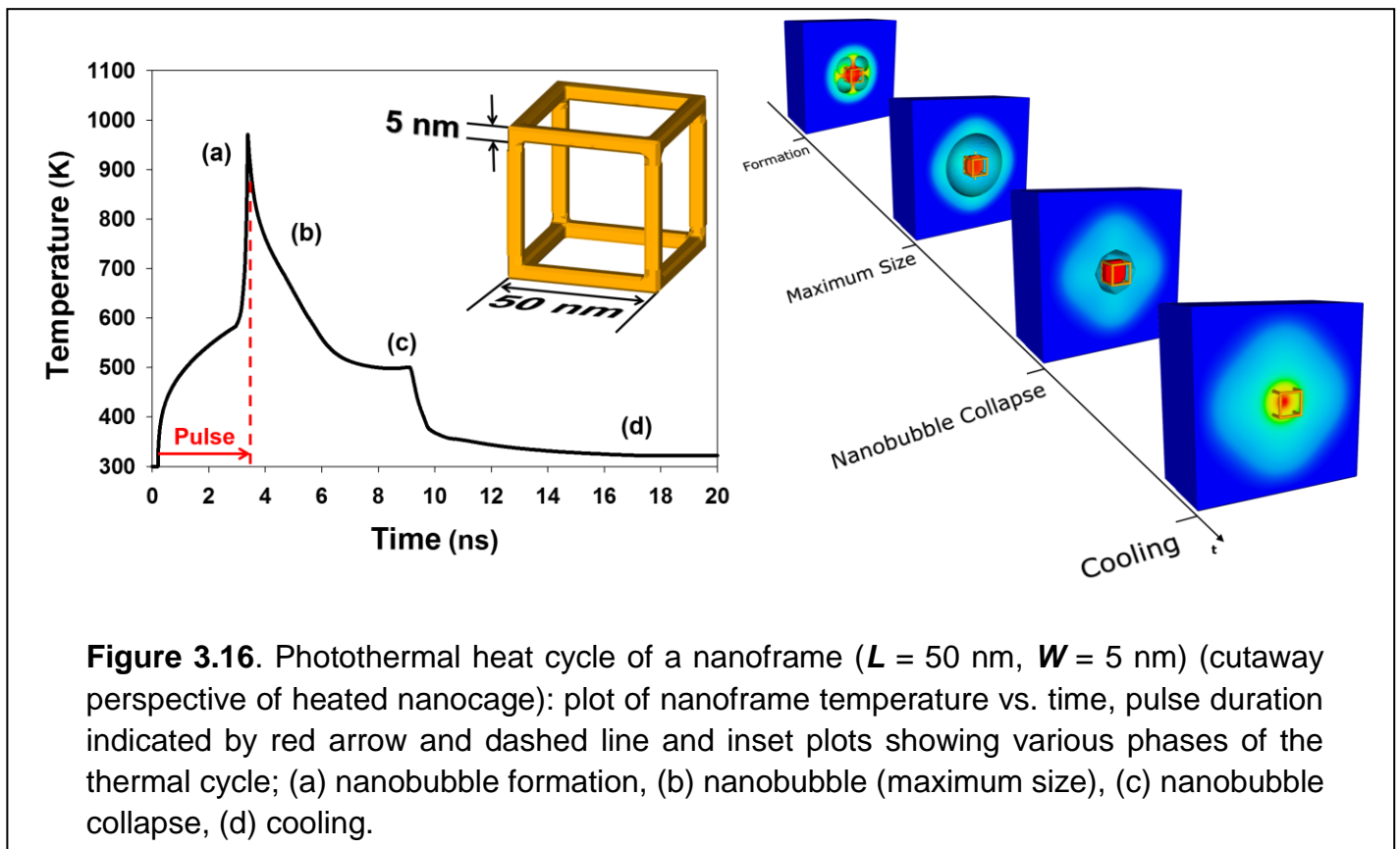
interior of a nanoframe. These include therapeutic drugs and fluorescent probes (Mackey et al. 2013; Xiong et al. 2014) that can enable high-resolution in vivo imaging and tracking.

3.4.2.3 Next we investigate the absorption cross-section spectra σ_{abs} (m^2) (absorbed power Q_{abs} (W) divided by the incident irradiance I_{inc} (W/m^2)) and especially the LSPR peak wavelength of a nanoframe as a function of its geometric parameters, i.e. L and W . As a first step in the analysis, we compute σ_{abs} as a function of L in the range of 22-37 nm with W fixed at 7 nm. As shown in **Fig. 3.15a**, as L increases, the LSPR absorption peak red-shifts from 690 nm to 1060 nm, demonstrating a strong L -dependent LSPR sensitivity, similar to that observed in nanorods (Alali et al. 2013). Our analysis also indicates that the optical absorption of a nanoframe at LSPR increases with the amount of gold it contains (**Fig. 3.15a**). Similarly, we then study the optical response of the nanoframe as a function of the aspect ratio $R = L/W$ where R ranges from 3 to 5.5 and $L = 28$ nm is kept constant. The absorption cross section σ_{abs} is calculated as a function of wavelength and plotted in **Fig. 3.15b**. Note that the LSPR peak wavelength red-shifts

from 680 nm to 1090 nm as R increases. We found that the absorption cross-section of the nanoframe monotonically decreases with W (Karampelas et al. 2016).

3.4.3 Thermofluidic Simulations

3.4.3.1 Contrary to all previous geometries studied, nanoframes do not exhibit any kind of axial symmetry. Thus a highly complex, full 3D analysis is required to describe their thermofluidic response to incident illumination. This 3D CFD analysis was performed to determine the incident optical irradiance and pulse duration needed to superheat the nanoframe and to nucleate an explosive homogeneous nanobubble without damaging the nanoparticle, i.e. without melting or vaporizing the metal. Owing to its symmetrical



nature, it was only necessary to model a 3D octant of the nanoframe. The CFD computational domain spanned a length scale that ranged from 2.8 to 8 times the edge length L of the nanoframe depending on the size of the bubble that was generated. A computational mesh of cubical cells was used for the analysis. The cell size was fixed at 1 cubic nanometer for $x, y, z \leq 150\text{nm}$, gradually increasing in size to a maximum of 2 cubic nanometers for the rest of the domain. The cell size was chosen to optimize the accuracy of the simulation (better surface tracking during the onset of bubble nucleation) while maintaining computational efficiency (lower total runtime). Symmetry boundary conditions were imposed along the x -, y - and z -axes in order to account for the remaining octants of the nanoframe. A stagnation pressure condition was imposed at the outer boundaries along with a thermal Dirichlet condition ($T=300\text{K}$) to account for the ambient temperature of the surrounding fluid. The pressure and temperature throughout the computational domain were initialized to 1Atm and 300K, respectively. These initial values and boundary conditions were used for all cases studied in our thermofluidic analysis. We chose water as the working fluid but the analysis can be applied to any Newtonian fluid.

3.4.3.2 Various gold nanoframe structures were studied, $L = 50\text{ nm} - W = 5\text{ nm}$, $L = 50\text{ nm} - W = 10\text{ nm}$ and $L = 70\text{ nm} - W = 5\text{ nm}$. It should be noted that the nanoframe dimensions selected for this analysis were chosen to illustrate representative photothermal behavior and provide an intuitive guide for optimal heating efficiency. As mentioned previously, the thermofluidic analysis was divided into two phases. In the first phase, a thermal analysis was performed to predict the power level required to heat the fluid around nanoframes of varying sizes (L and W) from an ambient temperature of 300

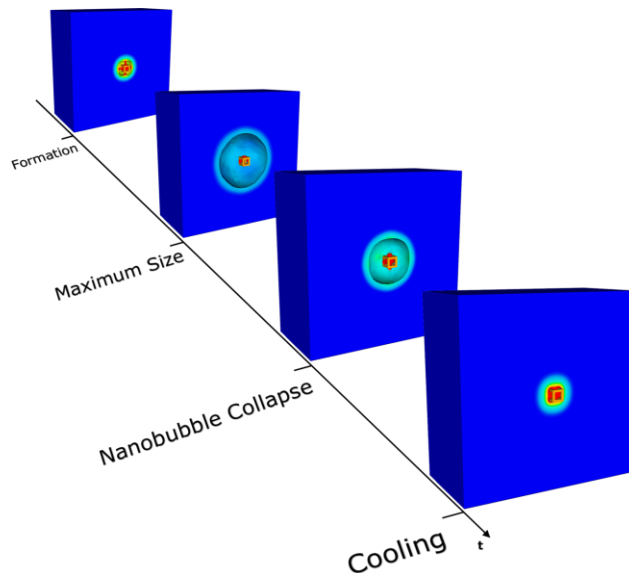
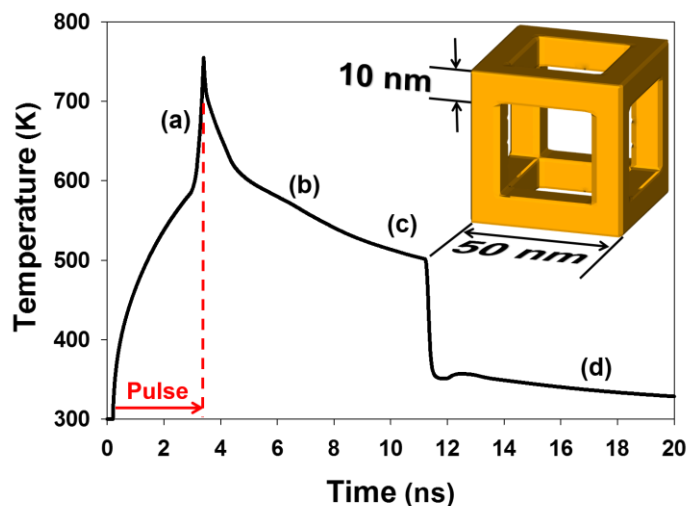


Figure 3.17. Photothermal heat cycle of a nanoframe ($L = 50$ nm, $W = 10$ nm) (cutaway perspective of heated nanocage): plot of nanoframe temperature vs. time, pulse duration indicated by red arrow and dashed line and inset plots showing various phases of the thermal cycle; (a) nanobubble formation, (b) nanobubble (maximum size), (c) nanobubble collapse, (d) cooling.

K to the superheat temperature of water i.e. 580 K. The heating process depends on the pulse intensity and duration, which was constrained to be between 3 to 5 ns. The nanosecond pulse duration far exceeds the characteristic time constants (femto- to picoseconds) for non-equilibrium energy transfer mechanisms that occur in gold nanoparticles and are therefore consistent with the continuum modeling approach taken here. Once the preliminary thermal calculations were completed, we performed the second phase of analysis where we applied the power levels obtained in the phase one analysis with a slightly increased pulse duration in order to heat the nanoframes beyond the superheat temperature, which causes vaporization of the surrounding fluid and bubble nucleation. The pulse duration was tuned so that the nanoparticle achieved a temperature that was sufficiently high to generate a sustained nanobubble, but low enough (< 1100 K) to avoid melting or vaporizing the nanoparticle. A summary of key simulation parameters, such as

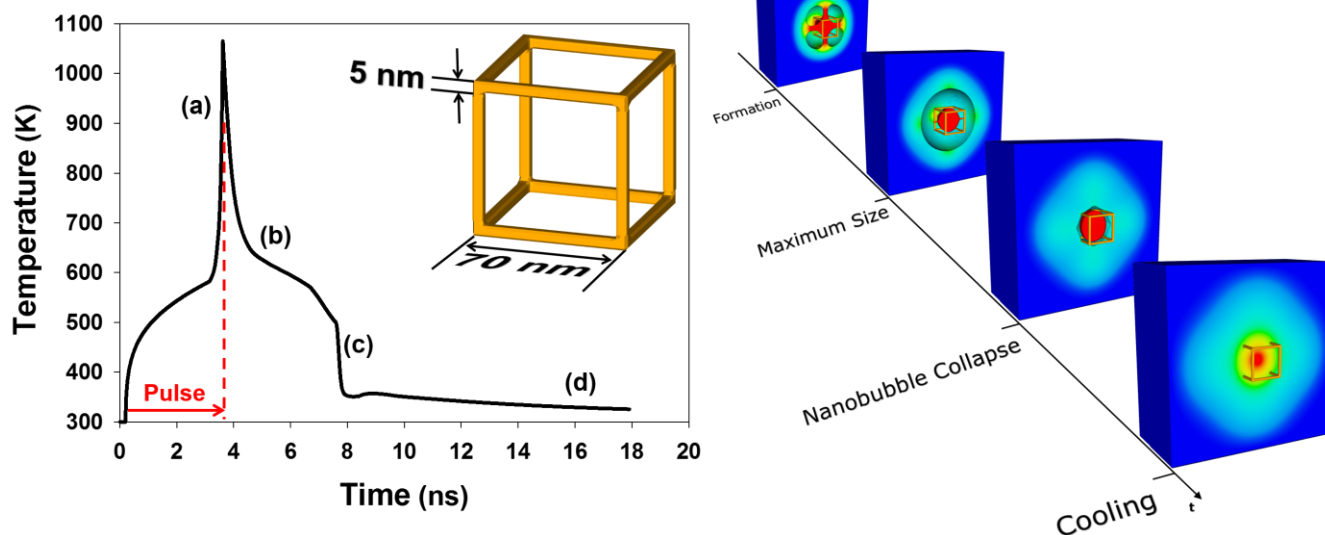


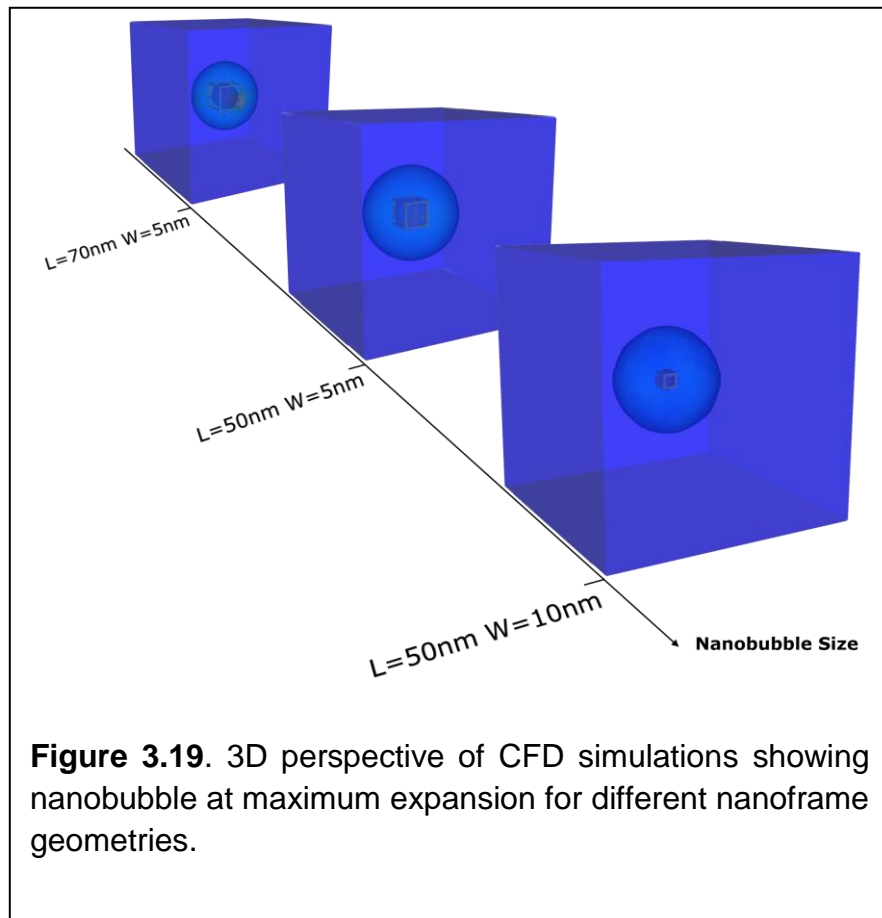
Figure 3.18. Photothermal heat cycle of a nanoframe ($L = 70$ nm, $W = 5$ nm) (cutaway perspective of heated nanocage): plot of nanoframe temperature vs. time, pulse duration indicated by red arrow and dashed line and inset plots showing various phases of the thermal cycle; (a) nanobubble formation, (b) nanobubble (maximum size), (c) nanobubble collapse, (d) cooling.

power and pulse duration required for the nucleation of an explosive nanobubble around each geometry, is given in **Table 1** found at the end of the chapter. **Figures 3.16, 3.17** and **3.18** illustrate simulation results for nanoframes with the following dimensions: $L = 50$ nm – $W = 5$ nm, $L = 50$ nm – $W = 10$ nm and $L = 70$ nm – $W = 5$ nm, respectively. These figures show a plot of the nanoparticle temperature vs. time and inset pictures of the nanoframe and the fluid temperature at various phases of the nanobubble cycle. The photonic analysis indicated that while all the geometries listed here have absorption peaks in the NIR, the two nanoframes with thinner frame elements, i.e. $L = 50$ and 70 nm with $W = 5$ nm only had minor peaks, i.e. their dominant absorption occurred at a longer wavelength. On the other hand, the nanoframe with thicker frame elements ($L = 50$ nm, $W = 10$ nm) had a dominant absorption in the NIR and a corresponding absorption cross-section that was ~ 2 orders of magnitude higher than the other geometries. In fact, we

found that nanoframes with more densely packed (i.e. thicker and more closely spaced) frame elements provide more efficient photothermal heating and larger nanobubbles due to enhanced LSPR coupling and cooperative heating between the elements.

3.4.3.3 An example of the photothermal-nanobubble heat-cycle for a nanoframe with $L = 50$ nm and $W = 5$ nm is shown in **Fig. 3.16**. The nanoframe and the fluid are initialized at a temperature of 300 K. The nanoframe is illuminated by a nanosecond pulsed laser that is operating that the LSPR wavelength of the nanoframe, in this case, $\lambda = 1500$ nm. The temperature of the nanoframe rises steadily for the first few nanoseconds as indicated in the temperature vs. time plot of **Fig. 3.16**. The fluid around the nanoframe reaches its superheat temperature (580 K) 2.8 ns after the onset of illumination, at which

time a homogeneous water vapor bubble is nucleated around it. Upon nucleation, the temperature of the nanoparticle rises rapidly since it is being insulated by a thin sheath of vapor while still being heated by the laser. This continues until the end of the laser



pulse, which coincides with the bubble formation and maximum temperature as shown in plot segment and inset (**Fig. 3.16a**). The pulse duration is 3.18 ns as indicated by the red dashed line. After it is nucleated the nanobubble expands because of its higher pressure compared to the surrounding fluid. The nanobubble reaches a maximum size as shown in inset **Fig. 3.16b**. For this geometry, the maximum bubble radius achieved was ~ 120 nm. Eventually, the nanobubble collapses bringing fluid back in contact with the nanoparticle after 7.8 ns as shown in plot segment and inset **Fig. 3.16c**, reducing its temperature to the ambient temperature (**Fig. 3.16d**). An interesting observation of this process is the formation of a hot mass of fluid in the middle of the nanoframe, which only partially evaporates as the nanobubble expands but does not reach superheat temperature. This phenomenon allows for the cooling of the nanoframe during the nucleation of an explosive nanobubble around it, thus maintaining its temperature below melting i.e. 1100 K, for the entirety of the photothermal heat cycle. For comparison purposes, we provide a transparent 3D perspective of the maximum expansion of the nanobubbles generated around all the geometries studied in order of maximum size as shown in **Fig 3.19**. This figure clearly illustrates that nanoframe geometries with more concentrated metallic mass are capable of generating nanobubbles of larger radius (Karampelas et al. 2016).

3.5 Summary of Combined Modeling Effort

3.5.0.1 Thus far, we have demonstrated the development and results of combined computational electromagnetic and CFD-based models for 5 different geometries, nanospheres, nanorods, nanorings, nanotori and nanocages/nanoframes. In short, using the combined approach we were able to predict the plasmon resonance wavelength for each geometry, the pulse duration and power required for sustained nucleation while avoiding potential damage to the nanoparticle and the dynamic behavior of the bubble as it expands and collapses. Although, the focus of our initial effort was modeling nanoparticles exhibiting axial symmetry, such as nanospheres and nanorods, we also proceeded to determine the aforementioned for 3D geometries such as nanoframes. Modeling non-symmetric nanoparticles was an extremely more complicated task that required vast amounts of computational resources. To the best of our knowledge, no similar numerical studies have been reported in scientific literature. The results of our modeling effort for specific can be summarized in **Table 1**.

3.5.0.2 Although our results are focused to a certain number of geometries, the methods described herein are directly applicable for any nanoparticle morphology. However, further computational research may be required for variations of already modeled geometries such as nanoparticles of different dimensions and materials as well as additional geometries e.g. nanostars or nanoframes of different shape. Therefore, for our future work, the models described in the previous sections should be further extended in order to capture all possible cases, thereby creating a more complete and

comprehensive ensemble that will form the basis for a rational design guide of future plasmon-based photothermal processes.

Nanoparticle Type	Radius, Dimensions (nm)	Power (μW)	Pulse Duration (ns)	Laser Irradiance ($\text{mW}/\mu\text{m}^2$) (λ nm)	Maximum Nanoparticle Temperature (K)	Maximum Bubble Radius (nm)	Nucleation Time (ns)	Maximum Bubble Time (ns)
Nanosphere	R=30	152	5	14 (532)	1080	50	3.8	5.6
Nanorod	L=60, r=8.5	76.8	1.9	10 (770)	915	65	2.7	3
Nanoring (h=20nm)	R=50, r=30	252	4	27.07 (935)	862	95	3.5	6.3
	R=40, r=20	192	3.8	11.79 (793)	984	85	3.2	5.5
	R=30, r=10	127.2	4.1	6.94 (662)	972	50	3.5	4.8
Nanotorus	R=40, r=10	259.2	3.1	21.82 (986)	889	70	2.7	4.9
	R=30, r=10	172.8	4.1	10.06 (825)	1000	80	3.4	5.4
	R=20, r=10	115.2	4.1	7.94 (680)	773	65	3.7	5.6
Nanoframe	L=50, W=5	180	3.18	209 (1500)	977	120	2.8	6.8
	L=50, W=10	200	3.2	4.96 (1015)	754	185	3.0	5.7
	L=70, W=5	288	3.42	633 (1500)	1068	95	3.2	4.5

Table 3.1. Summary of modeled nanoparticle geometries with heating and nanobubble parameters.

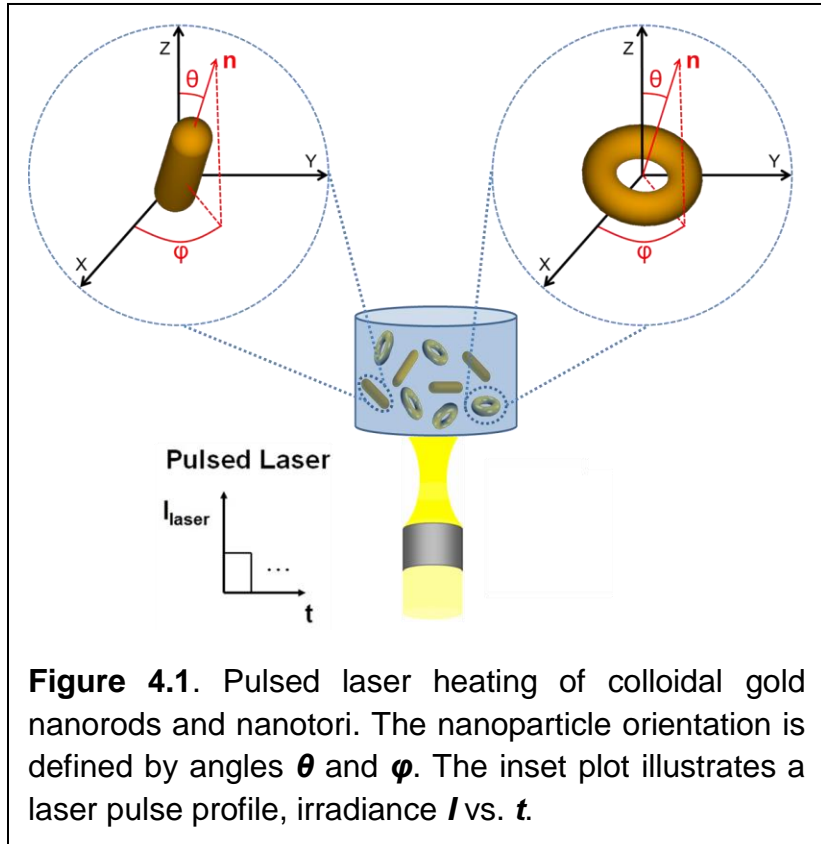
Chapter 4: Colloidal Photothermal Modeling

4.0 Since most in vivo applications involve a solution of nanoparticles, our modeling effort will now be extended to include additional computational models that predict the colloidal photothermal or optical behavior of various nanostructures. We begin with numerical simulations of the absorption of incident light by nanoparticles rotated in different orientations. This modeling work will be used to determine not only the types of nanoparticles that are characterized by LSPR in the NIR but also their overall absorption cross-section independent of orientation at this wavelength range. A number of thermal models predicting heating of a colloidal solution of identical nanoparticles under pulsed illumination as a function of nanoparticle separation distance will also be developed. Such models will serve as indicators of the energy required for sustained nucleation when particle aggregates are formed. As it can be seen from SEM and TEM images in previous sections, nanoparticles in a solution are rarely encountered in isolation but rather as a parts of a larger population. These types of groups of nanoparticles have also been experimentally identified by numerous in vitro experiments showing aggregation inside targeted cells (Albanese and Chan 2011; Chithrani et al. 2006; Hotze et al. 2010). This phenomenon could be used to increase the localization and effectiveness of nanobubble treatment. By lowering the irradiance and/pulse duration and relying on cooperative heating effects, larger nanobubbles are possible with reduced power. This statement can be confirmed by models of cooperative nanobubble nucleation around identical nanoparticles described below. Overall, the colloidal modeling effort serves to extend the application of Chapter 3 models in more realistic in vivo or in vitro environments. In all Chapter 4 models all material properties are considered constant.

4.1 Photonic Models for Nanoparticles at Varying Orientations

4.1.1 Absorption Spectra of Gold Nanorods and Nanotori at Discrete Rotations

4.1.1.1 In this section we compare photothermal energy conversion for colloidal nanorods and nanotori. In order to determine their heating efficiency, it is necessary to quantify their absorption as a function of orientation. For all geometries studied in this section, the orientation can be specified using angles φ



and θ that define the rotation of axis of the particle relative to the x - and z -axis, respectively. **Figure 4.1** illustrates colloidal nanorods and nanotori being illuminated with a pulsed laser and a reference frame showing the angles φ and θ that define the orientation of the particles. Throughout this analysis the incident field is assumed to be linearly polarized along the x -axis and propagating downward with k in the z -direction as shown in our previous photonic analyses e.g. **Figs. 3.5** and **3.9**. The inset plot in **Fig. 4.1** depicts the pulse profile (irradiance I_{laser} vs. t) for the laser. In this figure, n is the unit vector along the axis of the particle. For the nanorod, n is along its length, whereas for a

nanotorus and similarly for a nanoring, \mathbf{n} is along its axis of rotation. The angle φ lies in the \mathbf{x} - \mathbf{y} plane and is measured from the \mathbf{x} -axis to the projection of \mathbf{n} onto that plane, whereas θ is the angle between \mathbf{n} and the \mathbf{z} -axis. As noted above, we assume that the incident field is linearly polarized along the \mathbf{x} -axis, shown in **Figs. 3.5** and **3.9**. As a point of reference, the nanotorus shown in **Fig. 3.9** has an orientation ($\theta = 0^\circ$, $\varphi = 0^\circ$) and is aligned parallel to polarization, i.e. the E field is parallel to the face of the torus, perpendicular to its axis. The torus is aligned perpendicular to the polarization when ($\theta = 90^\circ$, $\varphi = 0^\circ$) or ($\theta = 90^\circ$, $\varphi = 90^\circ$). Similarly, a nanorod, as shown in **Fig. 4a**, is oriented parallel (longitudinal) to the polarization when ($\theta = 90^\circ$, $\varphi = 0^\circ$).

4.1.1.2 We first study the nanorod. It is well-known that there are two distinct LSPR frequencies for this geometry that correspond to transverse and longitudinal polarization modes, respectively. A higher LSPR frequency (shorter wavelength) occurs for transverse alignment, whereas a lower resonant frequency (longer wavelength) is obtained for parallel alignment. Moreover, the latter depends on the aspect ratio (diameter/length) of the nanorod and can be tuned through synthesis for a specific application. The ability to tune LSPR in this fashion has spawned a growing interest in the use of gold nanorods, especially for bioapplications that require NIR wavelengths to achieve more effective penetration of light into a target tissue. As in section 3.2, we model the nanorod as a cylinder with hemispherical caps. Similarly to our previous analysis, the length and diameter of the nanorod are 60 nm and 17 nm, respectively, which define an aspect ratio of 0.28. We compute the absorption spectra for five different orientations that range from parallel to transverse alignment in 30° increments: ($\theta = 0^\circ$, $\varphi = 0^\circ$), ($\theta = 30^\circ$, $\varphi = 30^\circ$), (θ

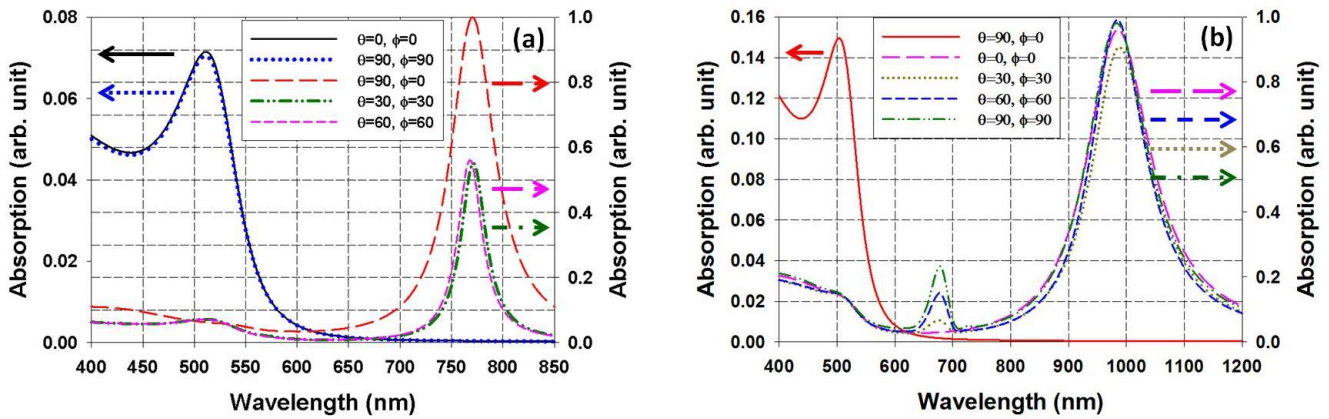


Figure 4.2. Normalized absorption spectra with nanoparticles at different orientations: (a) Nanorod ($L = 60$ nm, $R = 8.5$ nm) and (b) Nanotorus ($R = 40$ nm, $r = 10$ nm).

= 60° , $\varphi = 60^\circ$), ($\theta = 90^\circ$, $\varphi = 90^\circ$) and ($\theta = 90^\circ$, $\varphi = 0^\circ$). The normalized absorption spectra for these orientations are plotted in **Fig. 4.2a**. The normalization is with respect to the peak absorption at parallel alignment. Note that as the nanorod rotates from parallel towards perpendicular alignment, the absorption decreases and the LSPR wavelength gradually shifts towards shorter wavelengths. These effects are nonlinear functions of the orientation and are more pronounced with greater the rotation. Note that when the nanorod is aligned perpendicular to the polarization, i.e. for ($\theta = 0^\circ$, $\varphi = 0^\circ$) and ($\theta = 90^\circ$, $\varphi = 90^\circ$), the normalized absorption is significantly reduced and its amplitude needs to be plotted on a separate (left side) axis. Overall, this analysis shows that when a colloid of nanorods is illuminated with the LSPR wavelength for parallel alignment, the absorbed power decreases substantially for misaligned nanorods, which reduces the overall colloidal heating efficiency.

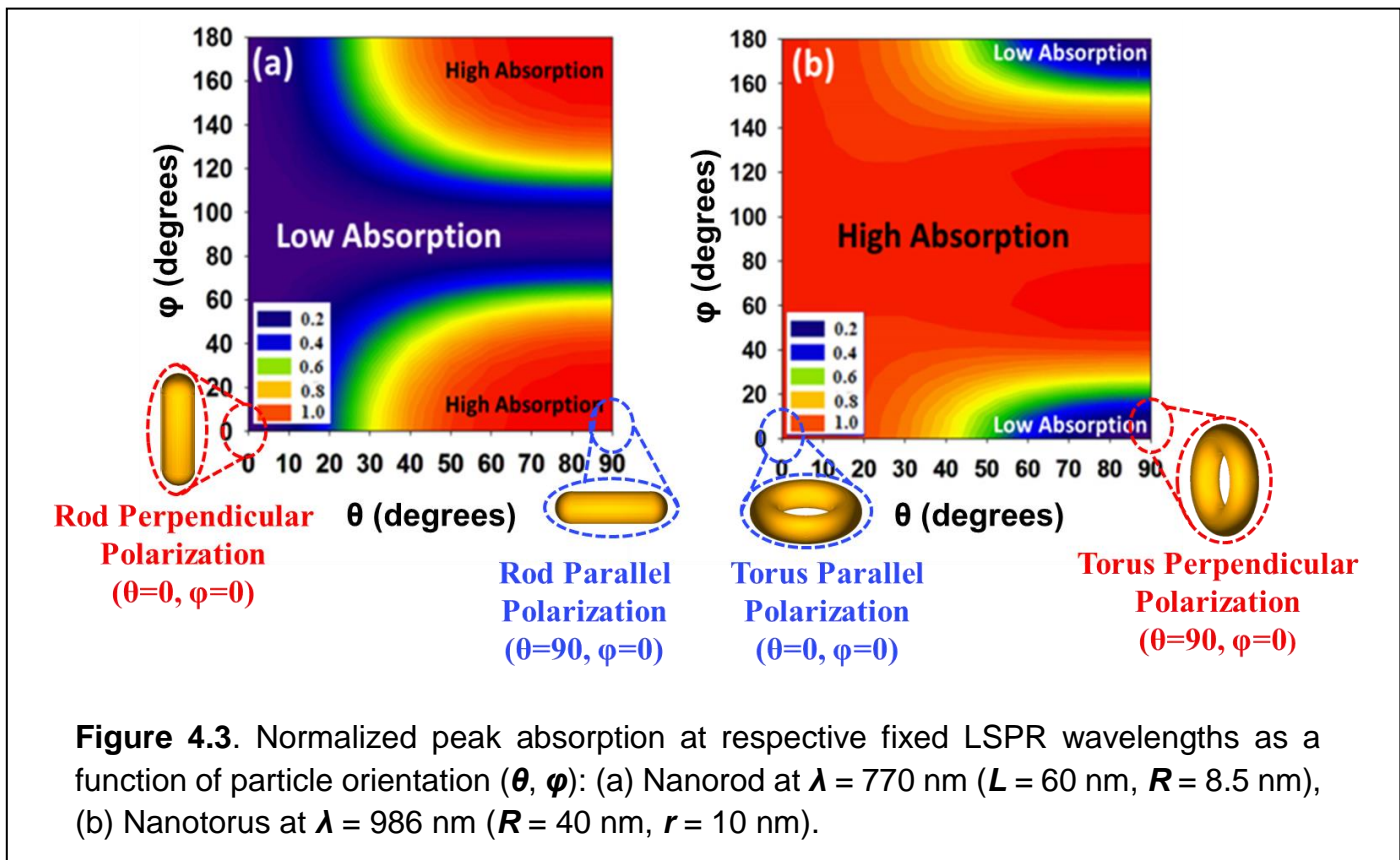
4.1.1.3 A similar analysis was performed for the nanotorus. This geometry is defined by its major and minor radii, r and R , respectively, as shown in **Fig. 3.7b**. The

LSPR for the torus has been investigated using closed-form expressions (Dutta et al. 2008) for both parallel alignment ($\theta = 0^\circ$, $\varphi = 0^\circ$) (**Fig. 3.9a**) and perpendicular alignment ($\theta = 90^\circ$, $\varphi = 0^\circ$). We compute the absorption spectra for a nanotorus with $R = 40$ nm and $r = 10$ nm, i.e. with an aspect ratio of 0.25. As in the case of the nanorod, the resonant wavelength can be tuned to the NIR by adjusting the aspect ratio r/R . We determine the absorption spectra of the nanotorus for five different orientations, as above. These are plotted in **Fig. 4.2b**. Note that in contrast to the nanorod, there is more overlap in the absorption spectra at different orientations and the LSPR wavelength first red-shifts slightly and then blue-shifts as the torus rotates away from parallel towards perpendicular alignment. This suggests that nanotori would provide more efficient colloidal heating than the nanorods due to their relatively higher absorption at different orientations.

4.1.2 Absorption Comparison of Gold Nanorods, Nanotori and Nanorings

4.1.2.1 We compare the absorption for these geometries over the full range of orientations, i.e. $0 \leq \theta \leq 90^\circ$ and $0 \leq \varphi \leq 180^\circ$. This is a complex function of the geometry (especially the aspect ratio), the dielectric function of each particle, its orientation (θ , φ), as well as the dielectric properties of the background medium. Numerical analysis is needed to study of these effects. We used full-wave analysis as described above to predict the normalized peak absorption contours at different orientations, as shown in **Fig.**

4.3.



4.1.2.2 In this analysis, the nanorod and nanotori at different orientations are illuminated with their respective LSPR wavelengths obtained for parallel orientation, in this case 770 nm and 986 nm, respectively. The idea is to determine the fall off in the peak absorption under a fixed illumination as the particles take on different orientations. It is clearly illustrated in **Fig. 4.3** that the nanorod has a substantially decreased peak absorption at most orientations except for those nearly aligned with the polarization (e.g. $\theta = 90^\circ$, $\varphi = 0^\circ$). This is in sharp contrast to the nanotorus, which exhibits a relatively high peak absorption throughout a wide range of possible orientations.

4.1.2.3 Nanorings are closely related to nanotori in terms of their plasmonic behavior. Of the two structures, nanorings are currently easier to fabricate because their rectangular features can be realized using planar lithographic techniques. Au nanoring

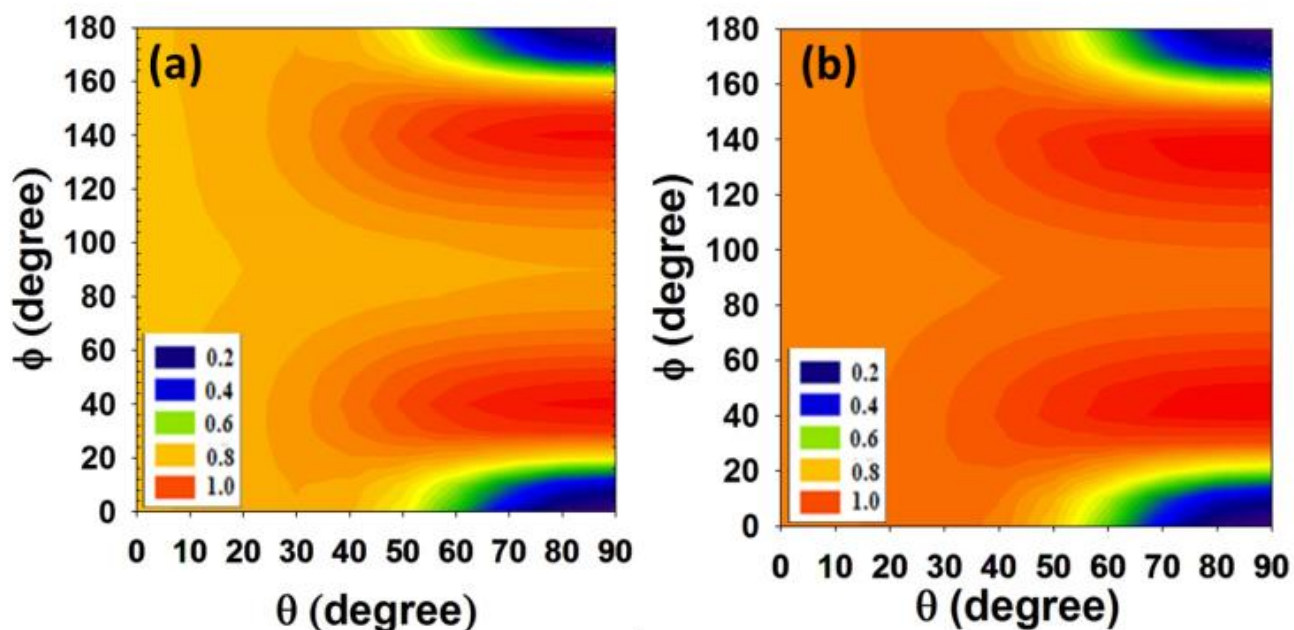


Figure 4.4. Normalized peak absorption at respective fixed LSPR wavelengths as a function of particle orientation (θ , φ): (a) Nanoring at $\lambda = 793$ nm ($R = 40$ nm, $r = 20$ nm), (b) Nanotorus at $\lambda = 825$ nm ($R = 30$ nm, $r = 10$ nm).

colloids have been developed by first fabricating the structures on a substrate and then releasing them into solution. The normalized peak absorption vs. orientation of nanorings are essentially the same as those of nanotori as shown in **Fig. 4.4**. In this analysis the nanoring and nanotorus have comparable dimensions. The nanoring has inner and outer radii of 20 nm and 40 nm, respectively. All the nanorings analyzed in the paper have a height of 20 nm. The nanotorus has the same dimensions as above, $R = 30$ nm, $r = 10$ nm. The nanoring and nanotorus at different orientations are illuminated with their respective LSPR wavelengths obtained for a parallel orientation, i.e. 793 nm and 825 nm, respectively. Specifically, these wavelengths are held constant as the particle orientations change. The analysis shown in **Fig. 4.4** indicates that nanorings and nanotori can be essentially interchanged for photothermal applications (Alali et al. 2013).

4.1.3 Absorption Cross-Section of Nanoframes under Different Orientations

4.1.3.1 While many groups have studied the optical response of nanoframe structures as a function their geometry, to our best knowledge, this is the first such analysis with respect to orientation. Similarly to previous the studies explained in previous subsections, we investigate the LSPR absorption of a nanoframe as a function of its orientation with respect to the polarization of the incident light. This is important for applications involving colloids where nanoframes have random orientations within a carrier fluid as illustrated in **Fig. 4.5a**. Since nanoframes have a relatively high degree of geometric symmetry we expect that their LSPR absorption will be somewhat insensitive to their orientation. Here, we quantify the orientation dependence for the first time.

4.1.3.2 The orientation of the nanoframe can be specified using angles φ and θ that define the rotation of the particle relative to the \mathbf{x} - and \mathbf{z} -axis, respectively. Throughout this paper the incident field is assumed to be linearly polarized along the \mathbf{x} -axis and propagating downward, i.e. with \mathbf{k} in the \mathbf{z} -direction as shown in **Fig. 3.14a**. **Figure 4.5a** illustrates a colloid of nanoframe structures being illuminated with a pulsed laser. A reference frame is shown along with angles φ and θ that define the orientation of the nanoframe. The inset plot in **Fig. 4.5a** depicts the laser pulse profile (irradiance I_{laser} (W/m^2) vs. t). In this figure, \mathbf{n} is a unit vector that describes the orientation of the nanoframe. Specifically, \mathbf{n} is normal to the top area, as shown. The angle φ lies in the \mathbf{x} - \mathbf{y} plane and is measured from the \mathbf{x} -axis to the projection of \mathbf{n} onto \mathbf{x} - \mathbf{y} plane, whereas θ is the angle between \mathbf{n} and the \mathbf{z} -axis. We perform parametric calculations of σ_{abs} for the

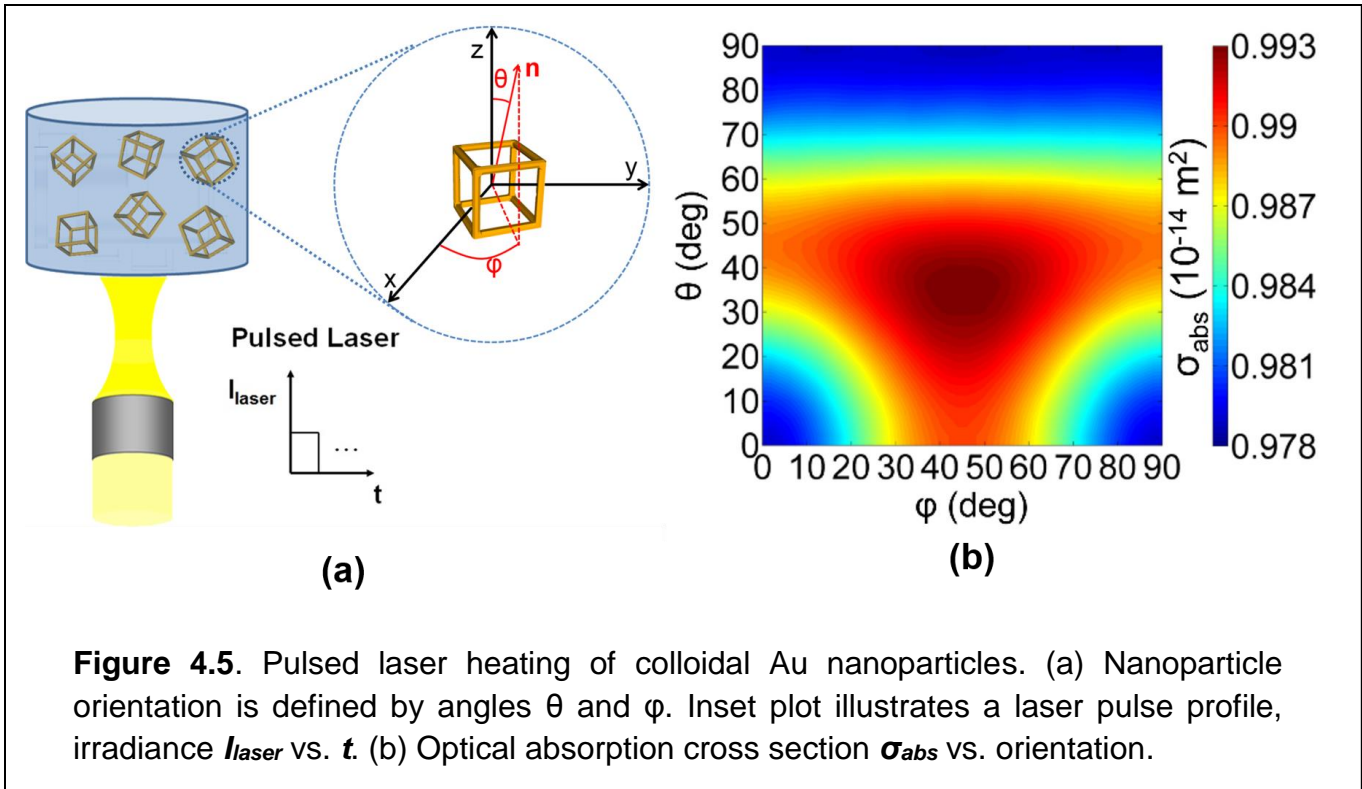


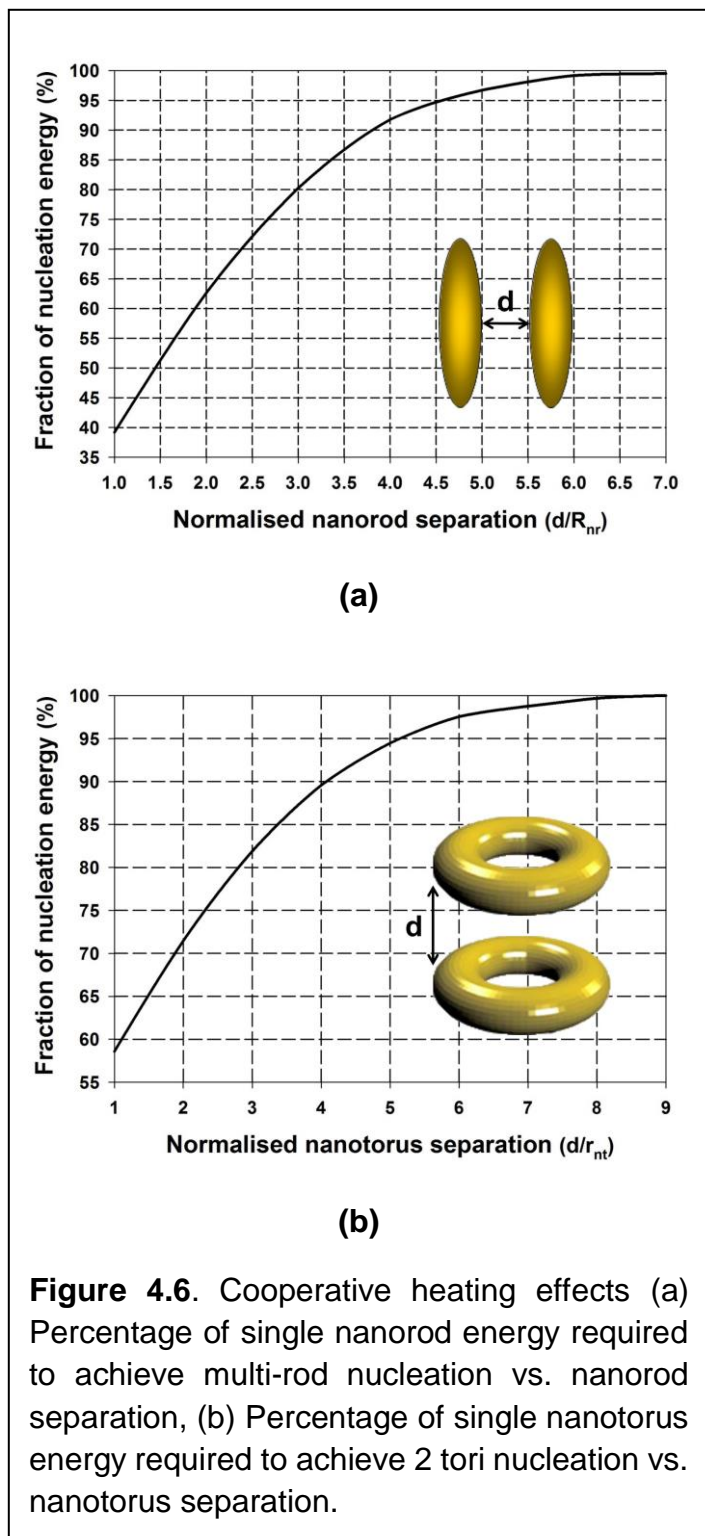
Figure 4.5. Pulsed laser heating of colloidal Au nanoparticles. (a) Nanoparticle orientation is defined by angles θ and ϕ . Inset plot illustrates a laser pulse profile, irradiance I_{laser} vs. t . (b) Optical absorption cross section σ_{abs} vs. orientation.

nanoframe as a function of its orientation with respect to the incident polarization. In our analysis, the nanoframe is illuminated by an x -polarized light at the LSPR peak wavelength. We analyze an Au nanoframe with $L = 28$ nm and $W = 7$ nm, which has an LSPR peak wavelength of 830 nm. The absorption cross section σ_{abs} of the nanoframe is plotted in **Fig. 4.5b**. Note that there is very little variation in σ_{abs} throughout the entire range of orientations. This is desired for applications such as photothermal cancer treatment as it implies a higher heating efficiency for a given laser irradiance (Karampelas et al. 2016). However, in order to quantify the behavior of the nanoparticle in fluid and the amount of energy required for the generation of nanobubbles, we perform a CFD analysis described in the following section.

4.2 Colloidal Heating of Identical Nanoparticles

4.2.1 Gold Nanorods

4.2.1.1 Following our photonic analysis, we performed a number of thermal simulations of multi particle systems. Such nanoparticle aggregates are very common during bottom up fabrication or when appropriately functionalized nanoparticles are uptaken by targeted cells in vitro or in vivo (Albanese and Chan 2011; Chithrani et al. 2006; Hotze et al. 2010). We begin with a multi-nanorod system to examine effects of cooperative heating. In this case, we studied an evenly spaced 3-dimensional array of nanorods that are 60 nm in length and 17 nm in diameter, i.e. identical to the single nanorod system presented in section 3.2. We systematically varied the surface-to-



surface spacing between the nanorods from 1 to 7 radii, in both r and z directions. We used 3D CFD analysis (without phase change) with a computational domain that spanned from 12.75 nm to 38.25 nm in both x and y directions and from 34.25 nm to 59.75 nm in the z direction, depending on the distance between the nanorods. Using the same amount of power in each nanorod as in the single nanorod case, we calculated the pulse duration that is required to heat the nanorods to the superheat temperature. The results of this parametric analysis are presented in **Fig. 4.6a**. Based on our calculations, it can be concluded that for a distance of 1 radius between the nanorods, only 39% of the energy is required to reach the nucleation temperature as compared to the single nanorod system. Moreover, all cooperative heating effects become negligible after a distance of 7 radii in all directions.

4.2.2 Gold Nanotori

4.2.2.1 A parametric thermal analysis was performed to examine the cooperative heating effects of the 2-tori system. Using the same amount of power (172.8 μW) as in the single torus case, we calculated the pulse duration required for the temperature of the tori to reach the superheat temperature. This analysis was performed for a range of torus-to-torus spacing spanning 1 to 10 minor radii between the edges of the tori (i.e. 10 to 100 nm). We used an axisymmetric model with a computational domain that spanned 200 nm and 200-245 nm in the r and z directions, respectively (depending on the distance between the tori). The results of this analysis are presented in **Fig. 4.6b**. Note, for example, that for a distance of 1 radius between the tori, the energy required to achieve

the superheat temperature is only 58% of that of the single torus system. In addition, all cooperative heating effects become negligible after a separation distance of 9 radii. Having examined the cooperative heating effects between nanoparticles, we will apply such principles for a multiparticle system undergoing a photothermal nanobubble cycle.

4.3 Cooperative Nanobubble Nucleation

4.3.1 System of Two Nanotori

4.3.1.1 In this section we explain the behavior of a two-nanoparticle system under pulsed illumination. Similarly to the combined modeling work reported in Chapter 3, the principles of CFD photothermal nanobubble modeling will be applied to a 2 tori system. We opted for this geometry since it is characterized by a high degree of rotational symmetry and has high absorption independent of orientation. Hence, the light energy absorbed by the two particles will be assumed to be identical while we focus our attention to the effects of cooperative heating in nanobubble nucleation. For this analysis, the distance between the centers of the tori was set to 60 nm (i.e. 4 minor radii spacing, edge-to-edge). We used an axisymmetric model in which the computational domain spanned 200 nm and 215 nm in the r and z directions, respectively, with a 1 nm cell size in both directions. Symmetry boundary conditions were imposed along both the r - and z -axes. The former accounted for the second torus while the latter accounted for their axial symmetry. The same initial and boundary values as in the single torus case were applied (see section 3.3). We first determined a range of viable power levels and pulse durations and then used this data in a parametric CFD phase change analysis to select a power level and pulse duration that are sufficient to generate a bubble without damaging the tori. It was found that respective values of 72.8 μW and 3.45 ns would serve this purpose. The fluidic analysis at this power and pulse duration is shown in **Fig. 4.7**. This plot shows the temperature of the tori and corresponding images that show the generation and collapse of combined nanobubbles.

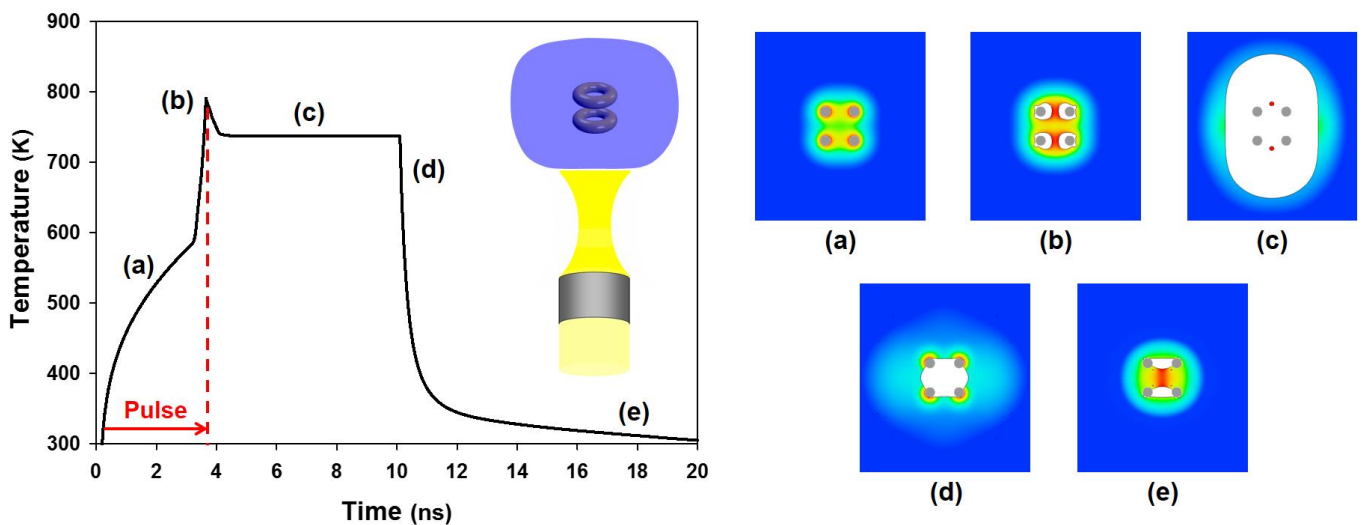


Figure 4.7. Photothermal heat cycle of a 2 identical nanotori system ($R= 30$ nm and $r = 10$ nm) (cross-sectional view): plot of nanorod temperature vs. time, pulse duration indicated by red arrow and dashed line and inset plots showing various phases of the thermal cycle; (a) initial heating, (b) nanobubble formation, (c) nanobubble (maximum size), (d) nanobubble collapse, (e) cooling.

4.3.1.2 Initially, the tori are at ambient temperature and after 0.2 ns they are illuminated. During the first 2.9 ns of heating, their temperature gradually increases to the superheat temperature, at which point, separate bubbles start to nucleate around the tori (**Fig. 4.7a**). It should be noted that this heating process requires 10% less energy than the single torus system, due to cooperative heating effects between the tori, as predicted by our parametric analysis shown in **Fig 4.6b**. Once the tori are partly surrounded by vapor, the heat transfer from their surface is negligible and their temperature increases rapidly as they continue to absorb energy. The tori reach an instantaneous peak temperature of approximately 790 K, which occurs at the end of the heat pulse (3.45 ns) at which point they are partially surrounded by liquid (**Fig. 4.7b**). This remaining liquid

completely evaporates at approximately 4.2 ns after the onset of heating, and during evaporation the tori cool from their peak temperature to 740 K.

4.3.1.3 As soon as the bubbles have nucleated, they expand and as they do so, isolated drops of hot fluid form within the bubble close to the tori, similar to what was observed in the single torus system (shown in **Fig 3.11**). The bubbles eventually merge and continue to grow as a single bubble, which reaches its maximum size 6.3 ns after the onset of heating. At its largest extent, the bubble has an elliptical shape of approximately 95 nm and 150 nm in the r and z directions, respectively (**Fig. 4.7c**). Eventually, 10 ns after onset of heating, the nanobubble collapses bringing fluid back in contact with the tori. A minor bubble forms in the space between the tori and shrinks slowly due to a relatively weak capillary force (**Fig. 4.7d**). The tori are then further cooled to ambient temperature and the bubble shown in **Fig. 4.7d** transforms into 2 smaller bubbles (**Fig. 4.7e**). It should also be noted that, due to relatively weak capillary forces (corresponding to a large radius of curvature at the liquid-vapor interface) the nanobubbles shown in **Fig. 4.7e** require a substantial amount of time to completely collapse. As with all systems studied, the number of bubbles generated and their dynamics can be controlled by tuning the power level and duration of the heat pulse. In conclusion, the 2 coaxial tori system was able to generate a bubble approximately 3.6 times larger than in the single torus case while requiring less than 85% of the energy consumed by a single torus system.

4.4 Summary of Colloidal Modeling Effort

4.4.0.1 In Chapter 4, we developed computational electromagnetic and fluidic models that pertain to the colloidal behavior of plasmonic nanoparticles. More specifically, we performed colloidal heating and cooperative bubble nucleation CFD modeling along with photonic analysis of nanoparticles at varying orientations. In summary, we observed that colloidal heating for nanobubble nucleation is very important for nanoparticles that are in relative close proximity while the effects diminish for less concentrated solutions. When nanobubble formation is the desired goal, it is shown that less energy is required and larger bubbles are observed for adjacent nanoparticles. In addition, we used computational modeling to demonstrate that colloidal plasmonic nanorings, nanotori and, even more so, nanoframes have advantageous absorption properties for photothermal applications because their level of absorption remains high over a broad range of orientations relative to the polarization of the incident field. These properties hold potential for applications such as photothermal cancer therapy as they can enable more efficient heating of malignant tissue and access to deeper tumors. The computational approach described herein provides insight into fundamental aspects of the photothermal process and enables rational design for novel applications. However, we believe that further modeling is required for cases involving geometries not studied herein e.g. core-shell nanoparticles. Therefore, in the following chapter we will suggest pathways of future work, in which the models described thus will be extended in order to capture more of the complex physical phenomena involved in cases of nanobubble treatment, directly addressing the knowledge gap concerning the colloidal photothermal behavior of plasmonic nanoparticles.

Chapter 5: Future Work Recommendations and Conclusions

Although, the models described in Chapters 3 and 4 represent the most accurate nanobubble modeling attempt performed thus far, at the time of writing, the assumptions of continuum theory, constant nanoparticle properties and constant absorption of light energy at every stage might lead to potential discrepancies between modeling and experimental results. Hence, in the interest of increased accuracy, we suggest the inclusion of additional modeling techniques or expanding current modeling effort through the addition of more physical models. More specifically, we propose the use of the Two-temperature Model (TTM) to describe non-equilibrium femto-second electron relaxation in the nanoparticle when such pulsing methods are employed. These models will enable the proposed modeling methodology to be extended to femto- and pico-second pulsing. In addition, a further refinement of the models developed in Chapters 3 and 4 could be realized with the inclusion of temperature dependent properties for the fluid and the nanoparticle. By adding temperature dependent properties to all materials involved, current models could become inherently more accurate. Finally, in order to account for the changes in refractive index that may occur post-nucleation if pulsing durations are sufficiently long, we suggest a separate analysis to be performed. This type of approach could be used to determine the fall off peak absorption when a nanoparticles are illuminated during the early formation stage of a nanobubble. This analysis could predict a drop in the absorbed power when nanoparticles are surrounded by vapor. Overall, the combination of non-equilibrium effects, temperature pertinent properties and nucleation-step photonic modeling will provide most sophistication to an already complex modeling effort.

5.1 Future Work Recommendations

5.1.1 Two-Temperature Model for Femto- and Pico-Second Pulsing

5.1.1.1 The Two-Temperature Model (TTM) can be used to describe the non-equilibrium state between electrons and the lattice occurring when metallic sample is excited by a laser pulse or an electric field is applied. According to the TTM, the metal is assumed to be composed by two interacting subsystems: electrons and phonons because the time necessary to achieve equilibrium in the electron gas is much less than the time required to establish equilibrium between the electrons and the lattice phonons. The hot degenerate (thermalized) electron gas relaxes to the bath phonons with relatively slow electron-phonon interactions (Singh 2010).

5.1.1.2 When a metallic sample is illuminated by femto-second laser pulse then a non-equilibrium electron distribution is generated while the temperature of the phonon lattice remains unchanged due to the large difference between the heat capacities of electrons (C_{pe}) and phonons (C_{pp}). Consequently, over a period of hundreds of femto-seconds, the electron cloud returns to equilibrium through coulombic interactions while the temperature of the electron cloud (T_e) is higher than that of the protons (T_p). This phenomenon is called thermalized electron distribution. This excited thermalized electron gas then relaxes via electron-phonon interactions giving up the excess energy to the phonon bath. Therefore, the difference between the intra-electron and intra-phonon relaxation times justifies the two temperatures T_e and T_p . The Two-Temperature model can be summarized by the following coupled differential equations:

$$\frac{\partial(Cp_p T_p)}{\partial t} = -G(T_e - T_p) \quad (5.1)$$

$$\frac{\partial(Cp_e T_e)}{\partial t} = -G(T_e - T_p) \quad (5.2)$$

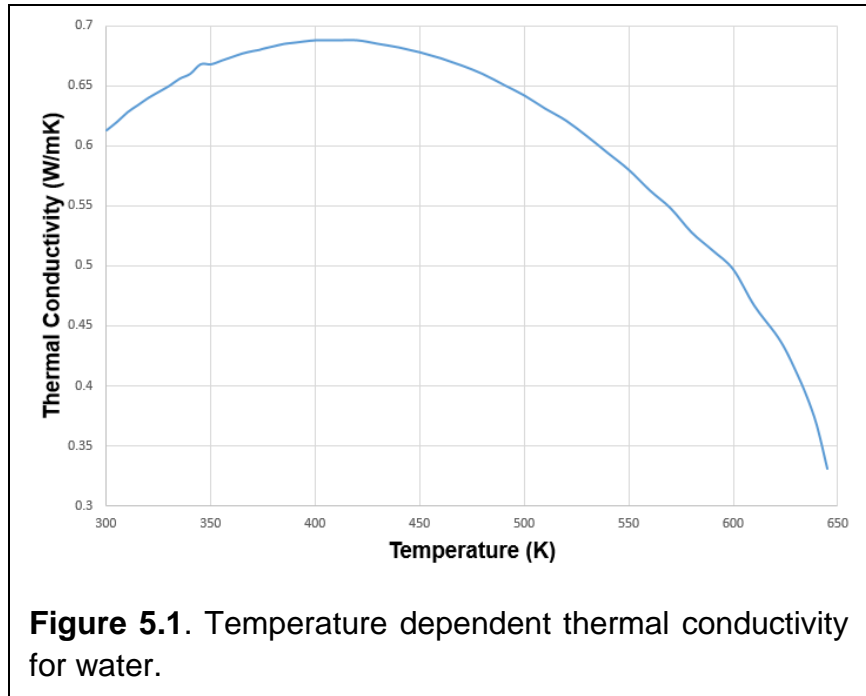
where G represents the electron-phonon interactions coefficient (Singh 2010).

5.1.1.3 We propose the use of the Two-Temperature Model for the description of femto- and pico-second laser pulsing being currently used in many experimental applications. The incorporation of the TTM in our simulations will enable more accurate modeling of ultra-short laser pulsing expanding our current modeling effort.

5.1.2 Temperature Dependent Material Properties

5.1.2.1 Since all the material properties were maintained at a constant value for the modeling effort described above we propose a further refinement with the use of temperature dependent properties for the models developed in Chapters 3 and 4. Since the temperature of the fluid and the nanoparticle might vary even by 800 K, the inclusion of temperature dependent properties will potentially provide a more accurate description of the photothermal process. The properties currently under consideration are: density, viscosity, specific heat, thermal conductivity and surface tension coefficient for the fluid and specific heat and thermal conductivity for the nanoparticles.

5.1.2.2 Thus far, preliminary results with only fluid temperature dependent properties indicate that variations in temperature can have a significant impact on the thermal behavior of the fluid resulting in reduced pulse times required for



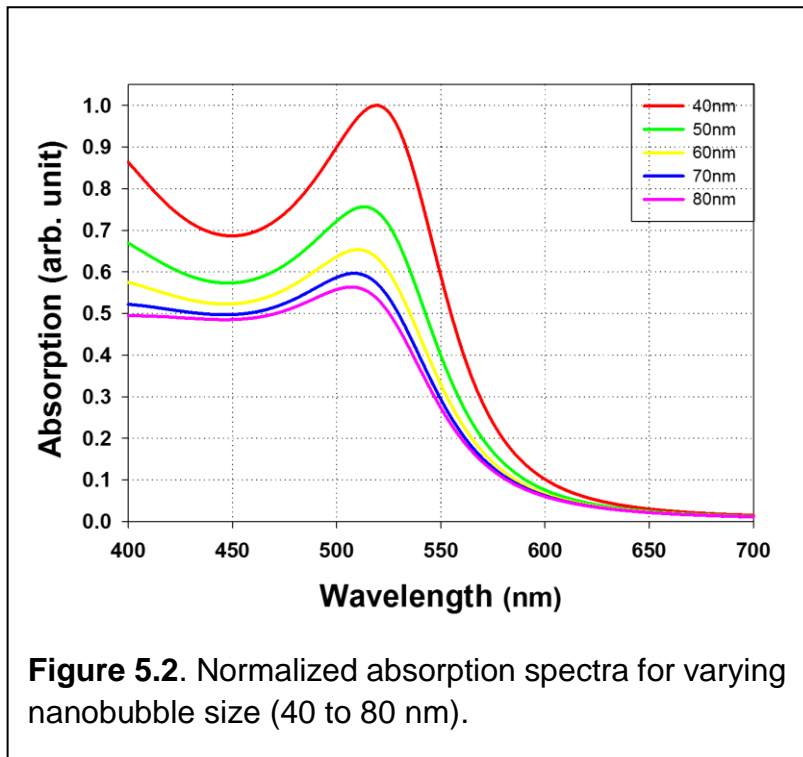
bubble generation. As seen in **Fig. 5.1**, the thermal conductivity for water varies significantly for the range of temperature considered in the models presented above. In addition, the behavior of the nanobubble is influenced by the temperature of the liquefied fluid at its border due to temperature dependent surface tension. The nanobubbles occurring under these conditions appear to be smaller in size than initially predicted.

5.1.2.3 Therefore, we propose the inclusion of temperature dependent fluid and nanoparticle properties in a future version of our models in order to provide the most accurate description of the nanobubble treatment process. As observed in the preliminary modeling effort, temperature can have a significant impact on the thermal behavior of the fluid.

5.1.3 Illumination during Nanobubble Formation

5.1.3.1 As seen in Chapter 3 models, there exist cases where the nanoparticle is still being illuminated for a small period of time ranging from 0.1 to 0.2 ns after the onset of a nanobubble formation. Compared to the total pulse duration, this post nucleation illumination represents less than 10% of the entire pulse duration. Nevertheless, we suggest a two-step transient photonic analysis approach. To the best of our knowledge such methods have never been implemented but could prove useful in determining the fall off peak absorption when a nanobubble is being formed around a nanoparticle while it is still being illuminated.

5.1.3.2 A preliminary analysis was performed for a spherical nanoparticle with a radius $r = 30$ nm similarly to section 3.1. The absorption of the nanoparticle was calculated for nanobubble radii spanning from 40 nm to 80 nm. In **Fig. 5.2**, a significant drop in absorption is observed with increasing



bubble size. Moreover, as the nanobubble expands, there is a negligible blue-shift in the

plasmon resonance wavelength. Further analysis would be recommended in order to expand the current work to additional nanoparticle geometries.

5.1.3.3 Based on the thermofluidic modeling explained in previous chapters, if illumination continues post-nucleation, the temperature of the nanoparticle rises rapidly since it is essentially insulated when surrounded by vapor. This represents a crucial fine tuning detail that has been identified thanks to our modeling effort. Hence carefully tuned pulse durations prevent nanoparticle damage and lead to increases of the overall efficacy of the treatment method by allowing the nucleation of robust nanobubbles with every laser pulse. However, current models could be further enhanced with a more accurate description of the crucial, rapid temperature increase, phase if the results of this analysis were incorporated.

5.2 Conclusions

5.2.0.1 The focus of this work was the study nanosecond-pulsed, laser-induced, plasmon-assisted bubble generation around subwavelength metallic nanoparticles in aqueous solutions and associated thermal and fluidic effects through advanced computational modeling. Our results include multiple nanoparticle geometries such as nanospheres, nanorods, nanotori, nanorings and nanoframes.

5.2.0.2 The modelling effort described herein offers a thorough explanation of the photothermal process: absorption of photonic energy by the nanoparticle at its plasmon resonance wavelength, subsequent increase in temperature within the particle, conductive heat transfer to the fluid, nanobubble formation and resulting behavior of the bubble and surrounding fluid during and after pulsed illumination.

5.2.0.3 In chapter 3 models, we applied a combined photonic-fluidic approach which resulted in initial estimates of the plasmon resonance wavelength for each of the aforementioned geometries, of the pulse duration and power necessary for bubble formation whilst not exceeding the melting temperature of the nanoparticle and of the nanobubble performance metrics (e.g. maximum bubble size). While using constant thermophysical properties for the fluid and the nanoparticle we were able to provide a wealth of preliminary results for certain geometries. We also proposed a further expansion of the current modeling effort into more complex geometries in order to conclusively

determine an optimal geometry for photothermal energy conversion and provide a more comprehensive list of design parameters for experimentalists in the field.

5.2.0.4 The ensuing modeling effort in chapter 4 is more focused on the description of the colloidal behavior of photonic nanoparticles. A preliminary cooperative colloidal heating and bubble nucleation CFD analysis was performed alongside a thorough photonic investigation of the power absorbed by the nanoparticles at varying orientations. The results of this modeling approach demonstrate the importance of colloidal heating as well as the relative orientation of the nanoparticle for practical applications. Current results indicate that the suggested use of nanorings, nanotori and nanoframes is advantageous for colloidal photothermal applications since their level of absorption remains relatively high for a wider range of orientations. Of these nanostructure morphologies, the use of nanoframes is most recommended since they can be readily synthesized via bottom up fabrication techniques and their absorption cross-section remains high independent of orientation. More specifically, nanoframe geometries with more densely packed frame elements can provide enhanced photothermal heating due to electromagnetic coupling and heating between the elements. This phenomenon in combination with the lower nanobubble nucleation power demands owing to cooperative heating, leads to increased nanobubble generation selectivity for highly localized cancer cell destruction when adequate uptake is achieved.

5.2.0.5 In terms of potential future work avenues, we proposed the study of the Two-Temperature Model (TTM) in order to extend our current modelling effort to femto- and pico-second pulse durations as well as a further refinement of previous models with the implementation of temperature dependent material properties and additional photonic analyses specific to the post-nucleation environment. This combined attempt aims at eliminating any potential discrepancies between modeling and experimental results, increasing model sophistication and thus providing the most accurate description of the photothermal process to date.

5.2.0.6. In summary, the modeling approach suggested herein a) directly addresses the knowledge gap of photothermal therapy nanobubble specifics such as required wavelength for plasmon resonance, required energy and pulse duration to achieve nucleation without melting or even evaporating the nanoparticles of various morphologies, b) explains the photothermal and optical behavior of colloidal plasmonic nanoparticles and, most importantly, c) provides experimentalists in any field involving bioapplications of nanotransducers with a most accurate rational guide for the development of novel applications.

References

- Agarwal, A, et al. (2007), 'Targeted gold nanorod contrast agent for prostate cancer detection by photoacoustic imaging', *J. Appl. Phys.*, 102, 064701.
- Aizpurua, J., et al. (2003), 'Optical properties of gold nanorings', *Physical Review Letters*, 90 (5).
- Alali, Fatema, et al. (2013), 'Photonic and thermofluidic analysis of colloidal plasmonic nanorings and nanotori for pulsed-laser photothermal applications', *The Journal of Physical Chemistry C*, 117 (39), 20178-85.
- Albanese, Alexandre and Chan, Warren CW (2011), 'Effect of gold nanoparticle aggregation on cell uptake and toxicity', *ACS nano*, 5 (7), 5478-89.
- Arbouet, A, et al. (2004), 'Direct measurement of the single-metal-cluster optical absorption', *Physical review letters*, 93 (12), 127401.
- Au, Leslie, et al. (2008), 'A quantitative study on the photothermal effect of immuno gold nanocages targeted to breast cancer cells', *ACS nano*, 2 (8), 1645-52.
- Baffou, Guillaume and Rigneault, Hervé (2011), 'Femtosecond-pulsed optical heating of gold nanoparticles', *Physical Review B*, 84 (3), 035415.
- Baffou, Guillaume and Quidant, Romain (2013), 'Thermo-plasmonics: using metallic nanostructures as nano-sources of heat', *Laser & Photonics Reviews*, 7 (2), 171-87.
- Bohren, Craig F and Huffman, Donald R (2008), *Absorption and scattering of light by small particles* (John Wiley & Sons).
- Brust, M, et al. (1995), 'Synthesis and reactions of functionalised gold nanoparticles', *Journal of the Chemical Society, Chemical Communications*, (16), 1655-56.
- Brust, Mathias, et al. (1994), 'Synthesis of thiol-derivatised gold nanoparticles in a two-phase liquid-liquid system', *Journal of the Chemical Society, Chemical Communications*, (7), 801-02.

- Carrara, Sandro (2010), *Nano-bio-sensing* (Springer Science & Business Media).
- Cepak, Veronica M and Martin, Charles R (1998), 'Preparation and stability of template-synthesized metal nanorod sols in organic solvents', *The Journal of Physical Chemistry B*, 102 (49), 9985-90.
- Chang, Ser-Sing, et al. (1999), 'The shape transition of gold nanorods', *Langmuir*, 15 (3), 701-09.
- Chen, C. L., et al. (2010a), 'In situ real-time investigation of cancer cell photothermalolysis mediated by excited gold nanorod surface plasmons', *Biomaterials*, 31 (14), 4104-12.
- Chen, Huanjun, et al. (2010b), 'Understanding the photothermal conversion efficiency of gold nanocrystals', *Small*, 6 (20), 2272-80.
- Chen, J., et al. (2005), 'Gold nanocages: Bioconjugation and their potential use as optical imaging contrast agents', *Nano Letters*, 5 (3), 473-77.
- Chen, Jingyi, et al. (2010c), 'Gold Nanocages as Photothermal Transducers for Cancer Treatment', *Small*, 6 (7), 811-17.
- Chen, Jingyi, et al. (2007), 'Immuno gold nanocages with tailored optical properties for targeted photothermal destruction of cancer cells', *Nano letters*, 7 (5), 1318-22.
- Cherukuri, Paul, Glazer, Evan S, and Curley, Steven A (2010), 'Targeted hyperthermia using metal nanoparticles', *Advanced drug delivery reviews*, 62 (3), 339-45.
- Chithrani, B Devika, Ghazani, Arezou A, and Chan, Warren CW (2006), 'Determining the size and shape dependence of gold nanoparticle uptake into mammalian cells', *Nano letters*, 6 (4), 662-68.
- Cho, Kwangjae, et al. (2008), 'Therapeutic nanoparticles for drug delivery in cancer', *Clinical cancer research*, 14 (5), 1310-16.
- Choi, Won Il, et al. (2011), 'Tumor regression in vivo by photothermal therapy based on gold-nanorod-loaded, functional nanocarriers', *ACS nano*, 5 (3), 1995-2003.

- Coronado, Eduardo A and Schatz, George C (2003), 'Surface plasmon broadening for arbitrary shape nanoparticles: A geometrical probability approach', *The Journal of chemical physics*, 119 (7), 3926-34.
- Daniel, Marie-Christine and Astruc, Didier (2004), 'Gold nanoparticles: assembly, supramolecular chemistry, quantum-size-related properties, and applications toward biology, catalysis, and nanotechnology', *Chemical reviews*, 104 (1), 293-346.
- Day, Emily S, et al. (2011), 'Nanoshell-mediated photothermal therapy improves survival in a murine glioma model', *Journal of neuro-oncology*, 104 (1), 55-63.
- Dickerson, Erin B, et al. (2008), 'Gold nanorod assisted near-infrared plasmonic photothermal therapy (PPTT) of squamous cell carcinoma in mice', *Cancer letters*, 269 (1), 57-66.
- Dutta, C. M., et al. (2008), 'Plasmonic properties of a metallic torus', *Journal of Chemical Physics*, 129 (8).
- Ekici, O., et al. (2008), 'Thermal analysis of gold nanorods heated with femtosecond laser pulses', *Journal of Physics D-Applied Physics*, 41 (18).
- Etchegoin, P. G., Le Ru, E. C., and Meyer, M. (2006), 'An analytic model for the optical properties of gold', *Journal of Chemical Physics*, 125 (16).
- (2007), 'An analytic model for the optical properties of gold (vol 125, pg 164705, 2006)', *Journal of Chemical Physics*, 127 (18).
- Faraday, Michael (1857), 'The Bakerian lecture: experimental relations of gold (and other metals) to light', *Philosophical Transactions of the Royal Society of London*, 147, 145-81.
- Foss Jr, Colby A, et al. (1992), 'Optical properties of composite membranes containing arrays of nanoscopic gold cylinders', *The Journal of Physical Chemistry*, 96 (19), 7497-99.
- Frangioni, John V (2003), 'In vivo near-infrared fluorescence imaging', *Current opinion in chemical biology*, 7 (5), 626-34.

- Frens, G (1973), 'Controlled nucleation for the regulation of particle size in monodisperse gold solutions', *Nature Phys. Sci*, 241, 20.
- Furlani, E. P. and Baev, A. (2009a), 'Free-space excitation of resonant cavities formed from cloaking metamaterial', *Journal of Modern Optics*, 56 (4), 523-29.
- (2009b), 'Optical nanotrapping using cloaking metamaterial', *Physical Review E*, 79 (2).
- Furlani, E. P., Karampelas, I. H., and Xie, Q. (2012), 'Analysis of pulsed laser plasmon-assisted photothermal heating and bubble generation at the nanoscale', *Lab on a Chip*, 12 (19), 3707-19.
- Gilstrap, Kyle, et al. (2011), 'Nanotechnology for energy-based cancer therapies', *Am J Cancer Res*, 1 (4), 508-20.
- Gobin, Andre M, et al. (2005), 'Near infrared laser-tissue welding using nanoshells as an exogenous absorber', *Lasers in Surgery and Medicine*, 37 (2), 123-29.
- Gobin, André M, et al. (2007), 'Near-infrared resonant nanoshells for combined optical imaging and photothermal cancer therapy', *Nano letters*, 7 (7), 1929-34.
- Goodman, S. L, Hodges, G. M, and Livingston, D. C (1980), 'A review of the colloidal gold marker system', *Scanning Electron Microsc.*, 2, 133 - 46.
- Gu, Frank X, et al. (2007), 'Targeted nanoparticles for cancer therapy', *Nano today*, 2 (3), 14-21.
- Hao, E and Schatz, G (2004), 'Electromagnetic fields around silver nanoparticles and dimers', *J. Chem. Phys.*, 120, 357 - 66.
- Hao, E, Schatz, G, and Hupp, J (2004), 'Synthesis and optical properties of anisotropic metal nanoparticles', *J. Fluorescence*, 14, 331 - 41.
- Hartland, G. V and Hu, M (2002), 'Photophysics of metal nanoparticles: heat dissipation and coherent excitation of phonon modes', *Proc. SPIE*, 4807, 166 - 76.

- Hartland, G. V, Hu, M, and Sader, J. E (2003), 'Softening of the symmetric breathing mode in gold particles by laser-induced heating', *J. Phys. Chem. B*, 107, 7472 - 278.
- Hashimoto, S., Werner, D., and Uwada, T. (2012), 'Studies on the interaction of pulsed lasers with plasmonic gold nanoparticles toward light manipulation, heat management, and nanofabrication', *Journal of Photochemistry and Photobiology C-Photochemistry Reviews*, 13 (1), 28-54.
- Hirsch, L_R, et al. (2003), 'Nanoshell-mediated near-infrared thermal therapy of tumors under magnetic resonance guidance', *Proceedings of the National Academy of Sciences*, 100 (23), 13549-54.
- Hirsch, Leon R, et al. (2006), 'Metal nanoshells', *Annals of biomedical engineering*, 34 (1), 15-22.
- Hirt, C. W. and Nichols, B. D. (1981), 'VOLUME OF FLUID (VOF) METHOD FOR THE DYNAMICS OF FREE BOUNDARIES', *Journal of Computational Physics*, 39 (1), 201-25.
- Hotze, Ernest M, Phenrat, Tanapon, and Lowry, Gregory V (2010), 'Nanoparticle aggregation: challenges to understanding transport and reactivity in the environment', *Journal of environmental quality*, 39 (6), 1909-24.
- Hu, Min and Hartland, Gregory V (2002), 'Heat dissipation for Au particles in aqueous solution: relaxation time versus size', *The Journal of Physical Chemistry B*, 106 (28), 7029-33.
- Huang, Huang-Chiao, et al. (2011), 'Synergistic administration of photothermal therapy and chemotherapy to cancer cells using polypeptide-based degradable plasmonic matrices', *Nanomedicine*, 6 (3), 459-73.
- Huang, Xiaohua, et al. (2006), 'Cancer cell imaging and photothermal therapy in the near-infrared region by using gold nanorods', *Journal of the American Chemical Society*, 128 (6), 2115-20.
- Huang, Xiaohua, et al. (2008), 'Plasmonic photothermal therapy (PPTT) using gold nanoparticles', *Lasers in medical science*, 23 (3), 217-28.

- Huff, Terry B, et al. (2007), 'Hyperthermic effects of gold nanorods on tumor cells'.
- Huttmann, G, Yao, C, and Endl, E (2005), 'New concepts in laser medicine: towards a laser surgery with cellular precision', *Med. Laser Appl.*, 20, 135 - 39.
- Huttmann, G, et al. (2002), 'High precision cell surgery with nanoparticles?', *Med. Laser Appl.*, 17, 9 - 14.
- Imura, Kohei, Nagahara, Tetsuhiko, and Okamoto, Hiromi (2005), 'Near-field two-photon-induced photoluminescence from single gold nanorods and imaging of plasmon modes', *The Journal of Physical Chemistry B*, 109 (27), 13214-20.
- Inasawa, S., Sugiyama, M., and Yamaguchi, Y. (2005), 'Laser-induced shape transformation of gold nanoparticles below the melting point: The effect of surface melting', *Journal of Physical Chemistry B*, 109 (8), 3104-11.
- Jain, P. K., et al. (2008), 'Noble Metals on the Nanoscale: Optical and Photothermal Properties and Some Applications in Imaging, Sensing, Biology, and Medicine', *Accounts of Chemical Research*, 41 (12), 1578-86.
- Jain, Prashant K, El-Sayed, Ivan H, and El-Sayed, Mostafa A (2007), 'Au nanoparticles target cancer', *nano today*, 2 (1), 18-29.
- Jemal, Ahmedin, et al. (2009), 'Cancer statistics, 2009', *CA: a cancer journal for clinicians*, 59 (4), 225-49.
- Jiang, Li-Ping, et al. (2004), 'Ultrasonic-assisted synthesis of monodisperse single-crystalline silver nanoplates and gold nanorings', *Inorganic Chemistry*, 43 (19), 5877-83.
- Johnson, P. B. and Christy, R. W. (1972), 'OPTICAL-CONSTANTS OF NOBLE-METALS', *Physical Review B*, 6 (12), 4370-79.
- Karampelas, Ioannis H, et al. (2016), 'Plasmonic Nanoframes for Photothermal Energy Conversion', *The Journal of Physical Chemistry C*, 120 (13), 7256-64.
- Khatua, Saumyakanti, et al. (2014), 'Resonant plasmonic enhancement of single-molecule fluorescence by individual gold nanorods', *ACS nano*, 8 (5), 4440-49.

- Khlebtsov, Boris, et al. (2006), 'Optical amplification of photothermal therapy with gold nanoparticles and nanoclusters', *Nanotechnology*, 17 (20), 5167.
- Khlebtsov, N., et al. (2013), 'Analytical and Theranostic Applications of Gold Nanoparticles and Multifunctional Nanocomposites', *Theranostics*, 3 (3), 167-80.
- Kotaidis, V, et al. (2006), 'Excitation of nanoscale vapor bubbles at the surface of gold nanoparticles in water', *The Journal of chemical physics*, 124 (18), 184702.
- Kottmann, Jörg P, et al. (2001), 'Plasmon resonances of silver nanowires with a nonregular cross section', *Physical Review B*, 64 (23), 235402.
- Kreibig, U and Vollmer, M (1995), *Optical Properties of Metal Clusters* (**Berlin**: Springer).
- Lal, Surbhi, Clare, Susan E, and Halas, Naomi J (2008), 'Nanoshell-enabled photothermal cancer therapy: impending clinical impact', *Accounts of chemical research*, 41 (12), 1842-51.
- Lapotko, D. O., Lukianova, E., and Oraevsky, A. A. (2006a), 'Selective laser nanothermolysis of human leukemia cells with microbubbles generated around clusters of gold nanoparticles', *Lasers in Surgery and Medicine*, 38 (6), 631-42.
- Lapotko, Dmitri (2009a), 'Optical excitation and detection of vapor bubbles around plasmonic nanoparticles', *Optics Express*, 17 (4), 2538-56.
- (2009b), 'Plasmonic nanoparticle-generated photothermal bubbles and their biomedical applications', *Nanomedicine*, 4 (7), 813-45.
- (2009c), 'Pulsed photothermal heating of the media during bubble generation around gold nanoparticles', *International Journal of Heat and Mass Transfer*, 52 (5-6), 1540-43.
- Lapotko, Dmitri, et al. (2006b), 'Method of laser activated nano-thermolysis for elimination of tumor cells', *Cancer Letters*, 239 (1), 36-45.

- Lee, Cheng-Kuang, et al. (2010), 'Characterizing the localized surface plasmon resonance behaviors of Au nanorings and tracking their diffusion in bio-tissue with optical coherence tomography', *Biomedical optics express*, 1 (4), 1060-74.
- Letfullin, R. R, et al. (2006), 'Laser-induced explosion of gold nanoparticles: potential role for nanophotothermolysis of cancer', *Nanomedicine*, 1, 473 - 80.
- Lewinski, N, Colvin, V, and Drezek, R (2008), 'Cytotoxicity of nanoparticles', *Small*, 4, 26 - 49.
- Li, Zhiming, et al. (2009), 'RGD-conjugated dendrimer-modified gold nanorods for in vivo tumor targeting and photothermal therapy†', *Molecular Pharmaceutics*, 7 (1), 94-104.
- Lim, Yong Taik, et al. (2003), 'Selection of quantum dot wavelengths for biomedical assays and imaging', *Molecular imaging*, 2 (1), 50-64.
- Lombard, Julien, Biben, Thierry, and Merabia, Samy (2014), 'Kinetics of nanobubble generation around overheated nanoparticles', *Physical review letters*, 112 (10), 105701.
- Loo, Christopher, et al. (2005), 'Immunotargeted nanoshells for integrated cancer imaging and therapy', *Nano letters*, 5 (4), 709-11.
- Loo, Christopher, et al. (2004), 'Nanoshell-enabled photonics-based imaging and therapy of cancer', *Technology in cancer research & treatment*, 3 (1), 33-40.
- Lukianova-Hleb, E. Y. and Lapotko, D. O. (2014), 'Nano-Theranostics With Plasmonic Nanobubbles', *Ieee Journal of Selected Topics in Quantum Electronics*, 20 (3), 12.
- Lukianova-Hleb, E. Y., et al. (2012a), 'Plasmonic Nanobubbles Rapidly Detect and Destroy Drug-Resistant Tumors', *Theranostics*, 2 (10), 976-87.
- Lukianova-Hleb, Ekaterina, et al. (2010), 'Plasmonic nanobubbles as transient vapor nanobubbles generated around plasmonic nanoparticles', *ACS nano*, 4 (4), 2109-23.

- Lukianova-Hleb, Ekaterina Y., et al. (2011), 'Selective and Self-Guided Micro-Ablation of Tissue with Plasmonic Nanobubbles', *Journal of Surgical Research*, 166 (1), e3-e13.
- Lukianova-Hleb, Ekaterina Y., et al. (2012b), 'Plasmonic nanobubble-enhanced endosomal escape processes for selective and guided intracellular delivery of chemotherapy to drug-resistant cancer cells', *Biomaterials*, 33 (6), 1821-26.
- Mackey, Megan A, et al. (2013), 'Inducing cancer cell death by targeting its nucleus: solid gold nanospheres versus hollow gold nanocages', *Bioconjugate chemistry*, 24 (6), 897-906.
- Mahmoud, MA, Snyder, B, and El-Sayed, MA (2010), 'Surface plasmon fields and coupling in the hollow gold nanoparticles and surface-enhanced Raman spectroscopy. theory and experiment†', *The Journal of Physical Chemistry C*, 114 (16), 7436-43.
- Mahmoud, Mahmoud A and El-Sayed, Mostafa A (2010), 'Gold nanoframes: Very high surface plasmon fields and excellent near-infrared sensors', *Journal of the American Chemical Society*, 132 (36), 12704-10.
- Martin, Charles R (1994), 'Nanomaterials--a membrane-based synthetic approach', (DTIC Document).
- (1996), 'Membrane-based synthesis of nanomaterials', *Chemistry of Materials*, 8 (8), 1739-46.
- Moon, H. K., Lee, S. H., and Choi, H. C. (2009), 'In Vivo Near-Infrared Mediated Tumor Destruction by Photothermal Effect of Carbon Nanotubes', *Acs Nano*, 3 (11), 3707-13.
- Murphy, Catherine J, et al. (2005), 'Anisotropic metal nanoparticles: synthesis, assembly, and optical applications', *The Journal of Physical Chemistry B*, 109 (29), 13857-70.
- Myroshnychenko, Viktor, et al. (2008), 'Modelling the optical response of gold nanoparticles', *Chemical Society Reviews*, 37 (9), 1792-805.

- O'Neal, D Patrick, et al. (2004), 'Photo-thermal tumor ablation in mice using near infrared-absorbing nanoparticles', *Cancer letters*, 209 (2), 171-76.
- Oldenburg, A. L, et al. (2006), 'Plasmon-resonant gold nanorods as low backscattering albedo contrast agents for optical coherence tomography', *Opt. Express*, 14, 6724 - 38.
- Pattamatta, A. and Madnia, C. K. (2010), 'Modeling Carrier-Phonon Nonequilibrium Due to Pulsed Laser Interaction With Nanoscale Silicon Films', *Journal of Heat Transfer-Transactions of the Asme*, 132 (8).
- Peer, Dan, et al. (2007), 'Nanocarriers as an emerging platform for cancer therapy', *Nature nanotechnology*, 2 (12), 751-60.
- Pérez-Juste, Jorge, et al. (2005), 'Gold nanorods: synthesis, characterization and applications', *Coordination Chemistry Reviews*, 249 (17), 1870-901.
- Petrova, H., et al. (2006), 'On the temperature stability of gold nanorods: comparison between thermal and ultrafast laser-induced heating', *Physical Chemistry Chemical Physics*, 8 (7), 814-21.
- Pitsillides, C. M, et al. (2003), 'Selective cell targeting with light-absorbing microparticles and nanoparticles', *Biophys. J.*, 84, 4023 - 32.
- Pustovalov, Viktor K (2005), 'Theoretical study of heating of spherical nanoparticle in media by short laser pulses', *Chemical Physics*, 308 (1), 103-08.
- Pustovalov, VK, Smetannikov, AS, and Zharov, VP (2008), 'Photothermal and accompanied phenomena of selective nanophotothermolysis with gold nanoparticles and laser pulses', *Laser Physics Letters*, 5 (11), 775.
- Reetz, Manfred T and Helbig, Wolfgang (1994), 'Size-selective synthesis of nanostructured transition metal clusters', *Journal of the American Chemical Society*, 116 (16), 7401-02.
- Roper, D. K., Ahn, W., and Hoepfner, M. (2007), 'Microscale heat transfer transduced by surface plasmon resonant gold nanoparticles', *Journal of Physical Chemistry C*, 111 (9), 3636-41.

- Schultz, S, et al. (2000), 'Single-target molecule detection with nonbleaching multicolor optical immunolabels', *Proc. Natl Acad. Sci.*, 97, 996 - 1001.
- Singh, N. (2010), 'TWO-TEMPERATURE MODEL OF NONEQUILIBRIUM ELECTRON RELAXATION: A REVIEW', *International Journal of Modern Physics B*, 24 (9), 1141-58.
- Skrabalak, Sara E, et al. (2007), 'Gold nanocages for biomedical applications', *Advanced Materials*, 19 (20), 3177-84.
- Sonnichsen, C, et al. (2002), 'Drastic reduction of plasmon damping in gold nanorods', *Phys. Rev. Lett.*, 88, 077402.
- Sun, Y. G. and Xia, Y. N. (2003a), 'Alloying and dealloying processes involved in the preparation of metal nanoshells through a galvanic replacement reaction', *Nano Letters*, 3 (11), 1569-72.
- Sun, Yugang and Xia, Younan (2003b), 'Triangular nanoplates of silver: synthesis, characterization, and use as sacrificial templates for generating triangular nanorings of gold', *Advanced Materials*, 15 (9), 695-99.
- Turkevich, John, Stevenson, Peter Cooper, and Hillier, James (1951), 'A study of the nucleation and growth processes in the synthesis of colloidal gold', *Discussions of the Faraday Society*, 11, 55-75.
- van de Hulst, H. C. (1981), *Scattering of Light by Small Particles* (New York: Dover Publications Inc.).
- Van der Zande, Bianca MI, et al. (1997), 'Aqueous gold sols of rod-shaped particles', *The Journal of Physical Chemistry B*, 101 (6), 852-54.
- Vogel, Alfred, et al. (2008), 'Femtosecond-laser-induced nanocavitation in water: implications for optical breakdown threshold and cell surgery', *Physical review letters*, 100 (3), 038102.
- Volkov, Alexey N, Sevilla, Carlos, and Zhigilei, Leonid V (2007), 'Numerical modeling of short pulse laser interaction with Au nanoparticle surrounded by water', *Applied Surface Science*, 253 (15), 6394-99.

- von Maltzahn, Geoffrey, et al. (2009), 'Computationally guided photothermal tumor therapy using long-circulating gold nanorod antennas', *Cancer research*, 69 (9), 3892-900.
- Wan, Dehui, et al. (2013), 'Robust synthesis of gold cubic nanoframes through a combination of galvanic replacement, gold deposition, and silver dealloying', *Small*, 9 (18), 3111-17.
- Wang, H, et al. (2005), 'In vitro and in vivo two-photon luminescence imaging of single gold nanorods', *Proc. Natl Acad. Sci. USA*, 102, 15752 – 56.
- Wang, Yucai, et al. (2013), 'Comparison study of gold nanohexapods, nanorods, and nanocages for photothermal cancer treatment', *ACS nano*, 7 (3), 2068-77.
- Wang, ZL (2000), 'Transmission electron microscopy of shape-controlled nanocrystals and their assemblies', *The Journal of Physical Chemistry B*, 104 (6), 1153-75.
- Xia, Younan, et al. (1999), 'Unconventional methods for fabricating and patterning nanostructures', *Chemical reviews*, 99 (7), 1823-48.
- Xiong, Wei, et al. (2014), 'Plasmonic caged gold nanorods for near-infrared light controlled drug delivery', *Nanoscale*, 6, 14388-93.
- Yakunin, Alexander N, Avetisyan, Yuri A, and Tuchin, Valery V (2015), 'Quantification of laser local hyperthermia induced by gold plasmonic nanoparticles', *Journal of biomedical optics*, 20 (5), 051030-30.
- Yan, F. and Goedel, W. A. (2005), 'The preparation of mesoscopic rings in colloidal crystal templates', *Angewandte Chemie-International Edition*, 44 (14), 2084-88.
- Yavuz, M. S., et al. (2009), 'Gold nanocages covered by smart polymers for controlled release with near-infrared light', *Nature Materials*, 8 (12), 935-39.
- Yu, Yu-Ying, et al. (1997), 'Gold nanorods: electrochemical synthesis and optical properties', *The Journal of Physical Chemistry B*, 101 (34), 6661-64.

Yuan, Hsiangkuo, Fales, Andrew M, and Vo-Dinh, Tuan (2012), 'TAT peptide-functionalized gold nanostars: enhanced intracellular delivery and efficient NIR photothermal therapy using ultralow irradiance', *Journal of the American Chemical Society*, 134 (28), 11358-61.

Zheng, X. H., et al. (2012), 'Enhanced Tumor Treatment Using Biofunctional Indocyanine Green-Containing Nanostructure by Intratumoral or Intravenous Injection', *Molecular Pharmaceutics*, 9 (3), 514-22.

Zinchenko, A. A., Yoshikawa, K., and Baigl, D. (2005), 'DNA-templated silver nanorings', *Advanced Materials*, 17 (23), 2820-+.